

# **Characterisation of Atomically-Thin Transition Metal Dichalcogenides**

by

**Paweł Jan Palczyński**

A thesis submitted in partial fulfilment of the requirements for the award of the degree

Doctor of Philosophy

from

Imperial College London

Faculty of Engineering, Department of Materials

October 18, 2019



## **Declaration of originality**

I hereby declare that this thesis is the result of my own work unless otherwise referenced or acknowledged. This document is submitted in partial fulfilment of the requirements for the award of Doctor of Philosophy in the Department of Materials, Imperial College London and it has not been submitted to any other academic institution awarding qualifications.

Paweł Jan Palczyński

## **Copyright declaration**

"The copyright of this thesis rests with the author. Unless otherwise indicated, its contents are licensed under a Creative Commons Attribution-Non Commercial 4.0 International Licence (CC BY-NC). Under this licence, you may copy and redistribute the material in any medium or format. You may also create and distribute modified versions of the work. This is on the condition that: you credit the author and do not use it, or any derivative works, for a commercial purpose. When reusing or sharing this work, ensure you make the licence terms clear to others by naming the licence and linking to the licence text. Where a work has been adapted, you should indicate that the work has been changed and describe those changes. Please seek permission from the copyright holder for uses of this work that are not included in this licence or permitted under UK Copyright Law."

## Acknowledgements

I would like to thank my supervisor Dr. Cecilia Mattevi for enormous amount of help, guidance, support and patience throughout my entire time in her group.

I would also like to acknowledge the examiners, Prof. Alexander Tartakovskii and Dr Peter Petrov for reviewing this thesis.

Thank you to Dr Francesco Reale for all the talks, both serious and lighthearted, and for providing me with all the CVD samples, XRD, SEM and AFM measurements and analysis.

Thank you to Ms Maria Sokolikova for the enlightening conversations and cheering me on to finish this thesis, and for all the colloidal synthesis samples, TEM imaging and analysis.

Thank you to Dr Peter Sherrell, Dr Federico Pesci and Dr Sharda Kanudha for all the guidance and help with setting up experiments and support, and for heterostructure samples, SEM imaging, electrical measurements and analysis.

I would like to acknowledge the help from collaborators, Dr. Iddo Amit, Prof. Monica F. Craciun and Prof. Saverio Russo for performing the electrical measurements.

Thank you to all the lab and office mates, Chiara Grotta, Cong Lu, Aleksandra Krajewska, Julian Buchinger, Jerome Nicolas, Nikesh Patel, Elisa Burbaum, Jeremy Tan, Mauro Och, Apostolos Panagiotopoulos, Gang Cheng, Giulia Zemignani, Stefano Tagliaferri, Gianmaria Matrone, David Poussin, Shengyang Chen, Luca Occhi, Francesco Salerno, Bartosz Barzdajn for all the interactions, talks and support that made this PhD journey complete.

And finally a thank you to my family, mamie, tacie, bratu i bratowej, for all the love and support, dziękuję.

# Publications

1. **P. Palczynski**, F. Reale, P. Sherrell, M. Sokolikova, C. Mattevi. In-doping of mono and few-layered  $WS_2$ . Submitted.
2. Peter C. Sherrell+, **Pawel Palczynski**+ (equally contributed), Maria S. Sokolikova, Francesco Reale, Federico M. Pesci, Mauro Och, Cecilia Mattevi. Large-Area CVD  $MoS_2/WS_2$  Heterojunctions as a Photoelectrocatalyst for Salt Water Oxidation. ACS Applied Energy Materials, 2019. Just accepted.
3. T. Wakamura, F. Reale, **P. Palczynski**, M. Q. Zhao, A. T. C. Johnson, S. Guéron, C. Mattevi, A. Ouerghi, and H. Bouchiat. Spin-orbit interaction induced in graphene by transition metal dichalcogenides. Physical Review B, 99(24), June 2019.
4. Maria S. Sokolikova, Peter C. Sherrell, **Pawel Palczynski**, Victoria L. Bemmer, and Cecilia Mattevi. Direct solution-phase synthesis of 1T'  $WSe_2$  nanosheets. Nature Communications, 10(1), February 2019.
5. Peter C. Sherrell, Kanudha Sharda, Chiara Grotta, Jacopo Ranalli, Maria S. Sokolikova, Federico M. Pesci, **Pawel Palczynski**, Victoria L. Bemmer, and Cecilia Mattevi. Thickness-dependent characterization of chemically exfoliated  $TiS_2$  nanosheets. ACS Omega, 3(8):86558662, August 2018.
6. Hugo Henck, Zeineb Ben Aziza, Debora Pierucci, Feriel Laourine, Francesco Reale, **Pawel Palczynski**, Julien Chaste, Mathieu G. Silly, François Bertran, Patrick Le Fèvre, Emmanuel Lhuillier, Taro Wakamura, Cecilia Mattevi, Julien E. Rault, Matteo Calandra, and Abdelkarim Ouerghi. Electronic band structure of twodimensional  $WS_2$ /graphene van der waals heterostructures. Physical Review B, 97(15), April 2018.
7. T. Wakamura, F. Reale, **P. Palczynski**, S. Guéron, C. Mattevi, and H. Bouchiat. Strong anisotropic spin-orbit interaction induced in graphene by monolayer  $WS_2$ . Physical Review Letters, 120(10), March 2018.

8. Francesco Reale, **Pawel Palczynski**, Iddo Amit, Gareth F. Jones, Jake D. Mehew, Agnes Bacon, Na Ni, Peter C. Sherrell, Stefano Agnoli, Monica F. Craciun, Saverio Russo, and Cecilia Mattevi. High-mobility and high-optical quality atomically thin  $WS_2$ . *Scientific Reports*, 7(1), November 2017.
9. Chiara Grotta, Peter C Sherrell, **Pawel Palczynski**, Maria Sokolikova, Kanudha Sharda, and Cecilia Mattevi. 3D printing of 2D atomically thin materials. *ArXiv*, 3:8655-8662, October 2017.
10. Federico M. Pesci, Maria S. Sokolikova, Chiara Grotta, Peter C. Sherrell, Francesco Reale, Kanudha Sharda, Na Ni, **Pawel Palczynski**, and Cecilia Mattevi.  $MoS_2/WS_2$  heterojunction for photoelectrochemical water oxidation. *ACS Catalysis*, 7(8):4990-4998, July 2017.

## List of abbreviations

TMDC - Transition metal dichalcogenide

CVD - Chemical vapour deposition

PL - Photoluminescence

SEM - Scanning electron microscopy

TEM - Transmission electron microscopy

AFM - Atomic force microscopy

XRD - X-ray diffraction

XPS - X-ray photoelectron spectroscopy

VBM - Valence band maximum

CBM - Conduction band minimum

DFT - Density functional theory

EDS - Energy dispersive x-ray spectroscopy

LPE - Liquid phase exfoliation

FWHM - Full width half maximum

MEX - Mechanically exfoliated

OM - Optical microscopy

# Abstract

Transition metal dichalcogenides (TMDC) are a class of materials that has become increasingly popular in the recent years in the wake of discovery of graphene and its surprising properties. Despite being known for decades and being used in their bulk form as a sold lubricant or catalysts their mono and few layer form remained largely unexplored. Indeed when TMDCs are only one or few layers thick their unique optical and electronic properties emerge. In particular group VI TMDCs such as  $MoS_2$  or  $WS_2$ , as their numbers of layers decreases, turn from an indirect to direct bandgap semiconductor with possible applications in visible range optoelectronic and electronic devices. Moreover unique quantum effects such as quantum spin Hall effect, strong spin orbit interactions or topological insulators can be observed in these thin films.

One of the major hurdles standing in the path of further development of those materials is its synthesis. The commonly used methods successfully optimise one of the many desired parameters and therefore new techniques must be developed to provide an improvement across all aspects of the material quality. In order to properly asses those new growths methods metrological studies must equally contribute to the capabilities of rapid assessment of large area flakes and films. To that effect the commonly used Raman and PL are heavily employed throughout in mapping the as grown as well as transferred flakes on multiple different substrates. In a similar fashion the x-ray spectroscopy is utilised to gain insight into the samples chemistry, layer thickness and crystal structure. This triple role of XPS allowed for initial studies of 1T'  $WSe_2$  which combined with Raman and PL spectroscopy with supplement of other characterisation techniques provided valuable introspective into its structure and properties.

The overarching goal of the thesis is to develop synthesis techniques for growth of TMDCs primarily via CVD as well as colloidal synthesis in order to reliably produce thin layers with controllable thickness and lateral size. This work focuses on characterisation of the as grown materials using Raman, PL and XPS techniques to assess the quality and reproducibility of the developed synthesis methods.

Additionally in this work the novel synthesis routes for growth of  $WS_2$  large area monolayers have been assessed. The as grown samples on top of exhibiting strong PL response showed remarkable, record high electron mobility in mono and bilayer form. A certain degree of optical and electrical properties tunability is also presented in In doped  $WS_2$  layers. By combining the growth of monolayers the heterostructures of  $MoS_2/WS_2$

are successfully grown on multiple substrates and their quality and structure is carefully investigated.

# Contents

<b>Chapter 1 Thesis introduction</b>	<b>11</b>
<b>Chapter 2 The state-of-the-art of group VI transition metal disulphides and diselenides</b>	<b>14</b>
2.1 Properties of TMDCs . . . . .	14
2.1.1 Electronic properties . . . . .	16
2.1.2 Optical properties . . . . .	17
2.1.3 Optoelectronics applications . . . . .	22
2.2 Phonon dispersion . . . . .	27
2.3 Conclusions . . . . .	32
<b>Chapter 3 <math>WS_2</math> CVD state of the art</b>	<b>33</b>
3.1 Introduction . . . . .	33
3.2 The state of the art . . . . .	33
3.2.1 Bulk crystals . . . . .	33
3.2.2 Thin films of W . . . . .	34
3.2.3 $WO_3$ based CVD of $WS_2$ . . . . .	34
3.2.4 CVD growth of mono and few layer $WS_2$ . . . . .	35
3.3 Conclusions . . . . .	36
<b>Chapter 4 The state-of-the-art of bilayer heterostructure of <math>MoS_2/WS_2</math></b>	<b>37</b>
4.1 Introduction . . . . .	37
4.2 Properties of bilayer heterostructures . . . . .	38
4.3 Fabrication of bilayer heterostructures . . . . .	39
4.4 Characterization of bilayer heterostructures . . . . .	41
4.4.1 Raman spectroscopy . . . . .	41
4.4.2 Photoluminescence . . . . .	42

<b>Chapter 5 Polymorphism in group VI transition metals dichalcogenides; a specific case of 1T' and 2H phases of <math>WSe_2</math></b>	<b>48</b>
5.1 Introduction . . . . .	48
5.2 $WSe_2$ phases . . . . .	48
5.3 Conclusions . . . . .	52
<b>Chapter 6 Chemical vapour deposition of mono-few-layered <math>WS_2</math>: the role of precursors</b>	<b>53</b>
6.1 Introduction . . . . .	53
6.2 Results . . . . .	55
6.3 Conclusions . . . . .	68
<b>Chapter 7 Low temperature photoluminescence of <math>WS_2</math></b>	<b>70</b>
7.1 Introduction . . . . .	70
7.2 Results . . . . .	70
7.3 Conclusions . . . . .	74
<b>Chapter 8 Transfer procedure of monolayer TMDCs from the native substrate to <math>SiO_2/Si</math> wafer</b>	<b>75</b>
8.1 Introduction . . . . .	75
8.2 Experimental . . . . .	76
8.3 Results . . . . .	76
8.4 Conclusions . . . . .	80
<b>Chapter 9 Post-transition metal doping of monolayer <math>WS_2</math></b>	<b>81</b>
9.1 Introduction . . . . .	81
9.2 Results . . . . .	82
9.3 Conclusions . . . . .	94
<b>Chapter 10 CVD of mono-few-layered 2H <math>WSe_2</math></b>	<b>95</b>
10.1 Introduction . . . . .	95
10.2 Results . . . . .	95
10.3 Conclusions . . . . .	102
<b>Chapter 11 Physical characterisation of few-layered 1T' <math>WSe_2</math></b>	<b>103</b>
11.1 Introduction . . . . .	103

11.2 Results . . . . .	104
11.3 Conclusions . . . . .	108
<b>Chapter 12 CVD few-layered MoS<sub>2</sub>/WS<sub>2</sub> Heterostructures</b>	<b>109</b>
12.1 Introduction . . . . .	109
12.2 Results . . . . .	110
12.3 Conclusion . . . . .	119
<b>Chapter 13 Methodology</b>	<b>121</b>
13.1 Introduction . . . . .	121
13.2 Raman spectroscopy . . . . .	121
13.3 Photoluminescence spectroscopy . . . . .	124
13.4 X-ray photoelectron spectroscopy . . . . .	126
13.5 Transfer . . . . .	127
13.6 Device fabrication . . . . .	128
13.7 Scanning electron microscopy (SEM) . . . . .	130
13.8 Atomic force microscopy (AFM) . . . . .	130
13.9 TEM . . . . .	132
13.10 MATLAB Script . . . . .	133
<b>Chapter 14 Conclusions and future work</b>	<b>134</b>
<b>Bibliography</b>	<b>137</b>

# Chapter 1

## Thesis introduction

The recently popular group of materials called Transition Metal Dichalcogenides (TMDCs) have attracted a great deal of attention following the discovery of graphene. Many of the materials belonging to that group, such as  $WS_2$  or  $MoS_2$ , are semiconducting in nature. As one of the manifestations of this property is a very strong photoluminescence (PL) response observed across many monolayers of the TMDCs. Despite extensive studies into the nature of this photoluminescence response the full understanding remains elusive. The PL spectrum of many of those monolayers is complex and can be a result of many contributions from different phenomena and particles. Besides the main peak resulting from recombination of excitons, other quasi particles such as trions or bi-excitons can contribute to the spectrum at room temperature. Additionally the interactions between the material and the substrate as well as any surface effects, including adparticles, vacancies, defects or strain can alter the observable spectrum. Due to its 2D nature TMDCs are especially influenced by the surface effects.

TMDCs can also exhibit different polytype structures with most common being 2H and 1T phases. An interesting phenomena can be observed in regards to those polytypes where different phases can change from semiconducting to metallic. Those phases together with structural defects and strain can also affect the electronic structure of the TMDCs and thus influence the formation of many of the photogenerated particles. Many of these interactions are however still at the early stages of understanding.

There has been many attempts at simulating the electronic structures using computational methods such as DFT. The results however are not always compatible with the observed phenomena and show even great discrepancies between different approaches.

One of the polytypes, the 1T' phase, shows interesting properties such as that of

topological insulator. It has however remained understudied, partially due to difficulty in synthesis. There still remains many TMDCs for which 1T' phase has not been demonstrated.

Because the 2D materials inherently lack much volume or mass, many standard characterisation techniques are insufficient and can either result in insufficient resolution or signal to noise ratio or can not be applied at all. Due to this a limited set of characterisation techniques remains viable. Among those, the most useful methods which can enable metrological characterisation are Raman spectroscopy, photoluminescence (PL) spectroscopy and X-ray Photoelectron Spectroscopy (XPS). Those techniques can provide information over large sample areas in relatively short times. In particular Raman and PL spectroscopy allows for fast mapping of areas in the order of tens of square millimetre in air without the need of any sample preparation and could potentially extract information about crystallographic phases, strain, density defects, number of layers and interaction between the layers. Nevertheless, Raman and PL studies of mono and few-layered TMDCs are still at the very early stages and there is still very limited knowledge in the correlation between the materials characteristics and position, width and relative intensity of the Raman and PL peaks. Both these characterization techniques can enable fast scanning rate of large surface areas (mm and cm scale). XPS can be further used to learn about stoichiometry, oxidation states, defects, doping or alloying and it can be correlated with Raman and PL features. The combined physical and chemical characterisation can therefore help to provide insight into the fundamental properties of those materials.

In this thesis some initial work on the interpretation of PL and Raman spectra in CVD grown  $WS_2$ , doped  $WS_2$ ,  $MoS_2/WS_2$  heterostructures has been performed. This work aims at contributing to the ultimate goal of establishing a correlation system between characterisation and materials properties for wafer scale grown mono and few-layered TMDCs in the 2H and 1T/1T' polytypes. The two most common methods of producing TMDC monolayers for purpose of research is mechanical exfoliation and chemical vapour deposition (CVD). While the former in many cases tends to provide higher quality flakes it does not scale in terms of size and therefore has to be replaced by different, scalable methods. The most popular such method is CVD, with which continuous layers on at least cm scales has been demonstrated. Due to variety of used precursors and synthesis paths the quality and composition of resulting flakes varies and therefore requires an understanding of its effects on the material properties.

Using this understanding similar techniques have been applied to  $MoS_2$  and  $MoS_2/WSe_2$  vertical heterostructure. This allowed to contribute to greater body of knowledge about the interactions between the layers in heterojunctions and its effect on the opto-electronic properties. Furthermore, we have studied by PL, Raman spectroscopy and XPS the 2H phase of  $WSe_2$  and by Raman spectroscopy and XPS the 1T' phase of  $WSe_2$ .

Using colloidal synthesis unique formations of atomically thin 1T'  $WSe_2$  flakes have been observed for the first time. They have been characterised using Raman spectroscopy and XPS to provide some of the first studies of those phases to correlate structural properties and W 4f bonding energy and Raman active vibrational modes.

# Chapter 2

## The state-of-the-art of group VI transition metal disulphides and diselenides

Following the discovery and characterisation of graphene in last decade the focus has been put on other 2D materials. Similar to graphene other bulk layered materials can exist in a monolayer or few layer form. Furthermore these thin layers also exhibit a significant change of properties when number of layers decreases from bulk all the way to monolayer. One of the most popular groups of these materials are transition metal dichalcogenides (TMDC). Their general form is  $MX_2$  where M is a transition metal, and X is a chalcogen atom.

### 2.1 Properties of TMDCs

TMDCs in their layered form have been known, studied and utilised for a long time. They can be found commonly in use as stolid-state lubricants or catalysts. About 60 different TMDCs have been studied and characterised with a general formula of X-M-X where a plane of metal atoms (M) is sandwiched between two chalcogen planes (X). Out of those 40 can be considered layered materials where individual layers are strongly bonded in-plane and weakly bonded out-of-plane in between layers. These weak, interlayer, Van der Waals interactions allow to form a bulk material. These bonds are also what allows for those layers to slide on top of one another similarly to other layered materials like graphite.

TMDCs consist of two transition metal and single chalcogen atoms covalently bonded. They can be found in 3 distinct structural polytypes: 1T (tetragonal symmetry, octahedral coordination) with single layer per repeat unit, 2H (hexagonal symmetry, trigonal prismatic coordination) with 2 layers per repeat unit and 3R (rhombohedral symmetry, trigonal prismatic coordination) with 3 layers per repeat unit [1] as can be seen in Figure 2.1.

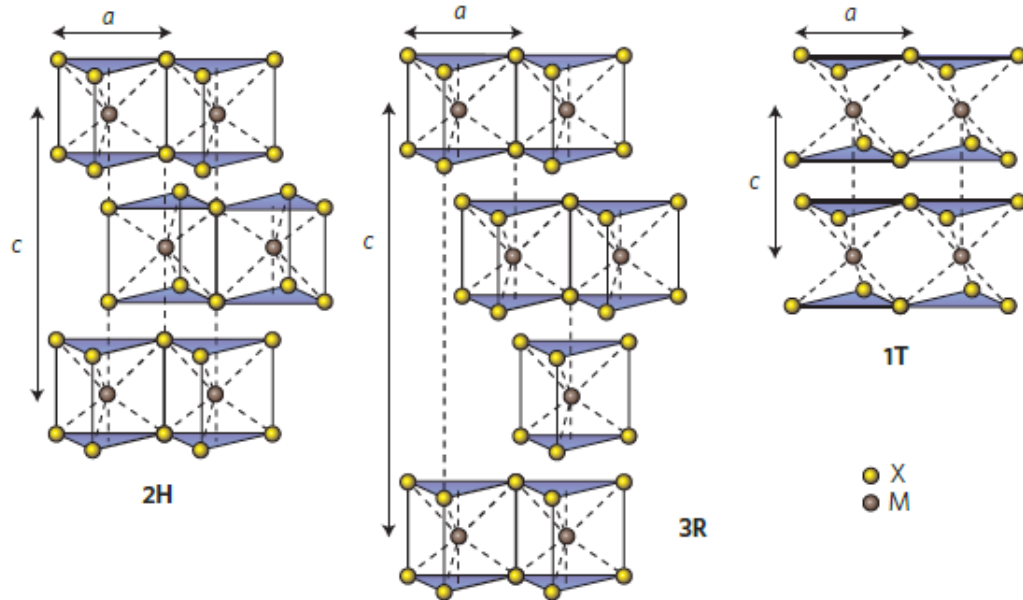


Figure 2.1: Schematics of the structural polytypes: 2H (hexagonal symmetry, two layers per repeat unit, trigonal prismatic coordination), 3R (rhombohedral symmetry, three layers per repeat unit, trigonal prismatic coordination) and 1T (tetragonal symmetry, one layer per repeat unit, octahedral coordination). The chalcogen atoms (X) are yellow and the metal atoms (M) are grey. The lattice constants  $a$  are in the range 3.1 to 3.7 Å for different materials. Adopted from [1]

Since graphene have proven to be difficult to work with in the fields of semiconductors due to its lack of natural finite electronic band gap its role as a successor in electronic and opto-electronic devices remains to be seen. However the techniques learned and effects observed during its characterisation were easily transferred to other layered compounds such as TMDCs. In particular the semiconducting, group VI-based TMDCs, containing sulphur and selenium as chalcogen atoms have proven to be more readily potentially useful as an active material in electronic and opto-electronic devices. This is due to their inherent electronic and optical bandgap in visible-near IR range.

As the number of layers changes from bulk to monolayer the properties of the TMDC

undergo a significant change. In most TMDCs the bandgap changes from indirect to a larger direct one.

### 2.1.1 Electronic properties

One of the most interesting features that the layered TMDC materials exhibit is the shift in the bandstructure with the changing number of layers. Several studies have shown in simulations and experimentally that TMDCs have very similar electronic band structure as seen in example of  $WS_2$  in Figure 2.2. In bulk  $WS_2$  the maximum of the valence band (VBM) at  $\Gamma$  point and the minimum of the conduction band (CBM) at  $\Lambda$  form an indirect bandgap. As the number of the layers decreases the CBM at  $\Lambda$  point as well as VBM at  $K$  point increases causing the band gap to widen. At 2 layers the  $K$  point becomes the actual CBM and a new indirect bandgap forms between  $\Gamma$  point and  $K$  point. Finally in a  $WS_2$  monolayer the VBM at  $K$  point as well as entire conduction band increases to form a new greater direct band gap at  $K$  point. This means that  $WS_2$  bandgap changes from 1.3 eV indirect bandgap in bulk to 2.1 eV direct bandgap in monolayer.

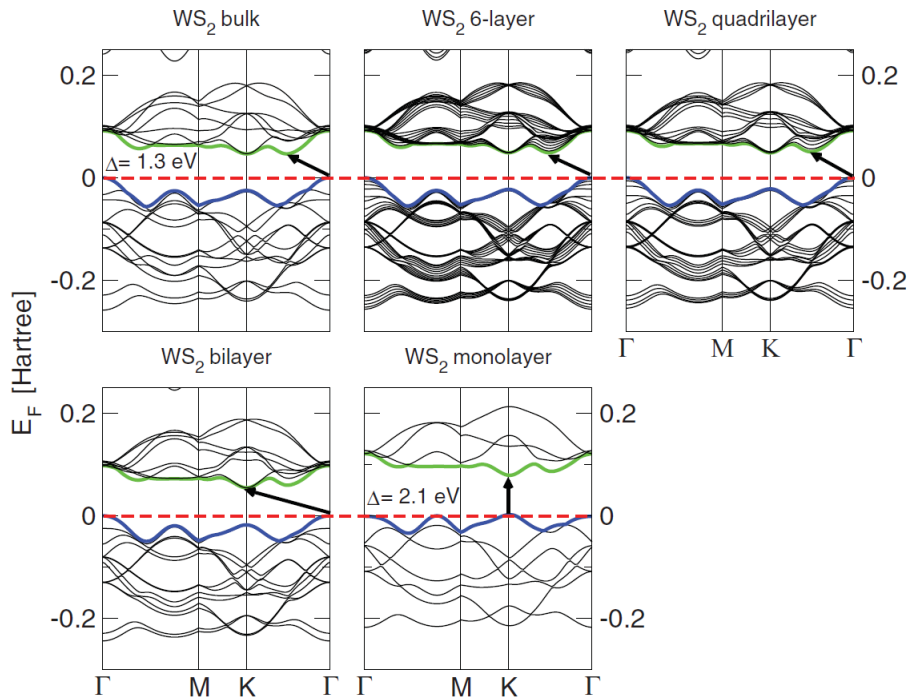


Figure 2.2: Band structures of bulk, mono and few layer  $WS_2$ , calculated from the density functional theory (DFT) simulation. Dashed lines - Fermi level. Arrows - band gap for a given number of layers. The top of valence band (blue) and bottom of conduction band (green) are highlighted. Adopted from [2]

Like  $WS_2$  other Mo and W based TMDC undergo similar transitions as seen in Table 2.1. In all cases the smaller indirect bandgap changes to greater direct bandgap with monolayer bandgap ranging from 1.1 eV to about 2.1 eV. Moreover the VBM at K points exhibits the orbit-spin band splitting at the K point of about 400 meV. This direct bandgap leads to presence of A and B excitons generated by transition between CBM and two VBMs at the K point. The conduction band as well as the valence band are dominated by the d-electron orbitals of the transition metal atoms and at the VBM and CBM they hybridize with the p-electron orbitals of the chalcogenide atoms. Because the hybridization happens mostly at the  $\Gamma$  point and the chalcogenide atoms are at the surface of the TMDC layer it leads to strong interactions between the layers. This leads to significant change in the band structure at the  $\Gamma$  and rise of the indirect bandgap as a result of increased number of layers. On the other hand at the  $K$  point the d-orbitals of the transition metals remain mostly unaffected due to them being positioned in the middle of the layer [2] [3]

Table 2.1: Mo and W based TMDC bandgaps comparison. Adopted from [1]

M\X	$-S_2$	$-Se_2$	$-Te_2$
Mo	Semiconducting	Semiconducting	Semiconducting
	1L: 1.8 eV	1L: 1.5 eV	1L: 1.1 eV
	Bulk: 1.2 eV	Bulk: 1.1 eV	Bulk: 1.0 eV
W	Semiconducting	Semiconducting	Semiconducting
	1L: 2.1 eV	1L: 1.7 eV	1L: 1.1 eV
	Bulk: 1.4 eV	Bulk: 1.2 eV	

### 2.1.2 Optical properties

TMDCs exhibit a wide array of opto-electronic effects due to their strong light-matter effects. These effects are mostly caused by the abundant presence of excitons, bi-excitons, trions or bound excitons. As a result the change in layer thickness from bulk to monolayer alters the photoluminescence, photoconductivity and absorption in the visible to infrared range.

The primary and most common quasi-particle that forms in such system is an exciton, which is a pair of a negatively charged electron and a positively charged hole bound together by Coulomb forces to form a structure similar to that of hydrogen atom. Such

pair is electrically neutral and is of size exceeding size of single cell which makes it a Wannier–Mott exciton. The recombination of these excitons results in a photon emission which can be easily observed during photoluminescence characterisation. On top of excitons other quasi-particles such as trions, bi-excitons or bound excitons can be found. A trion is a group of 2 electrons and a hole or 2 holes and an electron, or otherwise described as a charged exciton. The exact nature of the trion depends usually on the type of intrinsic doping of the TMDC. A bi-exciton is a pair of excitons which is usually only observed in quantum dot systems but can be also seen in excitonically dense systems such as TMDCs. A bound exciton is similar to the free exciton but is trapped by a defect. In a typical photoluminescence spectrum several peaks can be observed depending on specific type of TMDC characterised. In  $WS_2$  monolayer for instance as seen in Figure. 2.3 the strongest peak (often labelled as an A peak) at about 1.97 eV is caused by the direct transition of single-photon generated exciton. Slightly redshifted by about 30 meV from the A peak a generally weaker peak caused by the trion recombination can be found. At higher energies another peak can be observed due to the presence of bi-excitons. At around the 1.3 eV a much weaker peak (I) can be seen caused by the indirect transition. Additionally a B peak can be observed blueshifted from the A peak which is caused by valley splitting as discussed in chapter 2.1.1. As seen in Figure 2.3 as the number of layers increases the main A peak becomes dramatically weaker due to lack of direct transition and redshifted following the pattern discussed in chapter 2.1.1. At the same time the I peak becomes relatively stronger and eventually dominates the bulk material.

Similarly the photoconductivity of the TMDCs is strongly reliant on the number of layers and incident photon energy. The  $MoS_2$  for instance shows 3 times stronger photoconductivity in monolayer around 1.8 eV, where the direct transition is located, than in 2L  $MoS_2$  around 1.6 eV. Additionally the photoconductivity appears to increase in steps with relation to the photon energy following the direct and indirect transitions. [1].

The sunlight absorption in TMDCs has been shown to be significantly more intense than in commonly used solar cell materials, at about 5-10% which is an order of magnitude greater compared to similar thickness of Si or GaAs. It is also stronger compared to 2-3% of sunlight absorption of graphene. As a result an excitonic solar cell based on  $MoS_2/WS_2$  bilayer shows about 1% power efficiency, about 3 times greater than that of typical ultrathin solar cells [5].

During standard single photon excitation photoluminescence studies the excitons generated can be called "bright" since they appear in PL spectrum. The reason we can

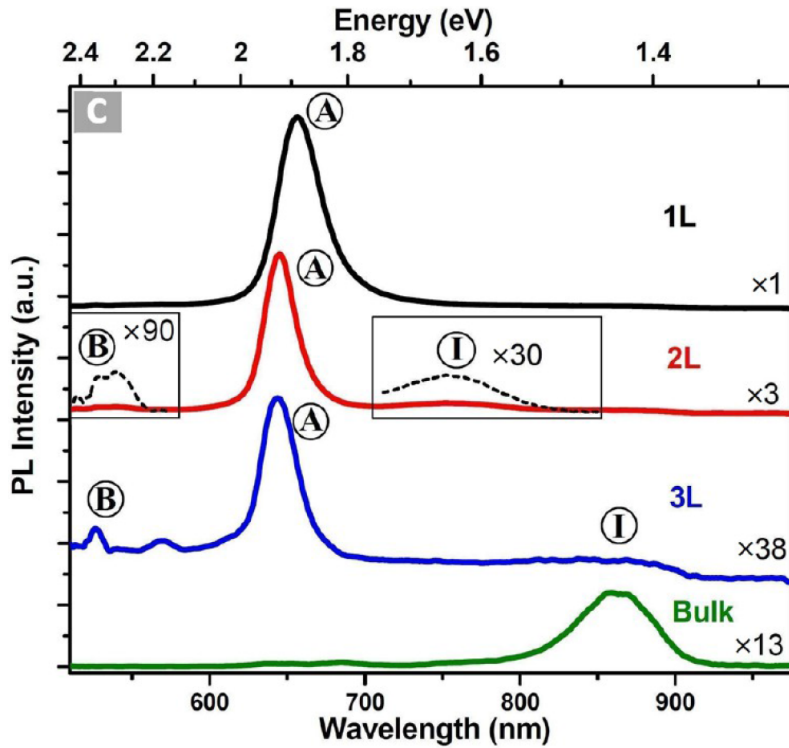


Figure 2.3: Typical PL spectrum of  $WS_2$  showing the influence of the number of layers. Adopted from [4].

observe them easily is because the spin between an electron and a hole is conserved, and thus allowing for photon emission. However another combination is possible, called dark exciton, where both electron and the hole have the same spin. Because of that they cannot recombine by emitting a photon and therefore remain absent from the PL spectrum. Even though they exist much longer than their bright counterparts their presence is of course also more difficult to observe. One way to observe them is to use two photon excitation. Due to two photon selection rule the single photon excitation can be excluded and the dark excitonic states can be observed. In  $WS_2$  the dark excitons result in two peaks at 2.28 eV and 2.48 eV. [6]

Defect engineering allows to tune the number of charge carriers. In  $MoS_2$  or  $WS_2$  the sulfur vacancies lead to increased number of electrons in the material. Because of that by increasing the number of defects in those materials the level of n-doping can be changed. An easy way to observe the presence of those defects and subsequent quenching of them is to expose the material to varying amounts of oxygen, nitrogen or water. Those species attract the electrons locally and therefore the electron population in the material decreases. This in turn leads to smaller trion population since trions require an extra electron to form. This then can be observed in PL as a more narrow direct peak,

with especially smaller redshifted shoulder. The effect can also be of course reversed by decreasing the amount of oxygen, nitrogen or water in the environment since those exist in already in ambient conditions [7].

In order to introduce and control the amount of vacancies in the TMDC different method have to be explored. One of the ways of achieving that in already grown material is the use of oxygen plasma. It has been shown that the number of defects can be controlled by limiting the plasma exposure. During the process the oxygen also chemically bonds to the MoS<sub>2</sub> at the defect sites and therefore partially negates the effect of defects on the optical properties. The PL can also be seen to increase in intensity with increasing number of defects with oxygen adsorbed due to the increased yield of bound excitons localised at these defects [8].

Similar effect has been shown using the 2,3,5,6-tetrafluoro-7,7,8,8-tetracyanoquinodimethane (*F*<sub>4</sub>*TCNQ*), 7,7,8,8-tetracyanoquinodimethane (*TCNQ*) and (nicotinamide adenine dinucleotide) *NADH* for chemical doping. Both *F*<sub>4</sub>*TCNQ* and *TCNQ* are p-type dopants while *NADH* is a n-type dopant. By exposing the surface of *MoS*<sub>2</sub> to these compounds the change in PL intensity and FWHM have been observed. Similar to doping with *O*<sub>2</sub>, *N*<sub>2</sub> or *H*<sub>2</sub>*O*, all of which are p-type dopants, the intensity of PL has increased in presence of *F*<sub>4</sub>*TCNQ* and *TCNQ*. The effect has been similarly ascribed to lowering the number of defects and therefore the lowering the trion population and subsequently increasing the exciton population increasing the yield. The opposite observation has been made with use of *NADH* with PL intensity decreasing. Similarly the increase in trion population with lower PL yield is ascribed to the lower PL intensity. [9]

It has also been show that alloying can be used to fine tune the PL by varying the concentration of alloying material. In monolayer *Mo*<sub>1-x</sub>*W*<sub>x</sub>*S*<sub>2</sub> the PL peak position initially decreases from 1.575 eV (PL peak position of pure *MoS*<sub>2</sub>) to 1.56 eV at x=0.21 and then increase up to 1.65 eV (PL peak position of *WSe*<sub>2</sub>) at x = 1. This effect could be attributed to the linearity of VB and non-linearity of CB with regards to change in W composition. The PL position can therefore be engineered on a monotonic range from 1.56 eV to 1.65 eV. In bilayer *Mo*<sub>1-x</sub>*W*<sub>x</sub>*S*<sub>2</sub> alloy the position of both direct and indirect transition PL peaks increases monotonically from about 1.49 eV and 1.53 eV for pure *MoSe*<sub>2</sub> to 1.56 eV and 1.62 eV for pure *WSe*<sub>2</sub> as the W amount is increased. This opens another relatively easy way of engineering PL position [10].

Another effect that has been demonstrated that allows for certain degree of control of PL in TMDCs is relation between the helicity of incident light and valley population

valley population. It has been shown that by exciting the monolayer  $MoS_2$  with right-polarised light the resulting excitons will fill primarily the VB at K point. Similarly by exciting the  $MoS_2$  with left-polarised light the excitons will fill the VB at K' point. After recombination the resulting photons will exhibit the same circular polarity as the photons that excited the electrons in the first place. [11][12]

The temperature effect on TMDCs has also been investigated. In  $WSe_2$  monolayer it has been shown that as the temperature of the sample increases from room temperature to about 400K the position of the direct transition PL peak redshifts from about 1.65 eV to about 1.58 eV. When the temperature is decreased from room temperature to about 5K the same peak blueshifts to about 1.7 eV. Between 100K and 50K as well 20K and 5K the position of the PL peak does not change. Additionally around 120K another peak appears and as the temperature is lowered it also blueshifts although less than the RT peak. The peak only present at RT is attributed to free excitons whereas the peak appearing at 120K is ascribed to bound excitons. As bound exciton peak appears its intensity increases with lower temperature while the intensity of the free exiton peak decreases. This indicates that the population of free excitons decreases while the population of the bound excitons increases with decreasing temperature [13]

There has been many reports on the spatial distribution of PL in the TMDCs. One of the observed patterns in  $WS_2$  and  $MoS_2$  has been that of much stronger PL intensity at the edges of the flakes. That effect has been primarily observed in small flakes of about  $5 \mu m$  [4]. It has recently been shown that the edge enhancement of the PL in  $WS_2$  flakes is caused by oxygen chemisorption. Due to presence of oxygen at the edges the electrons move towards the edges which results in greatly increased population of triions and subsequent increase in PL intensity [14].

Direct band-to-band transitions in two-dimensional system are characterized by a step-function-like spectrum originated from the energy-independent joint-density-of-states and transition matrix elements near parabolic band edges [15] (dashed blue line in Figure 2.4). However, TMDCs are dominated by excitonic effects as exemplified by experimental absorption spectrum with sharp resonance features [3] (solid green line in Figure 2.4). These excitonic effects are enabled by the very large exciton binding energies  $E_B$  (0.5–1 eV, corresponding to an exciton Bohr radius  $a_B \approx 1nm$ ) at room temperature which has been predicted theoretically and measured experimentally using optical spectroscopy and scanning tunnelling spectroscopy. Some discrepancies in the estimated value are still present but overall theory and experiment broadly agree. In addition to excitons, higher-

order excitonic quasiparticles have also been observed in 2D TMDs (Figure 2.5). Trions, which are bound states of two electrons and one hole, or two holes and one electron, have been observed in intrinsically doped monolayer TMDCs [11][16]. Bi-excitons (bound states of two excitons) have been reported in monolayer TMDCs under pulsed optical excitations [17][18] and the quinton (the five-particle negatively charged biexciton) [19].

The existence of trions at room temperature and higher-order excitonic quasiparticles in general, may open up many applications for room-temperature electrical transport of absorbed light energy, and creation of high-temperature and high-density quantum coherent states of excitons. The very high excitonic effects also generate a significant transfer of oscillator strengths from the band-to-band transitions to the fundamental 1s exciton state [15]. The ratio between the oscillator strength of the 1s ( $f_{1s}$ ) and the band-to-band ( $f_0$ ) transitions has been estimated from the ratio of the width  $\Delta$  of the 1s state ( 10 meV) and exciton binding energy  $E_B$  ( 0.5 eV), the exciton reduced mass  $\mu$  and total mass M ([20][21]) using the following equation:

$$f_{1s}/f_0 \approx 24(\mu/M)(E_B/\Delta) \approx 100 \quad (2.1)$$

This provides a value of 100 which is a large exciton oscillator strength which gives rise to a strong light absorption. Indeed, peak absorbance as large as  $A_0 \approx 0.1 - 0.3$  are observed at the exciton 1s state [22][11]. Furthermore, the strong excitonic effects lead to a short radiative lifetime  $1/\Gamma_{1s}$  ([20][21]). This can be estimated using the following equation:  $1/\Gamma_{1s} = (f_0/f_{1s})(1/\Gamma_{r0})$  This value is  $\sim 10 - 100\text{ps}$  at low temperature considering a typical band-to-band radiative lifetime to be  $1/\Gamma_{r0} \approx 1 - 10\text{ns}$ . Atomically pristine materials could potentially present even shorter radiative lifetime [23][24].

### 2.1.3 Optoelectronics applications

Here I summarize the main developments in optoelectronic devices based on 2D TMDs, in particular photodetectors, excitonic light-emitting devices (LEDs) and optical generation of spin-valley currents.

#### Photodetectors

TMDC photodetectors are still at the early stages of development and they have been used and demonstrated in the same operational wavelengths as silicon. 2D TMDCs, however present intrinsic advantages over silicon which are the mechanical flexibility and

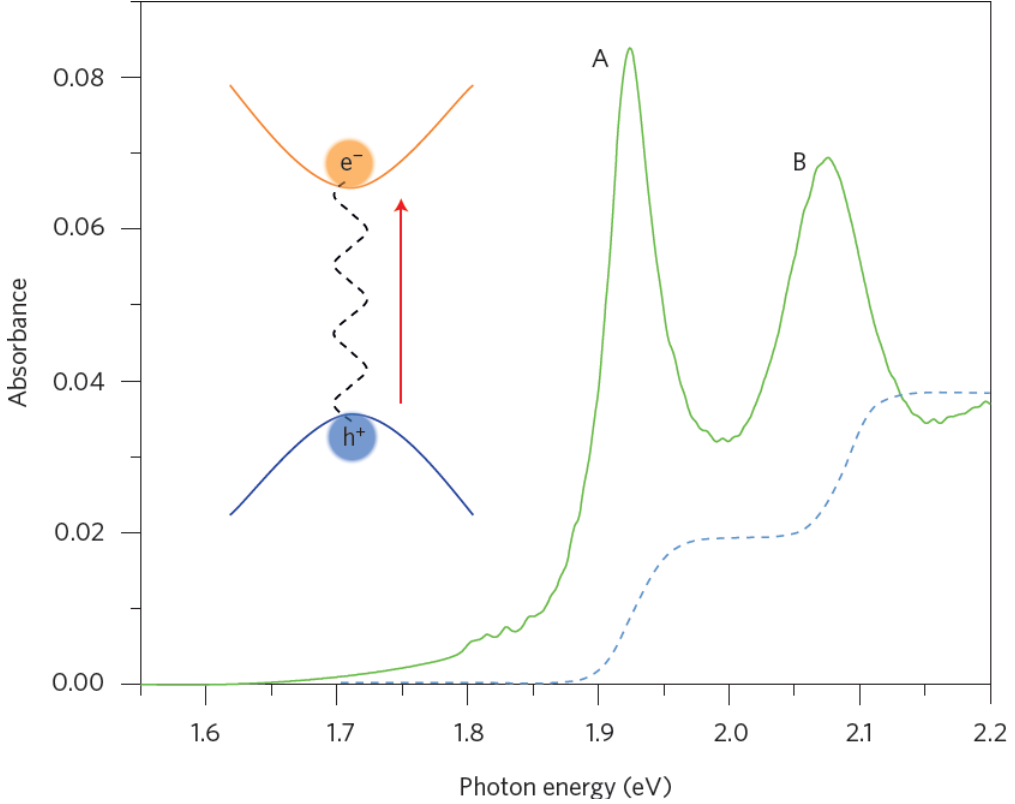


Figure 2.4: Absorption spectrum of monolayer  $MoS_2$  at 10 K in green. A and B peaks correspond to two spin-split valence to the conduction bands transition. Blue dashed line - absorbance in absence of excitonic effects. Inset - Coulomb attraction between an optically generated electron–hole pair which forms a bound exciton. Reproduced from [24]

electronically highly tunability. 2D TMDC photodetectors operate mostly on the basis of the photovoltaic effect and exhibit low dark currents and high responsivity while the operation speed remain limited. Significant improvements should be possible given the short exciton lifetimes in these materials ( 10–100 ps)[25][26][27]. The operation modes of photodetection based on the photovoltaic effect can be divided [28] into two categories: photoconduction, and photocurrent. Photoconduction is based on photoexcited carriers which increase the device’s conductance, while the photocurrent, in which photoexcited carriers are converted into current with the help of a built-in electric field originated from a symmetry-lowering element such as a junction (p-n junction). Experimental demonstration of photodetectors are based on both in-plane and out-of-plane structures of 2D TMDCs (Figure 2.6 and Figure 2.7). In-plane devices allows to control the material’s properties through electrostatic gating which offers a better accuracy than the out-of-plane devices. However the latter can support a much higher bias field (up to  $1 V nm^{-1}$ )

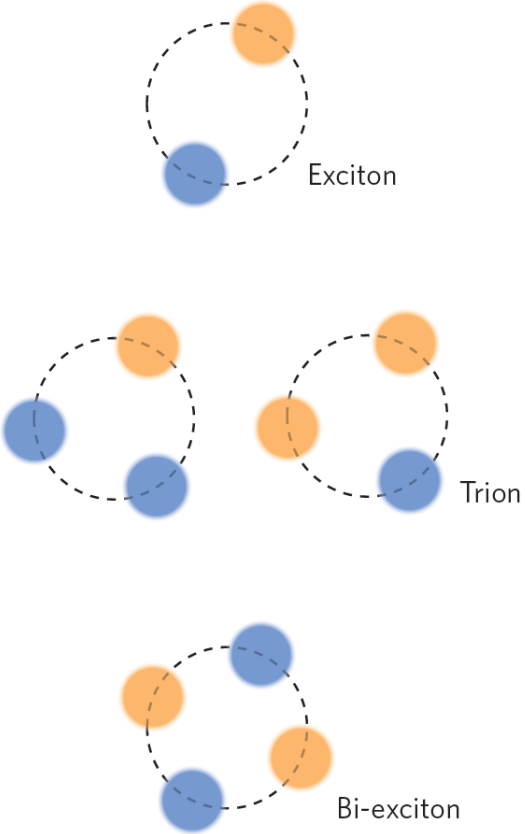


Figure 2.5: An exciton and other excitonic complexes: a natural exciton, a trion and a bi-exciton. Reproduced from [24]

which can enable a more efficient exciton dissociation. Indeed exciton dissociation in TMDCs is key due to the very high binding energy and in case of tunnelling ionization of excitons the process becomes inefficient when a bias electric field is small compared with  $E_B/(ea_B) \approx 0.2Vnm^{-1}$  [15] while excitons dissociation is effectively achieved by electric fields (either built-in or externally applied) [24].

There has been many successful attempts in making photodetectors based on photoconductivity and utilising TMDCs as an active material. Monolayer  $MoS_2$  has been used for a transistor achieving responsivity of  $880 AW^{-1}$  with a bandwidth of  $\sim 0.1Hz$  (Figure 2.6) [29]. A much better bandwidth ( $> 10kHz$ ) and therefore a faster device has been achieved, but with a smaller responsivity of  $\sim 1AW^{-1}$  [30]. The large photogain is associated with the trapped carrier at the interface states [31]. The devices conductivity tends to be modified primarily by the doping as well as trapped states [30][32][24].

Similarly devices based on photocurrent for photodetection have been achieved. These can be made by creating a junction both out of plane [33][34] as well as in plane [35][36].  $WSe_2$  has been used to make an in plane p-n junction with a depletion region of up to 500

nm and a resulting field of  $0.02 \text{ V nm}^{-1}$ . In such a device a responsivity of  $\sim 1 \text{ mA W}^{-1}$  and  $\sim 200 \text{ mA W}^{-1}$  was demonstrated under zero bias and a forward bias respectively [37]. Due to large diffusion length of excitons it is difficult to achieve both wide depletion area as well as a strong built in field to dissociate strongly bound excitons. On the other hand the out of plane heterojunctions made out of one n-type (e.g.  $\text{MoS}_2$ ) and one p-type (e.g.  $\text{WSe}_2$ ) layers can rectify these issues. Such built device can achieve very high in built electric fields of  $\sim 1 \text{ V nm}^{-1}$  and a zero bias responsivity of  $\sim 0.1 \text{ A W}^{-1}$  [34][38].

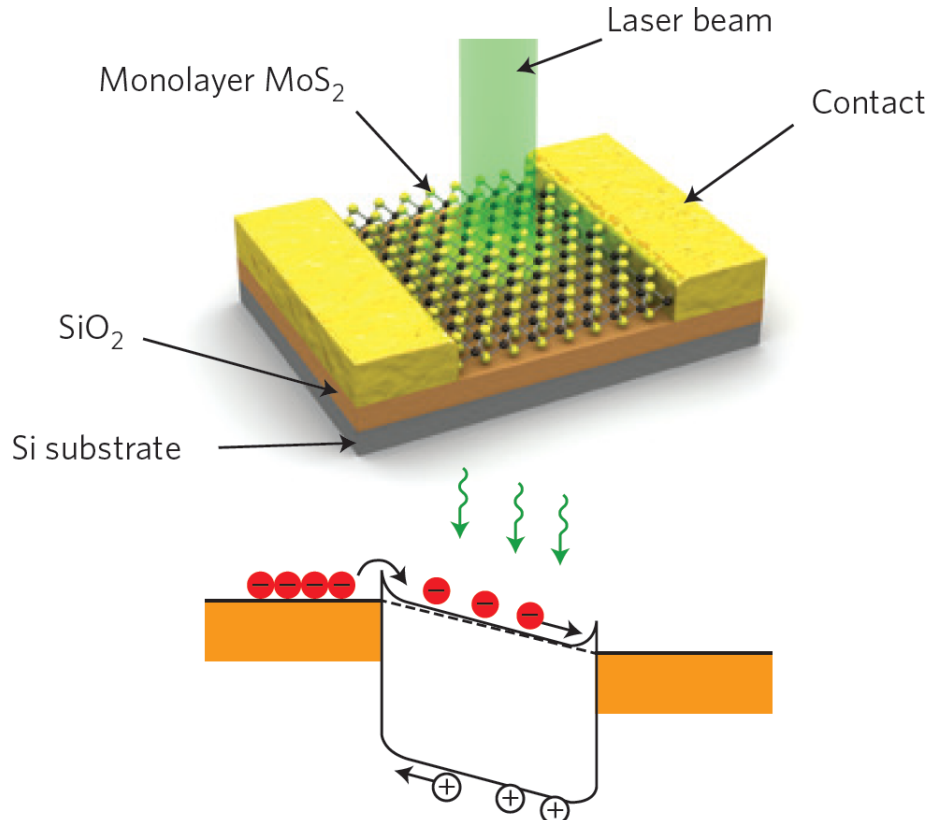


Figure 2.6: Top: Monolayer  $\text{MoS}_2$  lateral photoconductor. Bottom: Band diagram of the monolayer  $\text{MoS}_2$  photodetector. Reproduced from [24]

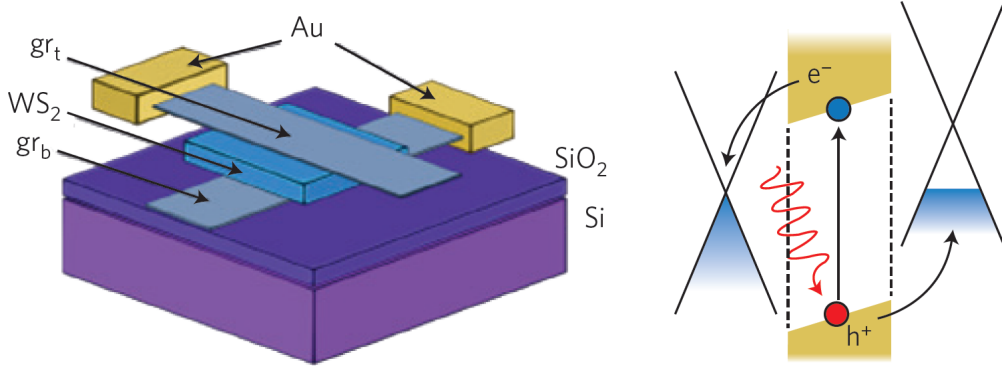


Figure 2.7: Left:  $WS_2$  vertical photoconductor with graphene deposited on top ( $gr_t$ ) and back ( $gr_b$ ) electrodes. Right: Band diagram of a graphene/ $WS_2$ /graphene heterostructure with a built-in electric field. Reproduced from [24]

Table 2.2: Comparison of performances of graphene and 2D TMD photodetectors. Adopted from [24]

	Device type	Responsivity	Bandwidth	Quantum efficiency
Near-infrared to visible gap	Photoconduction			
In-plane	$\sim 1 - 10^3 AW^{-1}$	0.1 Hz to > 10 kHz		$\sim 50\%$ (E)
Strong exciton binding	Out-of-plane	$\sim 0.1 AW^{-1}$	$\leq 200$ GHz	
Mainly based on photovoltaic effect	Heterojunction			
Low dark current	In-plane	$1m AW^{-1}$ (zero bias)	-	$\sim 2\%$ (I) (zero bias)
	Out-of-plane	$\sim 100m AW^{-1}$ (zero bias)	-	$\sim 10-30\%$ (E) (zero bias)

I and E are internal and external quantum efficiencies, respectively. LT, low temperature; RT, room temperature.

## LED

The light emission diodes (LED) and other devices utilising the electroluminescence in layered TMDCs have been realised. A variety of junctions can be formed to allow for the electron-hole recombination and therefore light emission, like Schottky junction [39], p-n junction [35][34][40] or vertical tunnel junctions [33]. Very low current on the order of nanoamps has successfully produced light emission in the in plane junction and efficiency of  $\sim 1\%$  has been demonstrated for the  $WSe_2$  LED [35][40]. It has also been shown that by controlling the injection bias the population of excitons and trions can be manipulated [35][33][24]. It has also been shown that the chirality of the emitted light can be controlled. By applying a strong electric field a p-n junction can spontaneously form and circularly polarised light is emitted. By reversing the direction of the applied field the resulting polarisation of the light also reverses [41]. Wu et al. has demonstrated a laser based on  $WSe_2$  and utilising nanocavities [42]. Similarly by using a disk resonator a  $WS_2$  based laser was made [43] as well as  $MoS_2$  based one [44].

## Photoinduced valley currents

Due to an extra degree of freedom of electrons found in layered TMDCs there has been attempts to utilise it for applications. It has been shown that by illuminating a monolayer of  $MoS_2$  with circularly polarised light an anomalous Hall effect has been observed, indicated by valley-polarised current. The observed voltage sign can be changed by reversing the polarisation of the incoming light[45]. Similarly Yuan et al. has shown that a circularly polarised light when illuminating an electric double layer transistor based on  $WSe_2$  produces valley current. The direction and magnitude of as generated current depends on the polarisation of the light and can be further altered by an external electric field [46].

This area of optoelectronic in regards to layered TMDCs remains still largely unexplored and the exact mechanism of the effects observed is not fully understood. The possible application of the photo induced valley currents however can prove to be interesting, especially as medium for information.

## 2.2 Phonon dispersion

The vibrational and phononic characteristics of TMDCs have been investigated at length by both theoretical simulations as well as experimental studies. The  $2H - MX_2$  crystal structure of the TMDCs belongs to  $D_{6h}^4$  point group and there are 18 lattice dynamical modes at the  $\Gamma$  point. Phonons belonging to these modes can be represented as Eq. 2.2 [47]:

$$\Gamma = A_{1g} + 2A_{2u} + B_{1u} + 2B_{2g} + E_{1g} + 2E_{1u} + E_{2u} + 2E_{2g} \quad (2.2)$$

In TMDCs 4 active Raman modes can be observed  $E_{1g}, E_{2g}^1, E_{2g}^2, A_{1g}$ . These can be seen in Figure 2.8. The  $E_{2g}^2$  is a shear mode that involves 2 layers vibrating against each other. The  $E_{1g}$  is an in-plane vibration of chalcogen atoms but is forbidden in the back-scattering configuration. For monolayers therefore it leaves primarily the  $E_{2g}^1$  which is an in-plane mode involving vibration of both metal and chalcogen atoms as well as  $A_{1g}$  which is an out-of-plane mode involving only chalcogen atoms.

These two peaks tend to dominate the spectrum of any TMDCs, whether monolayer or few-layer or bulk. The shear mode  $E_{2g}^2$  appears at low Raman shift frequencies and is therefore difficult to observe but can be used to differentiate monolayer from few-layer material. Since  $E_{2g}^1$  is an in-plane mode it tends to be unaffected by the number of

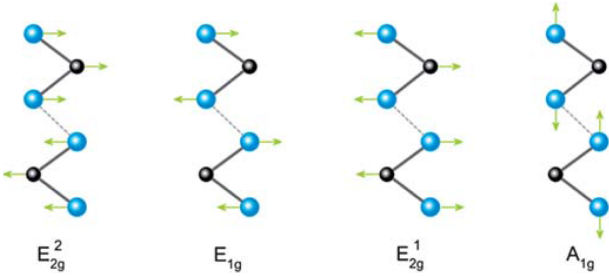


Figure 2.8: 4 active Raman modes in TMDCs. Metal atoms and chalcogen atoms are black and blue respectively. Adopted from [47]

layers due to weak van der Waals forces between the layers but can be seen to be slightly redshifted as the number of layers increases. As seen in Figure 2.9 the  $E_{2g}^1$  peak at about  $352\text{ cm}^{-1}$  is overlapping with another stronger peak, a 2LA(M) peak at  $350\text{ cm}^{-1}$  which is a longitudinal acoustic mode caused by in-plane collective oscillations of W and S atoms. The second strongest peak at around  $416\text{ cm}^{-1}$  is an  $A_{1g}$  peak, caused by out of plane vibrations. Because of that it is much more sensitive to the number of layers and is seen to become blueshifted as the number of layers increases. This has been attributed to the restorative forces as well as increase in dielectric screening of the Coulomb forces. Combining both of these shifts in frequency with the changing number of layers the difference between these two peak position can be used to identify the number of layers in TMDCs as seen in Figure 2.10

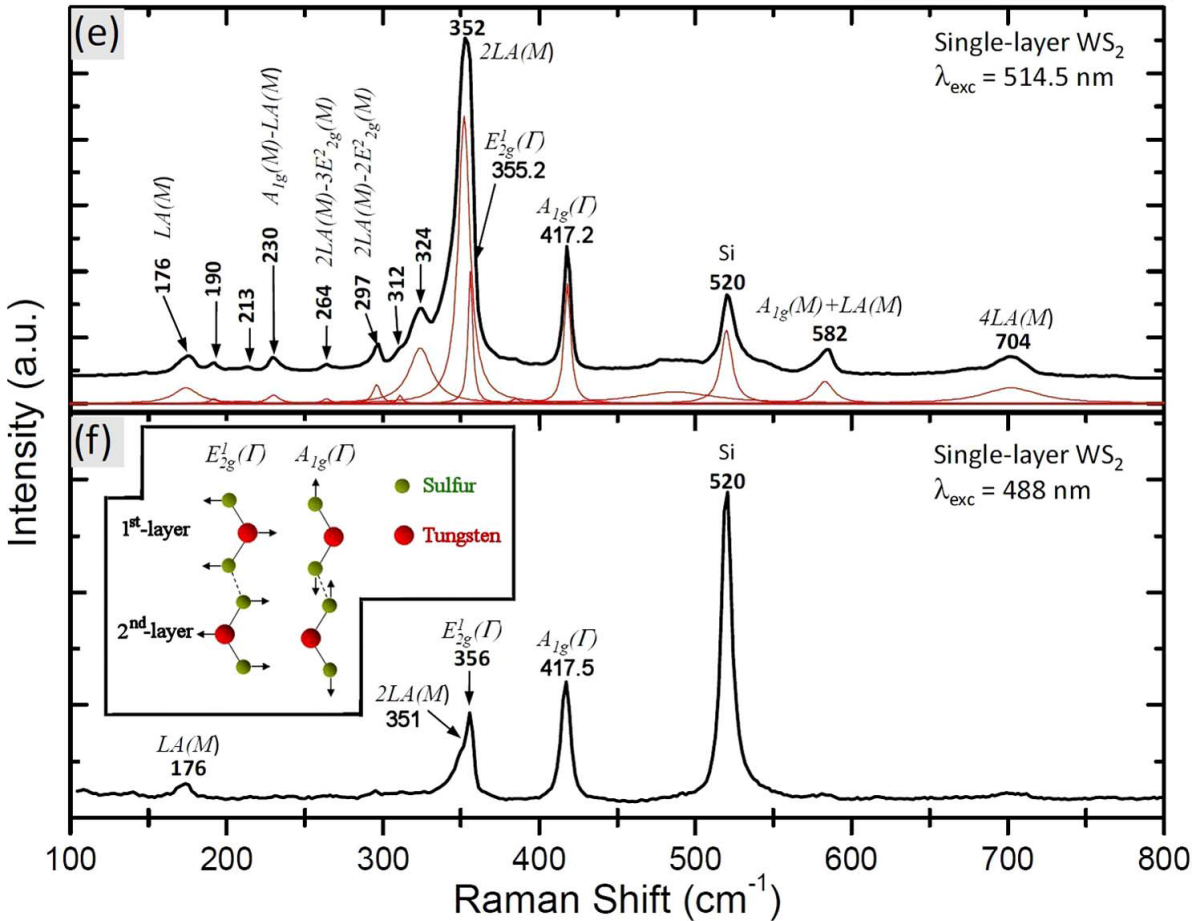


Figure 2.9: Raman spectrum of  $WS_2$  with characteristic peaks indicated. Adopted from [48].

Similarly in  $MoS_2$  the  $E_{2g}^1$  and  $A_{1g}$  peaks can be observed easily using Raman spectroscopy. The position of the monolayer  $E_{2g}^1$  and  $A_{1g}$  peaks are found to be about  $385\text{cm}^{-1}$  and  $403\text{cm}^{-1}$  respectively. Unlike the  $WS_2$  and especially in monolayer form the  $E_{2g}^1$  does not overlap with the 2LA peak which helps greatly with resolving and peak fitting individual peaks. Similarly to the  $WS_2$  the peak position of those two peaks changes with the number of layers in a same manner. As the number of layers increases from monolayer to bulk the  $E_{2g}^1$  shifts a small amount to the red being largely unaffected since that vibrational mode exists in plane and is therefore not influenced by the layer above or below. The  $A_{1g}$  on the other hand, similarly to the  $WS_2$   $A_{1g}$  peak blueshifts by relatively larger amount due to out of plane vibrations which are affected by the number of layers. The separation between those two peaks can be used therefore as an indicator of the number of layers similarly to the  $WS_2$ .

The mono and few layers of  $WSe_2$  has not received nearly as much attention as  $MoS_2$  or  $WS_2$ . The monolayer of  $WSe_2$  shows a bandgap of about 1.7 eV [50] and  $\sim 1$

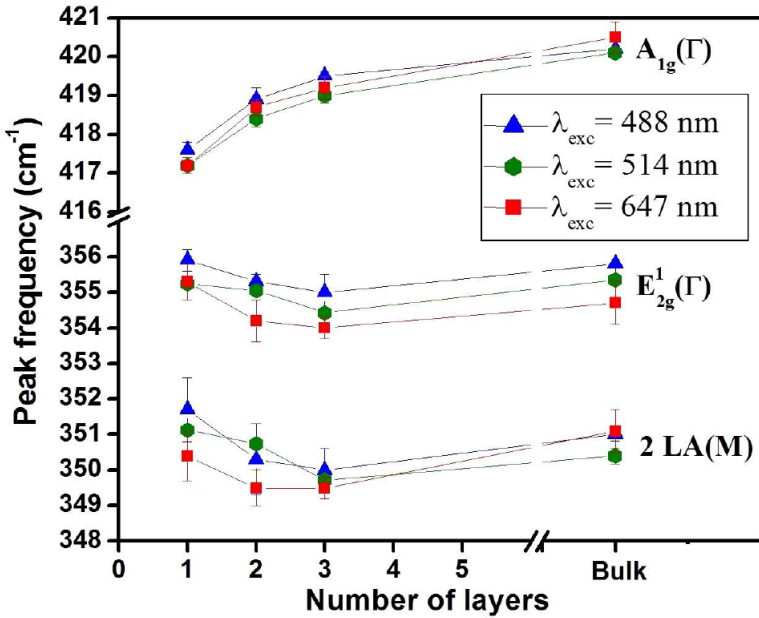


Figure 2.10: Identification of number of layers by the difference in position of  $A_{1g}$  and  $E_{2g}^1$  peaks. Adopted from [48].

eV for bulk and therefore allows for application in electronic and optoelectronic devices operating in near infrared range. As seen in Figure 2.12 the Raman spectrum of  $WSe_2$  shows the 2 main peaks  $E_{2g}^1$  and  $A_{1g}$  at around  $249\text{ cm}^{-1}$  with a 2LA peak at around  $260\text{ cm}^{-1}$ . Because of such proximity between those two peaks the proper peak fitting is made difficult and the peak position separation between  $E_{2g}^1$  and  $A_{1g}$  to determine the number of layers as used for  $WS_2$  and  $MoS_2$  cannot be easily utilised. There is however a breathing mode peak at around  $320\text{ cm}^{-1}$  which is absent from monolayer and present in few layers of  $WSe_2$  and can therefore be used to easily differentiate between mono and few layers of  $WSe_2$ .

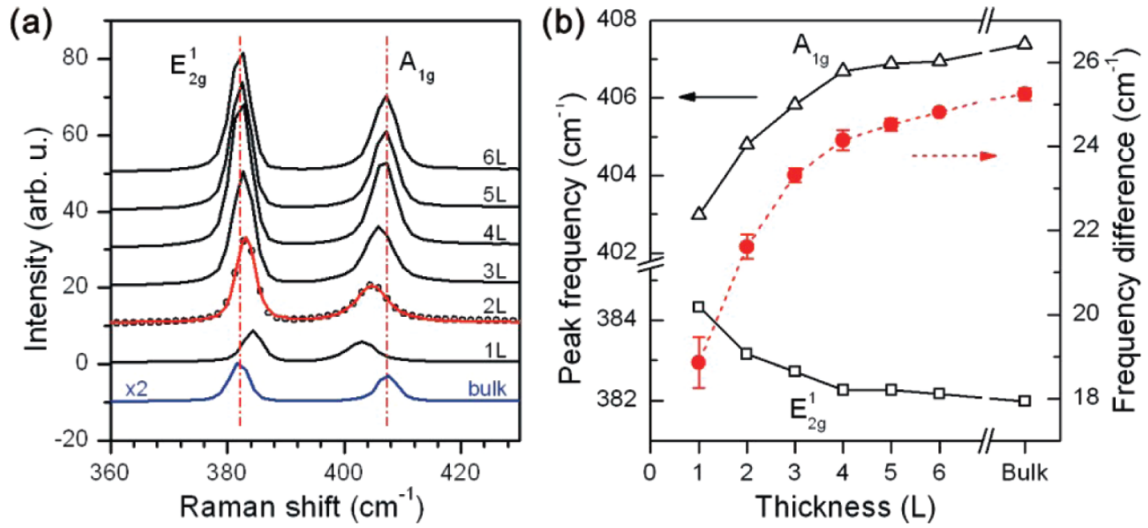


Figure 2.11: a) Raman spectra with of mono and few layers and bulk  $WS_2$  with indicated characteristic peaks b) Characteristic Raman peak position and difference between them as a function of number of layers. Adopted from [49].

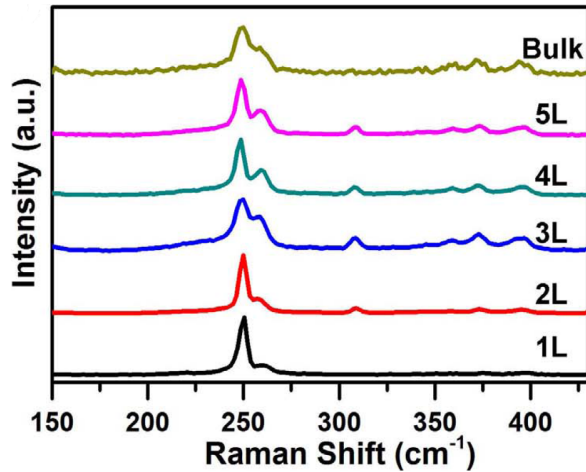


Figure 2.12: Raman spectra of mono and few-layer  $WSe_2$ . Adopted from [51].

## 2.3 Conclusions

In this chapter we have presented and discuss the electronic and vibrational properties on group VI TMDs with a specific focus on  $WS_2$  and  $MoS_2$ . We have summarized the current state of the art which involves experimental and simulation studies. In conclusion mono- and few layer TMDCs have become an important class of materials to study in recent years. Despite their knowledge and usage in bulk forms for many more years their atomically thin form remained largely unexplored. Their particularly interesting properties arise most strikingly when the number of layers is very small. The sulphides and selenides of group VI transition metals (Mo and W) exhibit an indirect to direct bandgap placed in visible to infrared range, high electronic mobilities of  $10^3 \text{ cm}^2\text{V}^{-1}\text{s}^{-1}$ , FET switch ratio of  $> 10^7$  and strain rates up to 20%. Those materials provide therefore a great potential for many applications in electronic and optoelectronic devices for light detection, emission and harvesting. One of the limiting factors in future development of material synthesis and devices is understanding of the TMDCs properties and ability to characterise them easily.

# Chapter 3

## Methodology

### 3.1 Introduction

In order to characterise the synthesised materials and acquire information about the chemistry, crystallinity, morphology as well as its optical and electrical properties a suite of state of the art techniques has to be utilised. An overview of those techniques has been provided in theory and experimental setup.

### 3.2 Raman spectroscopy

Raman spectroscopy is one of the most useful and versatile characterisation techniques for 2D TMDCs due to its non destructive and ease of use. The lack of need to extensively prepare the sample like in some other techniques allows for relatively fast measurements of a large number of samples. Additionally the lack of transfer required results in minimal changes to the material itself as well allows for easier tracking of specific areas of the sample across different techniques. Raman spectroscopy can be used to measure as grown by CVD samples on *Si/SiO<sub>2</sub>* substrate or any other solid substrate as well as liquid solution samples produced by liquid exfoliation.

The Raman spectroscopy can be used to extract information about the chemistry of the material as well as the crystal structure, the number of layers of 2D TMDCs or the strain within the layers.

When a material is irradiated with light the photons generally scatter at different angle but same wavelength. However certain small part of the incident photons (about 1 in 10 million) is scattered at different wavelength than the incident one. This is known as the

Raman effect and the photons that are scattered at wavelengths greater than the incident ones are due to Stokes scattering, while the ones emitted at wavelengths smaller than the incident one are due to anti-Stokes scattering. In the Stokes scattering phenomena the phonon is emitted while during the anti-Stokes scattering the phonon is absorbed as seen in Figure 13.1. In order for the Raman effect to take place a transition between two resonant states must occur. The probability of transition from lower to higher energy state depends on the population of the states. In a thermodynamically stable system the lower energy states are more occupied than the higher energy and therefore the transition from lower to higher is more likely to occur (Stokes scattering). The spectrum of photons scattered as a result of Raman scattering forms what is known as Raman spectrum, where the number of photons scattered is plotted against the photon frequency difference between the incident and the scattered photons. The spectrum is symmetrical around the spectrum origin in regards to the frequency but not in terms of intensity. Because of that only the Stokes part is generally used as a Raman spectrum.

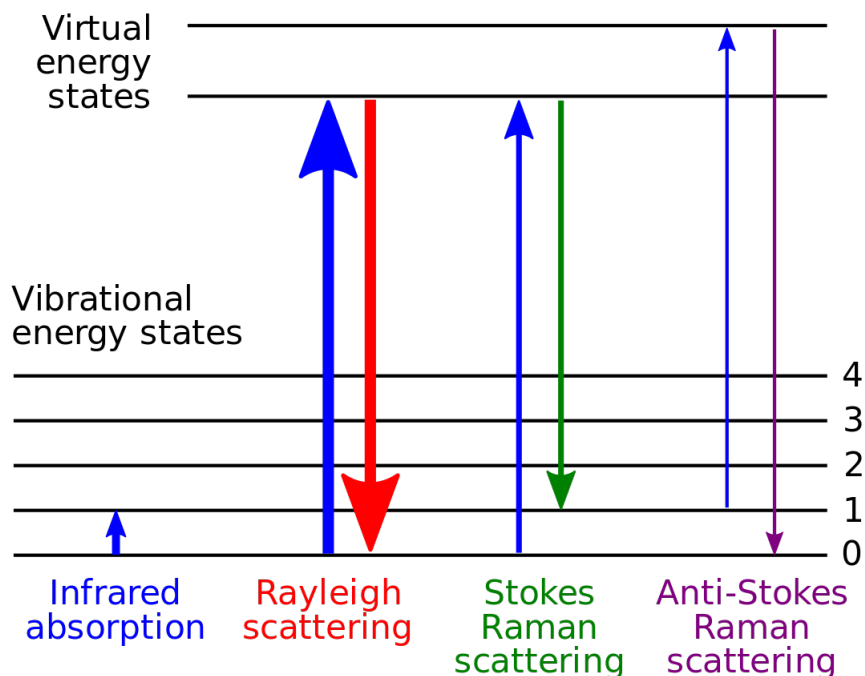


Figure 3.1: An energy diagram comparing elastic and inelastic scattering. Reproduced from en.wikipedia.org

The phonons that are emitted or absorbed during the transitions between the virtual states in the Raman effect are phonons of the vibrational modes in the material. For any solid state crystalline material the point group can be defined. Using the point group

the available vibrational modes can be found. In order for Raman scattering to occur a change in polarisability must occur in a given vibration mode. Similarly if the vibrational mode results in change in dipole moment it results in an IR active mode. As a result a set of available Raman active modes can be found. The Raman spectrum can be therefore used to identify the vibrational modes and therefore gain insight about various factors that influence those vibrational modes.

A typical Raman spectroscope setup involves a monochromatic light source, generally a laser, which is focused on a sample. As a result some of the light is scattered elastically (Rayleigh scattering) while even smaller part is scattered inelastically (Raman scattering). The scattered light is then passed through a filter to remove the elastically scattered light at the wavelength equal to that of the incident photons. The remaining Raman scattered light is passed through a monochromator and then onto a CCD detector. A diagram of a Raman spectroscope can be seen in Figure 13.2.

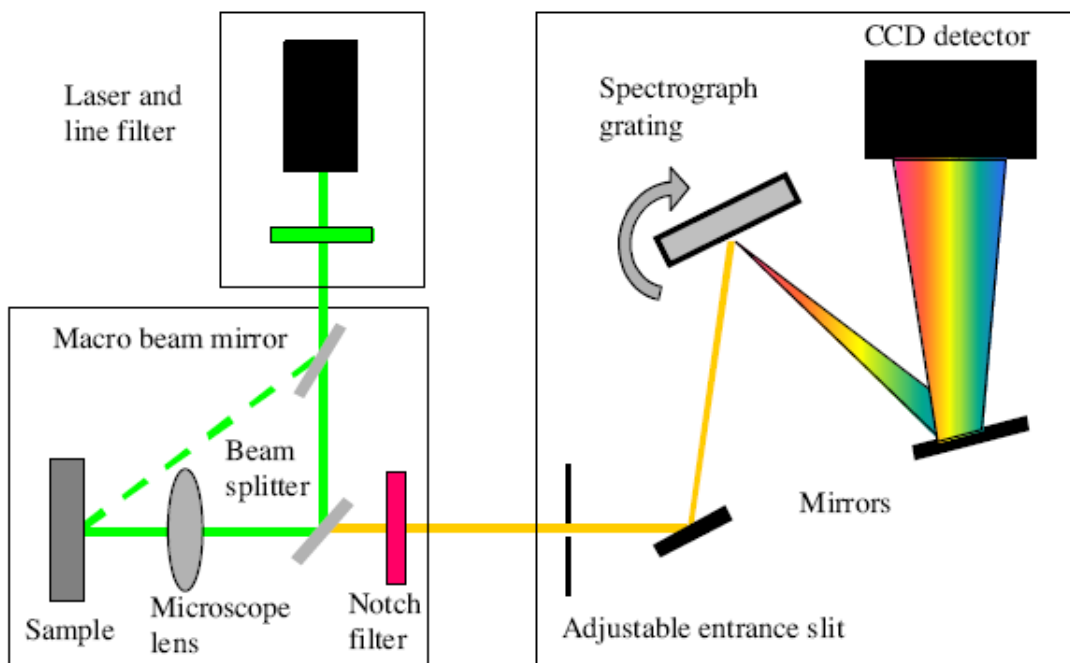


Figure 3.2: A typical Raman spectroscope setup. Reproduced from [www.sas.upenn.edu](http://www.sas.upenn.edu)

A Raman spectrometer used in this work is a Renishaw Raman spectrometer. The 532nm laser was used as a light source in a backscattering geometry. Unless otherwise specified the measurements were taken at room temperature and ambient pressure. An objective lens of 100x with 0.9 numerical aperture was used as the focusing lens. The laser power was set to be 1.6mW with 0.1s acquisition time for mapping and 1s acquisition time

for single spectra. The grating of 1800 lines/mm was used resulting in a resolution of about  $1.5\text{ cm}^{-1}$ . For calibration purposes a silicon sample was used with a peak at  $520\text{ cm}^{-1}$ . All data analysis was performed using MATLAB software.

### 3.3 Photoluminescence spectroscopy

The photoluminescence spectroscopy (PL) is an another versatile non-destructive characterisation technique. When applied to the 2D TMDCs it can provide great insight into the crystal stricture, electronic structure of the material as well as some direct information about its optical properties. One of the great advantages of PL spectroscopy is shared with the Raman spectroscopy in that the sample preparation and handling is very easy and quick allowing for high throughput of characterisation. Unlike Raman spectroscopy a substrate choice might become more important for PL measurements owing to the fact that the conductive substrate might result in PL quenching. Since the bandgap of many of the 2D TMDCs lies within the optical range of the spectrum or near to it a single laser at 532nm can be used to excite the samples.

Photoluminescence is a type of luminescence where an excitation is provided by the incident light. In a semiconducting material like many of the 2D 2H TMDCs the electron from valence band is excited to the conduction band. Following the excitation the electron and resulting hole relax in both energy and momentum to the edge of the conduction and valence band respectively. Thus they form an exciton, a quasi particle that contains no net charge and can move across the material. An exciton in TMDCs can approach large sizes (Wannier-Mott exciton) due to great value of dielectric constant and resulting screening between the electron and the hole. Such exciton can also interact with the material by getting pinned by defect sites. After very short lifetime the exciton recombines emitting the photon at the same time. The photons emitted by the recombining exciton can be then collected. A plot of the photon count versus the energy of the detected photon forms the PL spectrum.

Therefore the PL spectrum can be used to directly infer the optical bandgap which is the electronic band gap of the material minus the binding energy of the exciton. In TMDCs on top of excitons additional type of quasi particle like trions or biexcitons can be found. Those particles exhibit varying level of binding energy and sometimes require special conditions to become excited. The PL spectrum can be therefore used to infer about the presence of those particles and therefore gain insight into the structure of the

material. An energy diagram representing the photoluminescence (fluorescence) process can be seen in Figure 13.3.

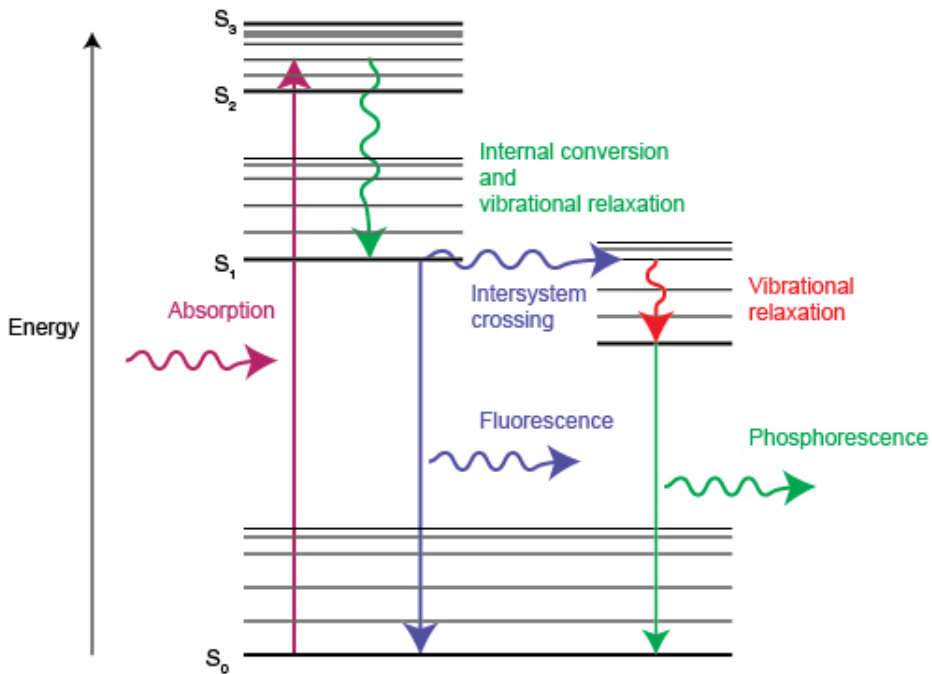


Figure 3.3: The photoluminescence (fluorescence) process. Reproduced from [www.renishaw.com](http://www.renishaw.com)

The PL signal becomes broadened due to variety of factors. One of the most important contributors is temperature which results in Gaussian broadening. At room temperature there is a constant peak broadening of about 25 meV. Because that broadening is relatively close to the binding energy of the trion ( $\sim 30$  meV). Therefore at room temperature the trion peak which is generally weaker than the exciton peak cannot be easily resolved. In order to be able to resolve those peaks a PL measurement at lower temperature can be performed.

A photoluminescence setup can look very similar to that of the Raman setup as seen in Figure 13.2. A monochromatic light source e.g. a laser illuminates the sample at the energy greater than that of the materials bandgap. As a result of that the photons emitted from the material together with the inelastically (Raman) and elastically (Rayleigh) scattered photons pass through a filter to remove the latter. The remaining light is then passed through monochromator and detected at the CCD detector. As a result the PL and Raman spectra can be observed in the same spectrum, provided that the sample material can produce both of those signals.

For low temperature (77K) measurements an environmental stage, Linkam THMS-

350V. A pump was used to lower the pressure in the chamber down to about  $2 \times 10^{-3}$  mbar. The liquid nitrogen was used to cool down the stage down to 77K. The stage was placed in Renishaw Raman spectrometer to capture PL spectra.

The PL spectrometer used in this work is a Renishaw Raman spectrometer. The 532nm green laser with objective lens of 100x with 0.9 numerical aperture was used and the data was recorded in backscattering configuration. The laser power used was 0.32mW with 0.1s exposition time for maps and up to 5s exposition time for a single extended spectrum. The 1800 lines/mm grating was used resulting in a resolution of about  $1.5\text{ cm}^{-1}$ . The spectrum was calibrated using silicon Raman peak at  $520\text{ cm}^{-1}$ . All data analysis was carried out was done using MATLAB software.

### 3.4 X-ray photoelectron spectroscopy

One of the most useful characterisation techniques for study of 2D TMDCs is X-ray photoelectron spectroscopy. It is a non-destructive method which allows to gain information about the chemical composition of the studied material. It is a very surface sensitive method that allows for obtaining signals from about 10 nm of the sample depth. In order to perform the XPS measurement the sample must be placed in high vacuum (about  $10^{-8}$  mbar). It is therefore necessary that the sample contains no liquids or adsorbed gasses which would increase the pressure inside the analysis chamber.

When a sample is irradiated with a beam of x-ray photons some of those photons get absorbed by the electrons in the sample. Because the energy of the incident photons is relatively large the electrons have enough energy to leave the atoms and travel towards the detector. At the detector their kinetic energy is measured. Because the energy of the incident x-ray photons is known and the kinetic energy of the photoelectrons is measured the remaining energy can be calculated using Equation 13.1:

$$E_{binding} = E_{photon} - (E_{kinetic} + \Phi) \quad (3.1)$$

If the  $\Phi$  which is a instrumental correction factor is known then the  $E_{binding}$  can be found. This binding energy depends on the specific atoms from which the electron as well as the specific atomic configuration. Because of that the chemical composition of a given sample surface can be determined. Additionally the number of detected electrons is directly correlated to the concentration of the atoms in the given sample the specific atomic percentages within the scanned area can be calculated. The number of detected

electrons can be then plotted against the calculated corresponding binding energy of the electrons to form an XPS spectrum. A diagram of the XPS physics can be seen in Figure 13.4.

In TMDCs the XPS can be used to determine the stoichiometric composition of the as grown material as well as detect any traces of unintentional doping from alkali or halogen atoms or intentional doping by e.g. In atoms. Additionally the amount of oxides as well as the presence of 2H or 1T phases can be quantitatively determined.

The XPS spectra were collected using the Thermo Scientific K-Alpha XPS system. The Al  $K_{\alpha}$  emission line was used as the x-ray source. The pass energy of 20 eV and the energy step of 0.1 eV were used. The XPS spectra were collected at room temperature and pressure of about  $3 \times 10^{-8}$  mbar. The acquired data was analysed using Avantage software.

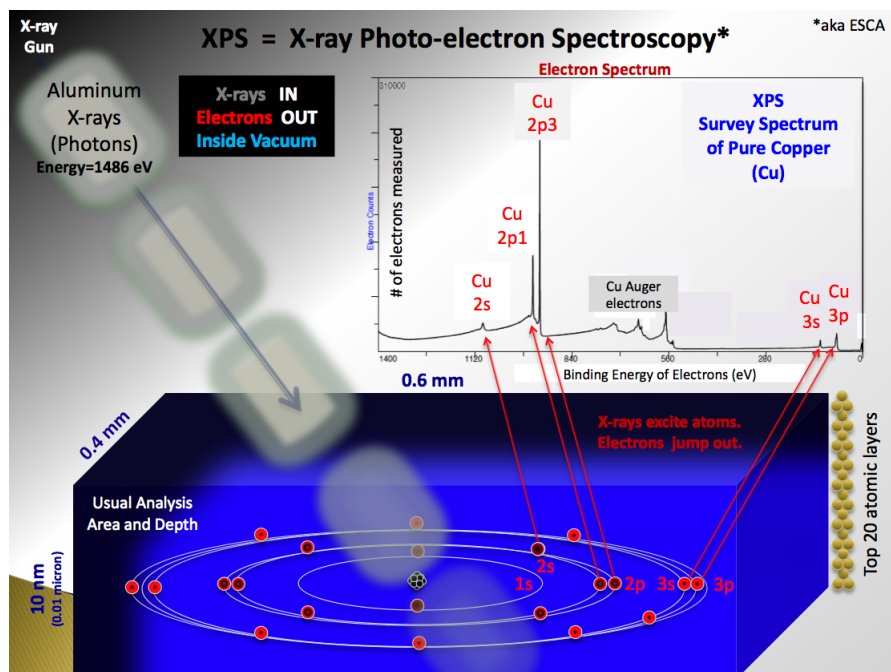


Figure 3.4: XPS spectrum acquisition diagram. Reproduced from en.wikipedia.org

### 3.5 Transfer

Due to the nature of the 2D materials, the 2D TMDCs are generally always deposited on some substrate and cannot be used independently of it. Depending on the manufacturing method different substrates can be used to initially synthesise or deposit the material. In general however the initially used substrate is different to that which can be used

for either characterisation or specific application. The samples synthesised by CVD are grown generally on  $Si/SiO_2$  at very high temperature and as such cannot be readily used in electronic applications due to  $Si$  deterioration at high temperature. To that effect the as grown samples are required to be transferred to a new substrate.

In this work the wet transfer method has been utilised to transfer CVD grown samples from  $Si/SiO_2$  to another  $Si/SiO_2$ , Au or TEM grid substrate. In this method the sample is first spin-coated with a thin layer of PMMA at 3000 RPM for 60 s. After that the sample is dried and heated up to about 50 °C for about 1 hour to ensure full polymerisation. Following that the substrate with the sample is then placed in a bath of 8% KOH solution for about 45 min or until the  $Si$  under the  $SiO_2$  has completely sank to the bottom of the beaker. The thin layer of PMMA with the sample at the bottom is then scooped up with a glass slide and transferred to a DI water to remove the KOH. The sample is held in a water bath for about 30 min and the step is repeated 2-3 more times. After the last dilution step the sample is scooped onto a target substrate. The sample is then gently dried using compressed nitrogen or air to drive any water from between the PMMA and the substrate. The substrate is then heated up to about 50 °C for about an 1h to completely dry the sample of any water and ensure better adhesion to the substrate. The substrate is then placed in a bath of acetone and isopropanol heated up to 60 °C for about an 1h to remove the PMMA layer. After all PMMA has been removed the sample is heated again on a hot plate up to 100 °C to remove any traces of PMMA.

### 3.6 Device fabrication

In order to measure the electric properties of the as-grown materials the material can be used to make a field effect transistor (FET) device. For that purpose the as grown mono- and bi-layer  $WS_2$  was transferred onto a  $Si/SiO_2$  substrate with the  $SiO_2$  layer of 285 nm in thickness. The  $Si$ , which is highly p-doped, then acts as a global gate electrode while the  $SiO_2$  is a gate dielectric. On top of the deposited contacts for source and drain electrodes additional probes were used in each of the FET devices to eliminate any voltage contributions from the contacts and thus allow for correct measurement of the channel conductance. The drain and source drains as well as the voltage drains were deposited using electron beam lithography. The contacts as well as the probes were made using 50 nm thick Au, while the rest of the leads were made using 5nm thick Ti and 50 nm thick Au. Following the contacts and leads deposition the FET devices were annealed at

200 °C fpr 2h under  $H_2/Ar$  (10/90) flow at 1 bar to remove any remaining PMMA from the lithographic process. The sample was then annealed at 115 °C for 60 h under high vacuum ( $10^{-6}$  mbar) to remove any remaining water.

Following the FET preparation the samples were then characterised in a vacuum chamber in high vacuum ( $10^{-6}$  mbar). A low noise source-meter was used to bias the drain electrode with source being grounded. Additionally another source was used to bias the gate electrode. The current across the channel  $I_{ds}$  was measured using ammeter while the voltage  $V_{A-B}$  across the voltage probes was measured with a voltmeter. The gate bias was applied until the measured current reached linear regime where it is described by Equation 13.2 [189]:

$$I_d = \mu_n C_{Ox} \frac{W}{L} (V_{gs} - V_{th}) V_{ds} \quad (3.2)$$

where  $\mu_n$  is electron field effect mobility,  $C_{Ox}$  is the  $SiO_2$  capacitance, W, L are the channel width and length,  $V_{th}$  is the threshold voltage,  $V_{ds}$  and  $V_{gs}$  are the drain-source voltage and gain-source voltage respectively. From the measurement of the current the field-effect mobility for the mono- and bi-layer of the  $WS_2$  can be calculated using the linear part of the plot from Equation 13.3:

$$\mu_n = C_{Ox}^{-1} \frac{d\sigma}{dV_{gs}} \quad (3.3)$$

where  $\sigma$  is the channel conductivity which can be calculated from Equation 13.4:

$$\sigma = \frac{LI_{ds}}{WV_{A-B}} \quad (3.4)$$

and the oxide capacitance  $C_{Ox}$  was calculated to be  $115\mu Fm^{-2}$  using Equation 13.5:

$$C_{Ox} = \frac{\epsilon_0 \epsilon_r}{d_{Ox}} \quad (3.5)$$

where  $\epsilon_0$  and  $\epsilon_r$  are the vacuum and relative permittivity of  $SiO_2$  respectively and  $d_{Ox}$  is the oxide thickness [189].

Additionally the the resistance vs temperature measurements were performed flakes were contacted using two wires configuration. The contacts were deposited using standard photolithographic method by applying the photo resist mask (AZ 5214E) followed by evaporation of Ti (5 nm) and Au (30 nm) using thermal evaporation and sputtering respectively. The measurements were then performed using six arm cryogenic probe station. The measurements were taken at high vacuum of  $10^{-5}$  mbar and liquid nitrogen

temperature. Following the measurements the conductivity was calculated from  $\sigma = \frac{L}{RA}$ , where L is the distance between contacts ( $\sim 3 \mu\text{m}$ ), R is the resistance while A is the flake cross section (0.9 nm -  $40\mu\text{m}$ ). The Keithley 2410 source measure unit as well as Lakeshor temperature controller were used for the measurement.

### 3.7 Scanning electron microscopy (SEM)

Scanning electron microscopy (SEM) is a versatile technique that allows for high resolution imaging of the sample surface. The fundamental operation of the SEM is based on a high energy (1 - 30 keV) electron beam which is rastered across the surface sample under high vacuum ( $< 10^{-5} \text{ mbar}$ ). The incident beam then is scattered by the atoms producing backscattered electrons, secondary electrons, Auger electrons, characteristic x-rays, fluorescent x-rays and continuum x-ray. The backscattered electrons (BSE) are those electrons that undergo elastic scattering during the process and are then measured by the detector. Similarly the secondary electrons (SE) are those electrons that undergo the inelastic scattering and can then, using a different detector to the BSE, be detected and counted. The depth from which the BSE are detected ranges up to  $\sim 100 \text{ nm}$  while that of the SE is limited to  $\sim 10 \text{ nm}$ .

The SEM images were produced using field emission gun SEM (FEG-SEM, Gemini 1525) with an In-Lens SE detector. The FEG-SEM allows for narrower spot size ( $< 5\text{nm}$ ) and a higher signal to noise ratio compared to the conventional thermionic emitters utilised in SEM [190]. Due to the thickness of the  $WS_2$  the SE were primarily used for imaging. Due to the position of the In-Lens SE detector in the electron column with a rotational symmetry around the optical axis it allows for use of low energy ( $\sim 1 - 5 \text{ keV}$ ) for acceleration and close distance. Because of that the contrast between different number of layers can be achieved for some 2D materials [191]. However in order to maintain good signal to noise ratio a slightly higher energy (5 - 10 keV) was utilised.

### 3.8 Atomic force microscopy (AFM)

The atomic force microscopy (AFM) is one of scanning probe microscopy methods that allows for imaging surface morphology below the nm range as well as manipulation and force measurement. As seen in Figure 13.6 the AFM operates by touching and following the sample surface. The probe, which is a very sharply ended tip made of silicon or silicon

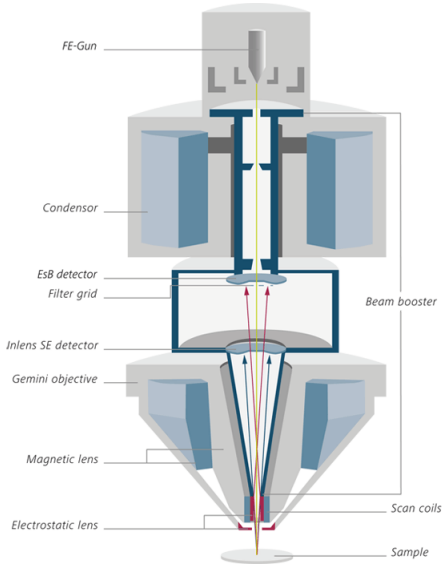


Figure 3.5: Cross section of the SEM optical column. Reproduced from zeiss.com

nitride and a tip radius in the range of nanometers, is mounted on a cantilever. That cantilever is then controlled by a piezoelectric actuator which adjust the position based on the feedback from the laser measuring the actual cantilever deflection. The tip itself when brought close to the surface of the sample experiences a number of possible forces such as van der Waals forces, electrostatic forces, magnetic forces, chemical bond forces or mechanical contact forces which leads to a deflection one way or the other.

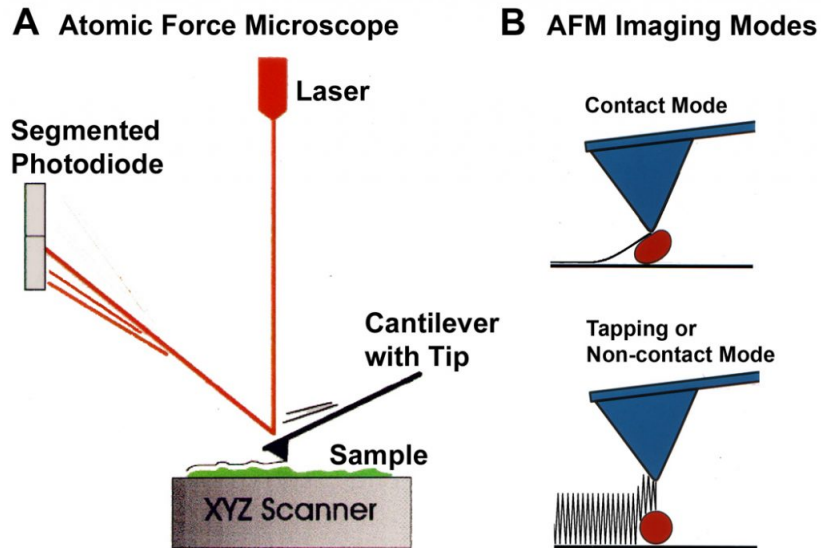


Figure 3.6: Diagram of AFM setup and operating basics. Reproduced from ccem.mcmaster.ca

The measurement can be performed in different modes as seen in Figure 13.6. In

contact mode the tip is dragged along the surface and either a tip deflection is directly measured or a constant height is maintained while the deflection required to maintain it is recorded [192]. Alternatively in a tapping mode the tip is oscillated at a resonant frequency and a constant amplitude is maintained. As the tip gets closer to the surface the forces act stronger and therefore the required correction is recorded and surface morphology and force can be determined. A tapping mode tends to be more useful for characterisation of 2D materials as it avoids damage to them but it is slower and may result in some artefacts [193].

When using tip with radius of  $<5$  nm of curvature a lateral resolution of  $\sim 5$  nm and a vertical resolution of few Å can be achieved. With a contaminated surface the resolution can quickly become bigger and therefore the thickness measurement of the 2D materials can become overestimated. In this work the measurements were carried out using AFM Asylum MFP 3D in a tapping mode with a probe tip made of silicon nitride and a radius of  $\sim 8$  nm on a PPP-NCHR 20 Nanosensors cantilever.

## 3.9 TEM

Transmission electron microscopy (TEM) is a microscopy technique in which a high energy (60-300 kV) electron beam is directed at a very thin ( $<100$  nm) sample. As a result an image of the sample can be produced at resolution much greater than that achieved with optical microscopy due to much smaller wavelength of the electrons compared to the visible photons. As the electron beam passes through the sample it carries information about its electron density, periodicity and phase and can then form an image on a fluorescent screen. The resulting bright field image shows contrast due to variation in thickness across the sample, and as the magnification increases the interaction between the electron beam and the sample becomes more complex giving rise to different types of contrast.

Because the wavelength of the high energy electrons is much smaller than the distance between the atoms in a crystal lattice, the sample can act as a diffraction grating for the incident beam. By shifting the back focal plane instead of the image plane onto the imaging screen and inserting an aperture the diffraction pattern from selected area (SADP) can be achieved. This allows to gain information about the crystal structure and defects within much smaller area than what is possible with x-ray diffraction.

In this work the TEM used was a FEI Titan 80-300 S/TEM at 80kV with a monochromator and  $C_s$  aberration image corrector. The focal series images were produced using

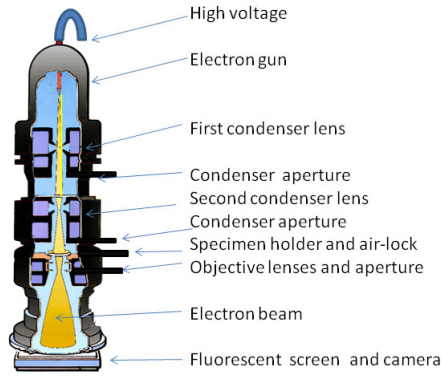


Figure 3.7: Crossection of a TEM column. Reproduced from ccber.ucsb.edu

different objective lens focus values ( $C_s = -4\mu m$ ). Exit wave reconstruction was achieved using TrueImage (FEI).

## 3.10 MATLAB Script

In order to analyse the PL and Raman spectra, both individual and maps, the MATLAB software was utilised. The spectra were exported from the Wire software used for Renishaw Raman spectrometer and they were then imported into MATLAB. Using "peakfit.m" script from "<https://terpconnect.umd.edu/toh/spectrum/peakfit.m>" the peaks were fitted with required number of peaks. For peak fitting the Voigt peakshape was used. Several scripts were developed for the purpose of automating data import, analysis and peak fitting of PL and Raman maps.

# **Chapter 4**

## **$WS_2$ CVD state of the art**

### **4.1 Introduction**

After extensive attention was provided to  $MoS_2$  and its synthesis as well as properties  $WS_2$  has quickly become one of the most studied TMDCs. As a semiconductor its optical bandgap of about 2 eV for monolayer and 1.3 eV in bulk form makes it an interesting material for any electronic and optoelectronic applications. In an atomically thin form its n type semiconductor [4][17][52] and its light emission has been shown to be 50 times that of the  $MoS_2$  [53]. It has also been shown that the valley splitting caused by spin orbit interaction is up to 0.45 eV in  $WS_2$  [54]. Another interesting properties observed strongly in  $WS_2$  is the valley index, referring to the confinement of electrons of the same energy but different momentum to local minima [1]. These and other properties mentioned in Chapter 2 make  $WS_2$  an important material to study. One of the major development hurdles in the field of the TMDCs is the lack of scalable and reproducible method of producing large area samples of TMDCs. Therefore it is imperative to develop a reproducible and scalable method of growing high quality atomically thin TMDCs. This is an overview of latest developments in the field of  $WS_2$  CVD synthesis.

### **4.2 The state of the art**

#### **4.2.1 Bulk crystals**

One of the most popular method of obtaining samples, especially for the purposes of further research, has been mechanical exfoliation from bulk crystals to single or few layer TMDCs. Said bulk crystals can be found naturally or synthesised using a chemical vapour

transport (CVT) method. In this method the precursors are kept in a closed system together with carrier gas and the target substrate and the temperature gradient is applied across the system. The precursor powder (a mixture of metal and chalcogenide precursors) evaporates with the assist of the transport agent to then deposit on the target substrate over the course of days to weeks [55][56]. Utilising this method it has been shown that single bulk crystals of  $WS_2$ ,  $MoS_2$ ,  $WTe_2$ ,  $MoSe_2$ ,  $MoTe_2$  can be grown [55][56][57][58][59][60][61][59]. Such grown crystals are then used to produced single and few layer TMDCs by micromechanical exfoliation and deposition onto a desired substrate. While as produced thin layers show good optical and electronic properties their size, thickness and distribution are not easily controllable.

#### 4.2.2 Thin films of W

Because of that a different method of direct synthesis of thin layers of TMDCs has been used. For the synthesis of  $WS_2$  thin films several different W precursors has been considered. The most common W precursor used is a  $WO_3$  which tends to produce  $WS_2$  samples with very low number of impurities. At the same time however it requires the high temperature ( $\sim 1000$  °C) to evaporate and sulfurise. As an alternative with much lower evaporation temperature ( $\sim 300$  °C) and high volatility the tungsten hexacarbonyl ( $WC_6$ ) can be used. The downside of that precursor however is the potential contamination of the sample with carbon and oxygen. Finally the tungsten halides can form films of high purity, but at the same time their usage results in release of highly corrosive byproducts [55]. As an alternative to regular CVD the metal organic chemical vapour deposition (MOCVD) has been used to produce uniform  $WS_2$  films of  $\sim 65$  nm thickness using  $WC_6$  and  $H_2S$  as precursors [62].

#### 4.2.3 $WO_3$ based CVD of $WS_2$

One of the methods of producing  $WS_2$  thin films is a two step process where a thin film of W or  $WO_3$  is first deposited onto the substrate and subsequently sulphurised. Those thin films of tungsten can be first deposited using electron beam evaporation or magnetron sputtering. In order to produce thin film of  $WO_3$  the as produced W film can be then thermally oxidised. Those thin films of W or  $WO_3$  are then placed in a tubular furnace, like the one used in CVD, heated up to  $\sim 800$  °C and exposed to chalcogen atmosphere. As grown  $WS_2$  films of up to  $\sim 200$  nm in lateral size from W films retain the distribution

and shape of the W films. The  $WS_2$  films produced from  $WO_3$  films showed triangular growths of up to micrometers in size . This suggests that in case of the sulphurisation of the thin layers of  $WO_3$  the W and S species diffuse on the substrate nucleating  $WS_2$  triangles and growing. They can further coalesce with other islands resulting in a wide size and density distribution of  $WS_2$  domains [63][55].

#### 4.2.4 CVD growth of mono and few layer $WS_2$

The CVD approach to growing atomically thin layers of TMDCs have been mostly a single step growth process using metal oxide and chalcogenide powders as precursors [55][53][64][65][66][67][68][69][70][71][72]. For  $WS_2$  growth one of the main challenges in this process is a significant difference of vapour pressure between the W and S precursors. It is therefore crucial to carefully control the evaporation rate of both of the precursors to allow for a degree of reproducibility. In order to do that the usual precursors,  $WO_3$  and S powders, are placed in separate crucibles in a quart tube in a CVD tubular furnace [73][74]. Because of great difference in evaporation temperature of S (100-150°) and  $WO_3$  (800 - 1070°) two separate furnaces are generally used. The growth is generally performed under inert atmosphere of Ar or  $N_2$  owing to high reactivity of S when reducing the  $WO_3$ . The  $H_2$  can be introduced into the process to promote the reduction of  $WO_3$  which can help regulate the shape of the grown samples from jagged edges to smooth triangles [75]. The synthesis of  $WS_2$  can be achieved at both atmospheric pressure as well as low pressure [73][74]. The low pressure growth condition allows for greater volatility of precursors as well as keeps the substrate free of particulates thus leading to more uniform nucleation. The atmospheric growth can however produce good quality  $WS_2$  using metal halides for promoting growth [76]. Thanks to reaction between the metal halides and tungsten oxide species and the subsequent formation of tungsten-oxyhalide species the growth temperature can be brought down to 850 °C [76]. In order to improve the substrate coverage and produce more flakes on the substrate nucleation promoters have been used. By dropping a solution of perylene-3,4,9,10-tetracarboxylic acid tetrapotassium salt (PTAS) onto the substrate and drying it prior to growth of  $WS_2$  a number of PTAS nuclei are formed across the substrate. This promotes the subsequent CVD synthesis of  $WS_2$  via heterogeneous nucleation. It also allows for CVD synthesis on a variety of surfaces (sapphire, quartz, silicon) with different surface corrugation [77]. The growth temperature has also been shown to have great effect on the flake size with a change from 880 °C to 900 °C resulting

in later size of flakes increasing from  $\sim 5\mu m$  to  $\sim 50\mu m$  [75]. Different approaches to heating the precursors as well as precursor and substrate placement have also been proposed. By placing both  $WO_3$  and  $S$  precursors in the same furnace, with  $WO_3$  in the centre and  $S$  at the edge small triangles with anisotropic PL signal across the flake have been observed. The variation in PL has been attributed to S deficiencies resulting from premature evaporation of the S precursor [53]. It has also been shown that by spreading  $WO_3$  powder onto one  $Si$  wafer positioned in the centre of the furnace and placing target substrate above it and facing it with S precursor in a separate heating element a successful growth can be achieved. The resulting flakes however showed a wide range of both lateral sizes as well as thickness with monolayer flakes showing uniform PL signal across the flake [64]. A CVD synthesis was performed on a hBN substrate using  $WCl_6$  as a tungsten precursor with flakes up to  $3\mu m$  and narrow PL emission (26 meV) centred around 2.01 eV [78]. In order to grow large area monolayer flakes  $WS_2$  Rong et al. has shown that by controlling the S evaporation time and therefore presulphurising the  $WO_3$  powders by 10 min flakes of up to  $370\mu m$  were grown [65].

At the same time the CVD growth of  $WSe_2$  has proven to be much more difficult. The most common strategy involves the use of  $H_2Se$  as the Se source which is a corrosive and extremely toxic gas. Because of that there is need to find substitutes to limit any possible exposure. There has been some successful growths using  $Se$  powders but the growth is often limited by low reactivity of Se, especially compared to S [79][80][76]. The resulting flakes therefore tend to be on the size order of 20-30  $\mu m$ . There is therefore room for further study and improvements to achieve bigger flakes with better substrate coverage.

### 4.3 Conclusions

In conclusion there has been a tremendous push in the area of CVD growth of mono and few layer TMDCs. Especially in case of  $MoS_2$  and  $WS_2$  many discoveries have been made regarding the mechanism responsible for the nucleation, growth, precursors evaporation and transport. Many strategies however manage often to optimise one parameter at cost of others and therefore no one of those methods can be easily utilised for scalable production for future applications. In case of less popular TMDCs like  $WSe_2$  there is even more that needs to be discovered to achieve parity with the established techniques for more common TMDCs.

# Chapter 5

## The state-of-the-art of bilayer heterostructure of $MoS_2/WS_2$

### 5.1 Introduction

As two-dimensional TMDCs have emerged as promising candidate materials for next-generation electronic and optoelectronic technologies with valley functionalities it has become apparent the need of enhancing some of their properties in view of their applications. For instance, creating band offsets between different monolayer TMDCs would enable efficient separation of charge carriers and rectification of charge flow. This would offer a mechanism for designing devices made by entirely van der Waals atomically thin materials. Furthermore, the semiconducting monolayer TMDCs —  $MoS_2$ ,  $MoSe_2$ ,  $WS_2$  and  $WSe_2$  — are also interesting because they possess direct bandgap in the visible region at energy degenerate band edges (valleys), spin–valley coupling and valley-contrasting electronic and excitonic properties. The valley physics of TMDC excitons have been intensely studied in the past few years, with recent advances including the optical generation and control of exciton valley coherence. However, as the valley degree of freedom is affected by very fast recombination time (picosecond timescale) would impede any possible exploitation of the valley-functional optoelectronic devices based on valley excitons in monolayer TMDCs in practical applications. The fabrication of bilayered van der Waals (vdW) heterostructures would enable to fully exploit the potential of TMDC in electronic, opto and valleytronic applications.

## 5.2 Properties of bilayer heterostructures

As it has been explained in Chapter 2, TMDCs undergo a crossover from indirect bandgap in the bulk to direct bandgap in the monolayer form. As a consequence of this direct band gap, monolayers absorb and emit light rather efficiently. The band structure changes as a function of the number of layers due to the strong interlayer coupling, which results in different shifts in the conduction and valence band edges at various symmetry points in the Brillouin zone as a function of the layer number [2]. Vertical TMDCs heterostructures formed by stacking up different monolayers offer a rich collection of physics and functionalities. Theory predicts that any stacked  $MX_2$  heterostructures form type II semiconductor heterojunctions and thus it facilitate efficient electron–hole separation [81]. This would be particularly beneficial for light harvesting and light detection applications. It has been further demonstrated that the charge separation can occurs over ultra fast time scales, such as femtosecond [82]. In type II semiconductor heterojunctions, the conduction band minimum and valence band maximum are found in two separate materials. If electrons and holes are photoexcited they will then prefer to stay in different materials. The alignment of electronic bands of  $MoS_2$  and  $WS_2$  monolayers as predicted [83] is reported in Figure 4.1. It shows that monolayer  $MoS_2$  and  $WS_2$  have bandgaps of 2.39 eV and 2.31 eV, respectively, and the  $MoS_2$  valence band maximum is 350 meV lower than that of  $WS_2$  and the conduction band level is also lower. Thus in this material system, the conduction band minimum resides in  $MoS_2$  and the valence band maximum in  $WS_2$ . This heterojunction structure can lead to efficient charge transfer upon optical excitation with separated electrons and holes residing in two layers. Hong et al has demonstrated that the electron-hole separation occurs in 50 fs [82]. The fast separation can be particular beneficial in solar-driven applications such as photoelectron catalysis and solar cells as it reduces the chances of immediate recombination of the charges. We have demonstrated that the formation of this type of heterojunction of chemically exfoliated  $MoS_2/WS_2$  and assembled in a form of thin films can be beneficial for photoelectrochemical water splitting. In Chapter 12 we discuss the formation of  $MoS_2/WS_2$  heterostructures in the form of thin films via CVD and their identification via physical characterization. The same structures have been used for photoelectrochemical water splitting. In general, the most studied bilayer heterostructures is formed by  $MoS_2$  and  $WS_2$  monolayers. This is due to the fact that synthesis of these materials via CVD is better established as compared to the selenides materials.

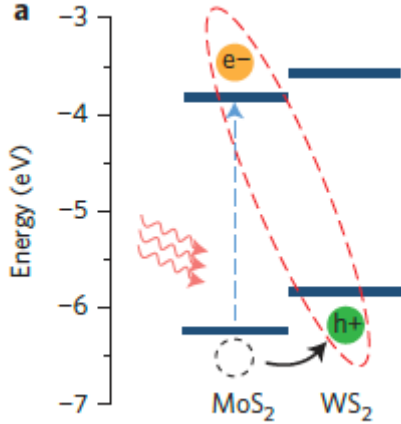


Figure 5.1: Charge separation across heterojunction following photoabsorption. Adopted from [82]

### 5.3 Fabrication of bilayer heterostructures

The first studies of heterostructures of TMDCs have been based on CVD materials. Two different approaches have been adopted. The first strategy was based on the transfer of two monolayers priorly synthesized independently. While the second approach, which has not seen nearly any further work on, was based on the direct synthesis of heterostructures via CVD.

#### Transfer -approach

*WS<sub>2</sub>/MoS<sub>2</sub>* heterostructures have been prepared from conventional PDMS stamping method from CVD grown monolayers [84]. In the first report about this [85], *MoS<sub>2</sub>* and *WS<sub>2</sub>* monolayers have been grown by high-pressure CVD technique onto *SiO<sub>2</sub>/Si* substrates. The CVD *MoS<sub>2</sub>* monolayers were continuous over 1mm with large, single-domain crystals reaching up to 75 microns while the CVD *WS<sub>2</sub>* monolayers were in the form of individual triangle islands of 5-50 microns in size. The fabrication process consisted in a first transfer of the *WS<sub>2</sub>* monolayers onto PDMS substrates, followed by stamping the *WS<sub>2</sub>* monolayers onto CVD *MoS<sub>2</sub>* monolayers, which formed vertical heterostructures of *WS<sub>2</sub>/MoS<sub>2</sub>* [84]. The overlap region (approximately 40  $\mu\text{m}$ ) of *MoS<sub>2</sub>* and *WS<sub>2</sub>* monolayers show slightly darker contrast under the optical microscope and it is the region which has been characterized by Raman spectroscopy and photoluminescence and electrical measurements.

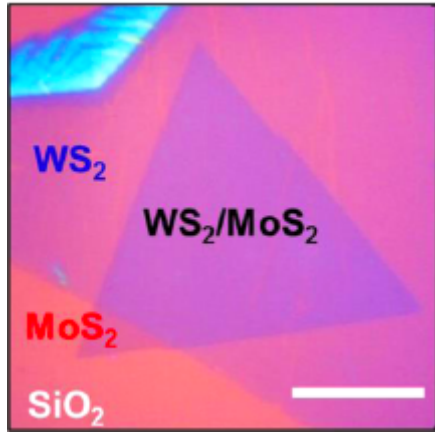


Figure 5.2: Optical micrograph of the heterostructure of  $WS_2/MoS_2$ . Adopted from [84].

### Direct synthesis of vertical heterostructures

Firstly, with the term, vertical heterostructures, we differentiate those from the lateral heterojunction created by two adjacent and consecutive layers of two different TMDs. This terminology differentiates these two different types of heterojunction which can be obtained by direct CVD synthesis. The direct synthesis of bilayer heterostructures have been obtained via CVD where molybdenum trioxide ( $MoO_3$ ) powder was placed in front of a bare  $SiO_2/Si$  wafer for the growth of  $MoS_2$  in a tubular furnace. A mixed powder of tungsten and tellurium was scattered on the wafer for the growth of  $WS_2$ . A small amount of tellurium was used to accelerate the melting of tungsten powder during the growth [85]. Upstream in a low-temperature zone, the sulphur powder was placed. The furnace was heated up to the temperature range of 650-850 °C and argon gas was used as a carrier gas to protect the system from oxygen and carry sulphur vapour from the upstream of the tube during the reaction. The difference in the nucleation and growth rates of  $MoS_2$  and  $WS_2$  and the chosen growth temperature favours the sequential growth of  $MoS_2$  and  $WS_2$ , instead of the formation of their ternary alloy ( $Mo_xW_{1-x}S_2$  alloy). Vertically stacked bilayers were found to grow preferentially at temperature of 850 °C, whereas in-plane lateral heterojunctions were found at 650 °C. The CVD synthesis can lead to clean interfaces [85][our paper submitted ] between the two monolayer components, in contrast with mechanical transfer of layers or assembly from liquid phase. A typical optical, SEM and atomic force microscopy (AFM) images of the layers are shown in Figure 4.3. The bilayers can be easily distinguished from monolayers via optical contrast (Figure 4.3), with  $MoS_2$  monolayers showing a light purple colour and the bilayer regions a much darker purple.

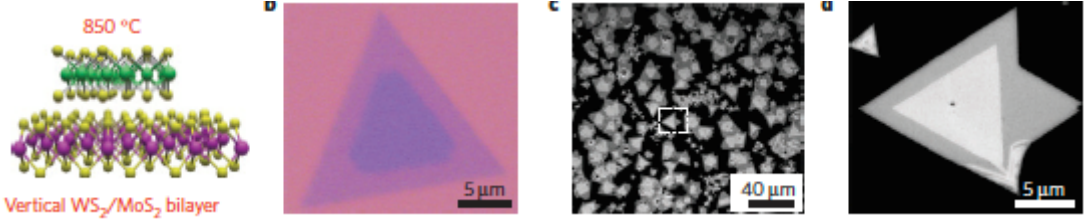


Figure 5.3: Heterostructure imaging. Adopted from [85].

## 5.4 Characterization of bilayer heterostructures

### 5.4.1 Raman spectroscopy

Heterostructures fabricated by both these approaches were characterized by Raman spectroscopy. As the vibrational modes of  $MoS_2$  and  $WS_2$  are quite different the Raman spectrum of the heterostructure displays in-plane ( $E_{2g}^1$ ) and out-of-plane ( $A_{1g}$ ) modes of  $MoS_2$  and  $WS_2$  at the same frequencies as in their monolayers. The  $WS_2$   $E_{2g}^1$  and  $A_{1g}$  modes are located at  $350\text{ cm}^{-1}$  and  $416\text{ cm}^{-1}$  while for  $MoS_2$  they are at  $380\text{ cm}^{-1}$  and  $405\text{ cm}^{-1}$  respectively [84]. Spatial maps show consistently distinct signal from each of the two layers using both fabrication techniques (Figure 4.4). In the transferred bilayered heterostructures there is a clear difference between the Raman modes position of the as transferred materials versus an annealed heterostructure. The position of the peaks for each material in the as transferred materials is compatible with monolayers while after annealing (at the temperature of  $70\text{ }^\circ\text{C}$ ) the peaks are affected by redshift/blueshift as it is characteristics of bilayer materials. This result suggest that as a consequence of annealing ( $120\text{ }^\circ\text{C}$  at  $<0.13\text{Pa}$  for 6 h) there is an increased interlayer interaction. The fact that no changes are observed in the E modes in plane can be explained with the fact that they are generally less sensitive to changes in the environment. The increased interaction has been also revealed by AFM where the step height of the bilayer heterostructure can be reduced from 1.6 nm toward the expected 0.8 nm by annealing. This can be explained with the possibility that such annealing is able to drive out trapped residual molecules, such as water. In the CVD grown materials, the  $A_{1g}$  Raman peaks appears at  $418.5\text{ cm}^{-1}$  and  $405.3\text{ cm}^{-1}$  respectively for  $WS_2$  and  $MoS_2$ . These values are compatible with a bilayer structures of the annealed transferred samples. This suggest there is an increased interaction between the layers in CVD grown materials in line with layered bulk materials [84].

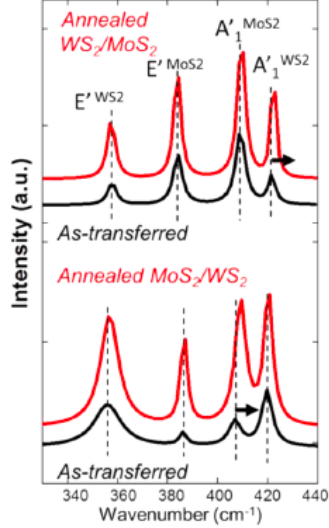


Figure 5.4: Heterostructure Raman spectrum. Adopted from [84].

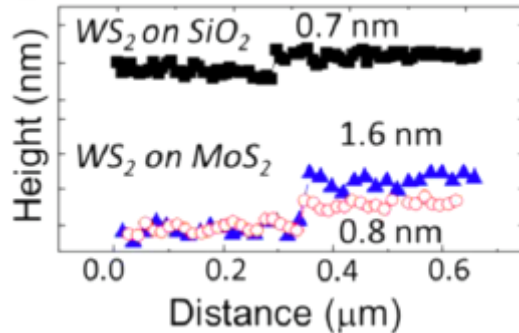


Figure 5.5: Comparison of AFM profiles of  $WS_2$  on  $Si/SiO_2$  and  $MoS_2$ . Adopted from [84].

### 5.4.2 Photoluminescence

The vertical heterostructures were further characterized by photoluminescence (PL) spectroscopy. The as transferred heterostructures manifest PL peak typical of  $MoS_2$  and  $WS_2$ . The spectrum can be defined as additive. The PL peak of  $MoS_2$  show intensity much higher  $WS_2$  and this was attributed to possibly higher density of defects in  $WS_2$  associated with its higher growth temperatures. After annealing the  $WS_2/MoS_2$  heterostructures, the PL spectrum gradually changes. The transition as seen in Figure 4.6 from transferred to fully annealed bilayer heterostructures occur through the followings: (1) A new PL peak ( $P_{hetero}$ ) appears at 1.94 eV, and its integrated intensity grows for prolonged annealing time. (2) Upon the annealing,  $P_{MoS_2}$  and  $P_{WS_2}$  gradually decrease up to the point of appearing as small features at lower and higher energy of the  $P_{hetero}$  peak (3) at the end

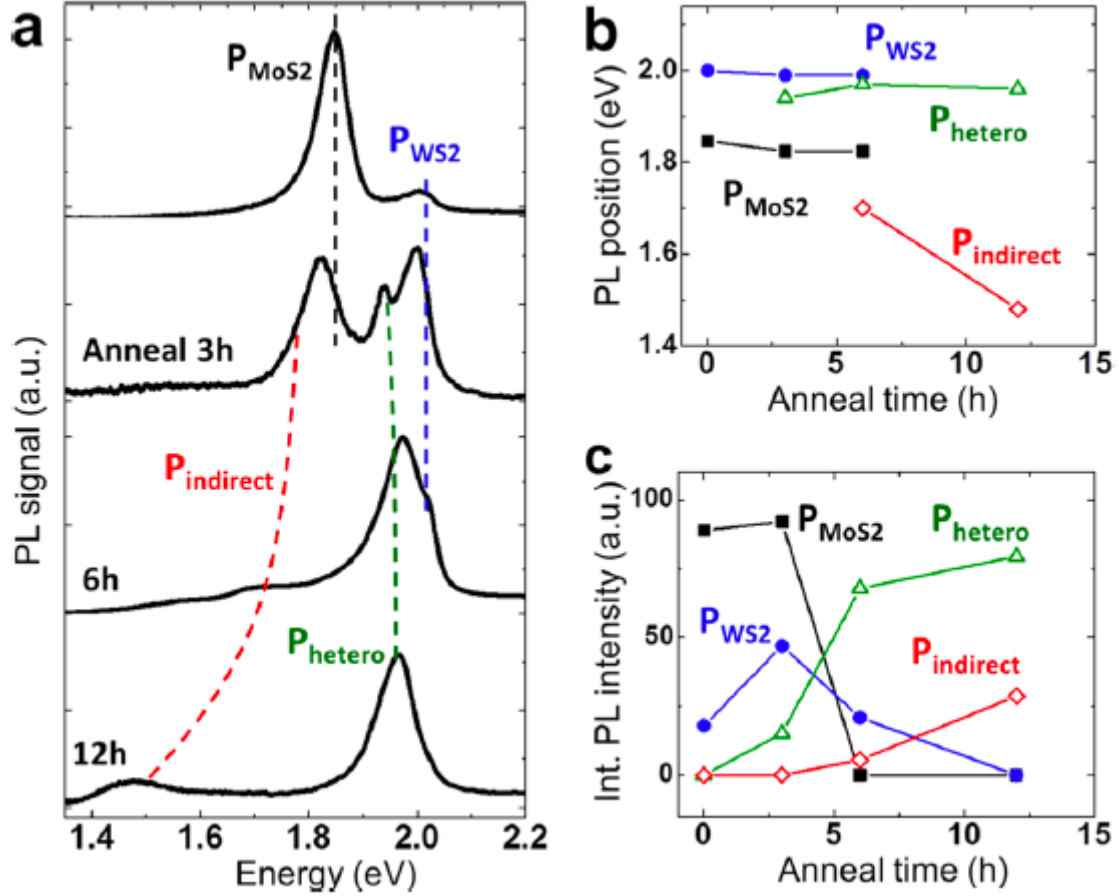


Figure 5.6: PL Spectrum of heterostructure after annealing. Adopted from [84].

of 12 hours of annealing, another weak emission peak ( $P_{indirect}$ ) appears at 1.75 eV, and the peak position rapidly and eventually red-shifts to 1.5 eV [84].

The explanation for this trend has been the following. As a consequence of the transfer the two monolayers end up well separated from each other due to residual water molecules and/or impurities trapped between the sheets. This large distance has been assessed by AFM (Figure 4.5). This system display PL peaks characteristics of isolated monolayer  $MoS_2$  ( $P_{MoS_2}$ ) and monolayer  $WS_2$  ( $P_{WS_2}$ ). After the annealing, the PL peak intensity of  $MoS_2$  ( $P_{MoS_2}$ ) and  $WS_2$  ( $P_{WS_2}$ ) decreases and two new peaks appear, called  $P_{hetero}$  and  $P_{indirect}$ , with the former arising from the electronic coupling between the two monolayer materials while the latter arising due to the indirect band gap formed at the interface of the heterobilayer (Figure 4.7). Because the  $P_{indirect}$  peak position changes rapidly with the degree of coupling (annealing time). This has been attributed to a phonon-assisted, indirect bandgap transition, which involves the valence band maximum (VBM) at the  $\Gamma$ -point and the conduction band minimum (CBM) at the K-point. To prove this

hypothesis, the authors have fabricated by transfer method a  $MoS_2/MoS_2$  heterostructure and the indirect peak has similar behaviour. This suggested that the indirect peak can be associated with a similar behaviour as the bulk material. DFT calculations has supported this hypothesis [86]. The formation of a type II heterojunction led to establishing a large electric field which develops across the 1 nm thick junction. This leads to strong exciton splitting by which holes (electrons) are rapidly swept from  $MoS_2$  to  $WS_2$  (from  $WS_2$  to  $MoS_2$ ).

In order to understand the interlayer interactions DFT simulations have been performed. It has been observed that the twist angle between 2 layers has an effect on several properties of the TMDCs. By twisting the layers from being aligned at  $0^\circ$  to  $30^\circ$  the distance between the layers increases by about  $0.3 \text{ \AA}$ . The trend then reverses with distance returning back at  $60^\circ$  to the same value as at the  $0^\circ$ . Additionally it has been predicted that as the twist angle changes from  $0^\circ$  to  $30^\circ$  the valence band at K point remains mostly unchanged while the valence band at  $\Gamma$  point rises. Due to this the direct transition K-K remains unchanged while the indirect K- $\Gamma$  transition shows lower energy gap. As an explanation of that phenomenon it has been noted that the both valence and conduction band states at K point involve primarily  $Mo$  states that are located within the layer. The valence state at the  $\Gamma$  point however involves appreciable  $p_z$  content of  $S$  atoms and  $Mo - d_z^2$ . Because of that the overlap between those  $p_z$  states of  $S$  atoms varies significantly with the layer separation [87].

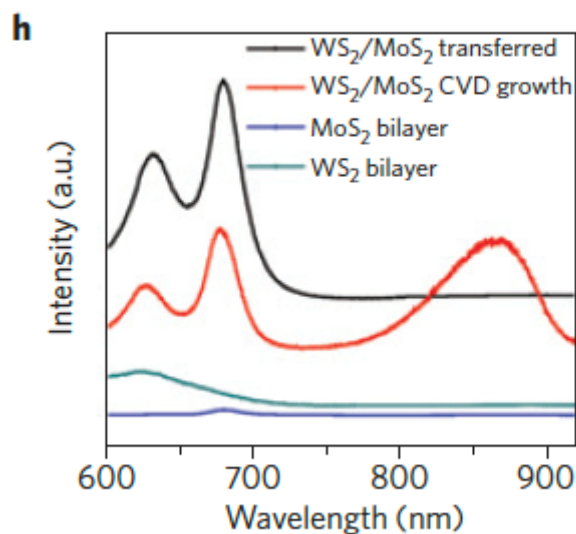


Figure 5.7: Comparison of PL spectra from hetero and homo bilayers of  $WS_2$  and  $MoS_2$ . Adopted from [85].

The CVD grown heterostructures shows a bandgap of 1.42 eV while at the same time separate pronounced PL peaks of  $MoS_2$  and  $WS_2$  can be seen (Figure 4.8) [85]. Subsequent studies have tremendously developed the understanding of the heterobilayer PL behaviour. The main factor which has been taken into consideration in the following studies is the mismatch angle between the lattices orientations of the two monolayers. Experimentally, it was found that the twist angle in a heterobilayer determines the photoluminescence efficiency of interlayer excitons (bound electrons and holes situated in adjacent layers) and their peak position. It has been hypothesized that twist-angle-dependent interlayer orbital hybridization can cause the variation in the photon emission energies of indirect excitons in heterobilayers (e.g.  $MoS_2/WSe_2$ ) and also in  $MoS_2$  bilayers [87]. Additional experimental work has reported similar results [88][89].

Specifically, in a study by Kunstamnn [90] the heterobilayer region of  $MoS_2/WSe_2$  shows the peaks of the two individual materials are discernible among with a new peak near 1.6 eV. This has been interpreted as the indirect exciton, and renamed as interlayer exciton (ILE). By altering the twist angle between the  $MoSe_2$  and  $WSe_2$  layers from  $0^\circ$  to  $30^\circ$  the ILE peak intensity has decreased and further from  $30^\circ$  to  $60^\circ$  the intensity has increased again. Similarly the ILE peak position has blueshifted from  $0^\circ$  to  $30^\circ$  and redshifted back from  $30^\circ$  to  $60^\circ$ . The separation between the layers is also found to be highest at about  $30^\circ$  and smallest at  $0^\circ$  or  $60^\circ$ . At the same time the other PL peaks, associated with monolayer  $WSe_2$  and  $MoS_2$ , are unaffected. The ILEs can be therefore associated with the K- $\Gamma$  transition.

Very recently, Alexeev et al [91] have shown the latest achievement in the field consist of bilayered TMDs heterostructures formed by transfer of CVD grown TMD as well as mechanically exfoliated. It has been shown that in the  $WSe_2/MoS_2$  heterostructure the PL peak associated with  $MoS_2$  monolayer redshifts while the one of the  $WSe_2$  monolayer remains largely unaffected. Additionally as the twist between the layers increases from  $0^\circ$  to  $60^\circ$  the position of that PL peak increases initially and plateaus soon after and drops again near the  $60^\circ$  twist. It has been then suggested that a strong hybridazation takes place between interlayer and intralayer excitons. The Moiré pattern formed by twisting the layers results in formation of mini Brillouin zones. Those mini Brillouin zones (mBZ) at small angle twists result in additional interlayer peaks. Those additional peaks are very strongly twist angle dependent and become less intense and more blueshifted at higher twist angles.

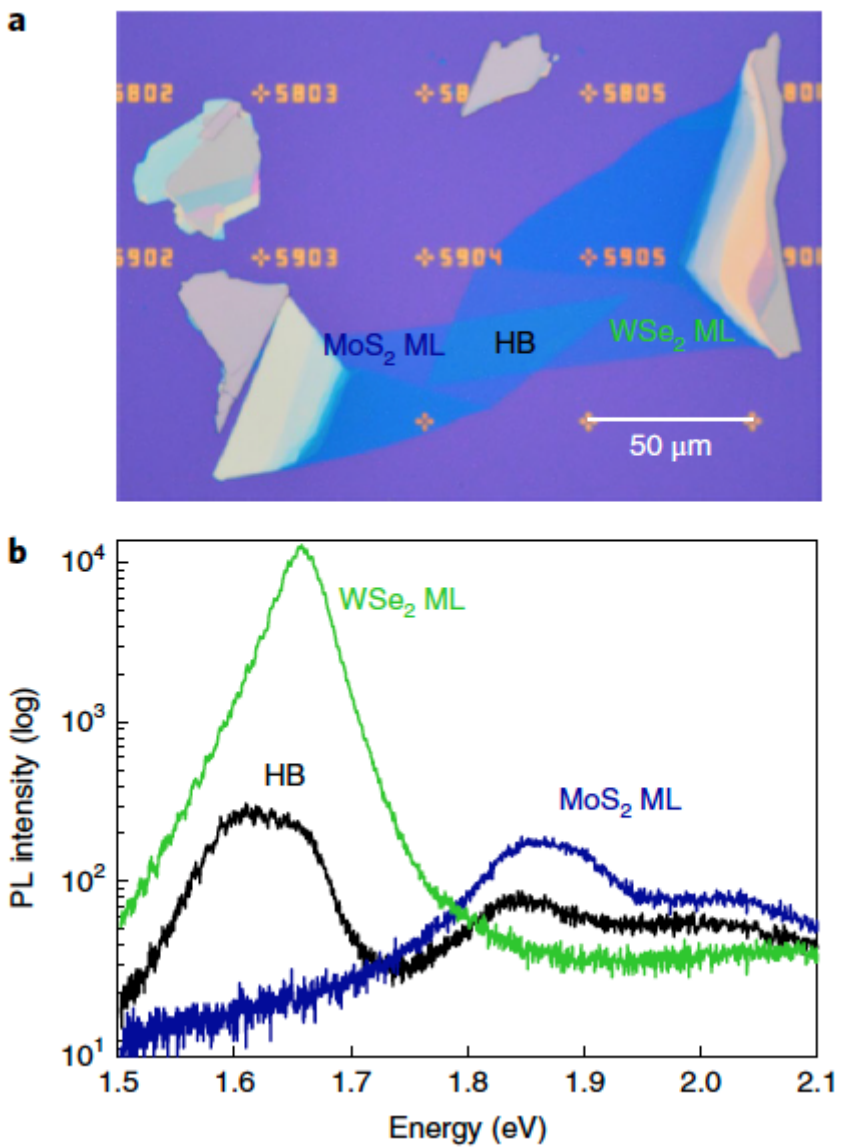


Figure 5.8: PL spectra taken from heterostructure. Adopted from [90]

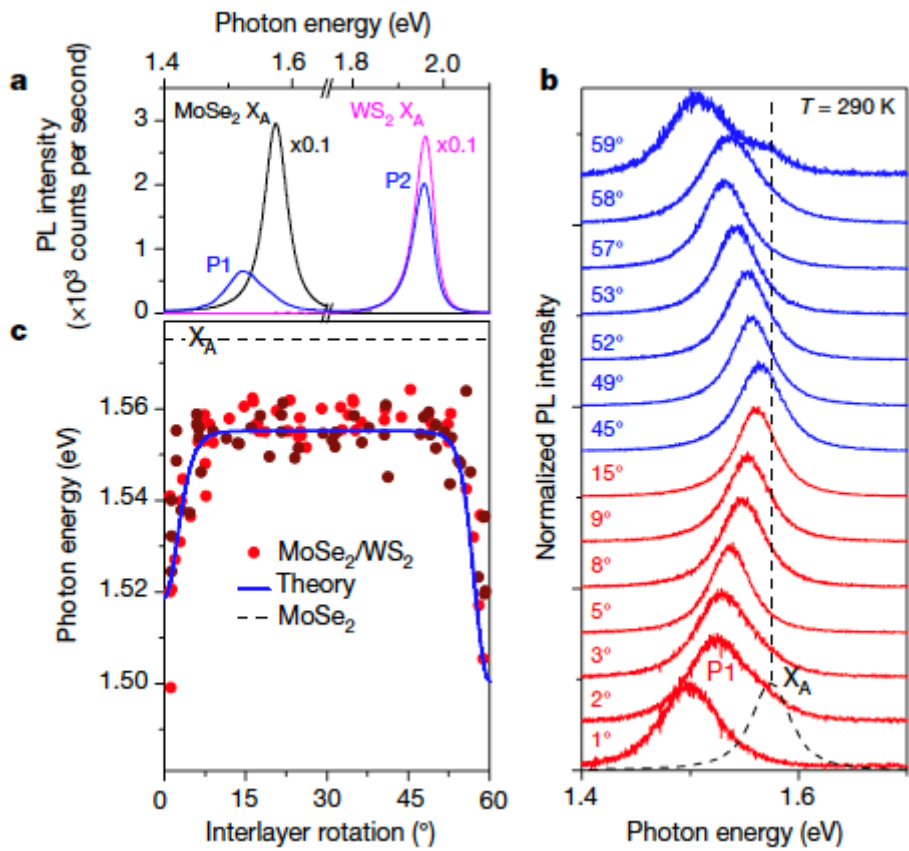


Figure 5.9: PL spectra of heterostructure. Adopted from [91]

# Chapter 6

## Polymorphism in group VI transition metals dichalcogenides; a specific case of 1T' and 2H phases of $WSe_2$

### 6.1 Introduction

In contrast to other 2D materials like hBN or graphene, TMDCs exhibit structural polymorphism and as such open an additional avenue in 2D material engineering. The relation between different phases observed in TMDCs can be seen in Figure 5.1. On top of altering the electronic nature of the TMDC, semiconducting or metallic, there can also be observed a variety of superconducting states [92][93], quantum spin Hall insulators [94][95][96][97] or Weyl semimetals [98]. Interestingly the various TMDC phases can coexist at specific temperatures and pressures [99][100][101]. Those different phases can exhibit small difference in energy per formula unit  $MX_2$ . As such a phase transition can be induced via e.g. a charge injection [102]. Overall the various phases of the TMDCs and the transitions between are of great interest and remain unexplored in full detail.

### 6.2 $WSe_2$ phases

The monolayers of TMDCs can be usually found in either 1H or 1T phase where the exact configuration depends on the thermodynamics [100][101]. In order to identify which of those phases is more favourable the crystal field theory can be applied. The number of electrons in d orbitals of transition metals needs to be counted for a given TMDC

material. For group IV TMDCs (Ti, Zr and Hf) that number is 0 ( $d^0$ ) while for group 10 (Ni, Pd and Pt) the number is 10 ( $d^6$ ). It can be therefore shown that the number of electrons in d orbitals correlates with the phase transitions in TMDCs as seen in Figure 5.2. The group IV TMDCs ( $d^0$ ) for instance are most stable in 1T phase. However the  $d_{z^2}$  level of the 1H phase has the lowest energy and therefore the TMDCs of group V ( $d_1$ ) and group VI ( $d_2$ ) fill that level first and therefore, they group V TMDCs are found most stable in either 1T or 1H phase while the group VI TMDCs are most favourable in 1H. After filling the  $d_{z^2}$  level in group VI TMDCs, the additional electron in group VII TMDCs contribute to the 1T levels and results in a distorted octahedral coordination (1T') with clusterisation or Peierls distortions of the metal atoms. Furthermore the group 9 and 10 TMDCs are most stable in the regular octahedral coordination (1T).

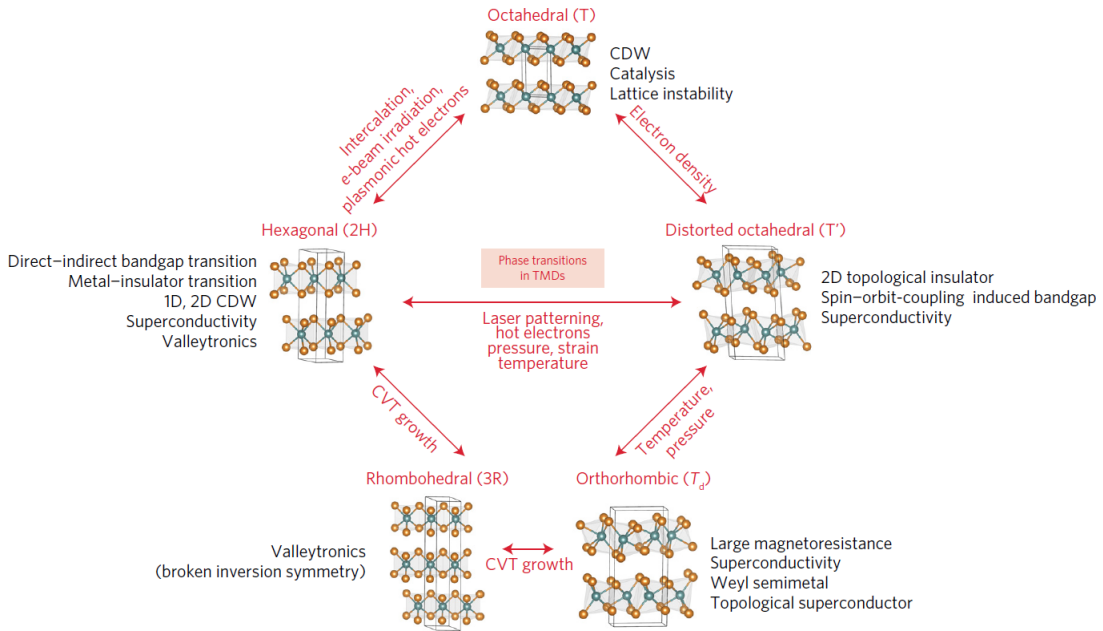


Figure 6.1: Transition and correlation between phase and physics in TMDCs. Reproduced from [103]

Recently the 1T' phase has received attention due to the predictions of potential Weyl semimetal or quantum spin Hall effects for group VI TMDCs [94][98]. Additionally the lattice distortion orientation can be affected by strain which allows for mechanical control of ferroelasticity and potential application as a shape memory material [104]. In order to achieve those effects in group VI TMDCs a phase transition from 1H to 1T' generally has to occur [105]. Such transition is usually performed via the lithium intercalation or chemical exfoliation. Following the lithiation the excess of the electrons is found in the d orbitals of the transition metals. As a result of that the electron density of those orbitals

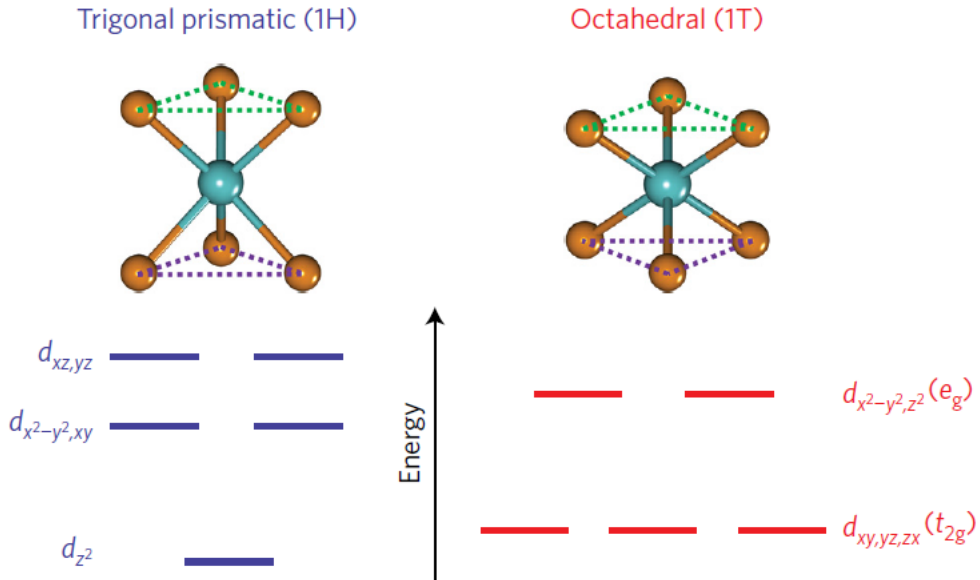


Figure 6.2: Diagrams of 1H and 1T lattices and energy levels of d-orbital electrons. Reproduced from [103].

increases from  $d_2$  to  $d_{2+x}$ . In order for a full transition from 1H to 1T to occur the excess of the electrons must be in range of 0.2 to 0.4. However if the excess is smaller than that then the distortion of the lattice may help to accommodate the phase transition.

One of the most important characteristics of TMDCs that influences a myriad of different properties is the number of layers. Especially in case of optical and electronic properties of 2H TMDCs the number of layers strongly affects the size and the nature of the bandgap, transitioning from indirect in bulk to direct in monolayer. The number of layers is however also of crucial importance to quantum effects observed or predicted in TMDCs in that the bulk material exhibits the in-plane inversion symmetry while the monolayers break it [92][93]. Such breaking of symmetry leads to strong spin-orbit coupling as well as effective Zeeman fields in TMDCS. Additionally an out of plane spin polarisation which depends on the valley, K or -K point, has been observed when a strong anisotropic magnetic field has been applied to quench the superconductivity in 2H-*MoS*<sub>2</sub>. There has also been observed a superconducting state in monoclinic and 1T' *MoTe*<sub>2</sub>, and where also the Weyl semimetal and topological insulator states are expected [94][98][106].

Due to the distortion in the 1T' phase of the group VI TMDCs a band inversion near the Fermi level with p and d bands from chalcogenides and metal atoms respectively. These bands result in some interesting phenomena, the Weyl state and quantum spin Hall effect. Those effects can manifest themselves in distorted octahedral phase (1T')

or orthorhombic ( $T_d$ ) phase. It has been shown using DFT calculations that group VI TMDC in the T' phase exhibit the band inversion resulting in the quantum spin Hall effect [94][95]. The change in number of layers results not only in inversion symmetry breaking but also affects the bandgap magnitude and as such is crucial in achieving the dissipationless spin transfer by the QSH [107][108]. It has theorised that a topological FET can be realised through the application of the external electric field which can turn the topological states on or off.

In contrast to the 1T' phases of group VI TMDCs, the orthorhombic  $T_d$  phase shows Weyl semimetallic states as a result of the inversion symmetry breaking. The  $T_d$  phase can be achieved via control of the defects, cooling down the T' phase below 240K or as a result of high pressure [106].

A phase transition from 2H to 1T in  $MoS_2$  has been observed using the TEM. Several intermediate phases have been identified and the gliding planes of Mo and S atoms have been observed. It has also been shown that the electron injection in TEM can be used to pattern the phase transition, and therefore that the electron driven phase transition is possible [109]. Additionally it has been shown that local heating and the chalcogenide defects created as a result can induce an irreversible transition from hexagonal to monoclinic phase in  $MoTe_2$  [101]. A laser irradiation can also cause a phase transition in  $MoS_2$  from monoclinic to hexagonal, where the activation energy for the transition has been found to be  $\sim 400$  meV [110]. There has also been demonstrated transition from hexagonal to monoclinic  $MoS_2$  using plasmonic hot electrons [111]. The injected hot electrons in the 4d band of the Mo atoms result in a more stable monoclinic phase according to the crystal field theory. As one of the potential application an infrared sensor can be proposed where a phase transition is engineered by strain to occur at such low temperature that a small change in temperature can induce it [112].

A contact between the 2D TMDC layer and rest of the device is of critical importance for any electronic and energy application. The commonly used transfer method of assembling the material with the contacts is generally undesirable as it alters the structure of the TMDC material. To this effect the homojunction offers a viable alternative as it has been presented with local transition from 2H  $MoS_2$  to 1T  $MoS_2$  [99]. The resulting 1T metallic phase interface as seen in Figure 5.3 with the metal contacts reduces the contact resistance in  $MoS_2$  FET.

One of the approaches to synthesis of TMDCs and which has been applied to growth of  $WSe_2$  is colloidal synthesis. This wet synthesis method involves dissolution of precursors

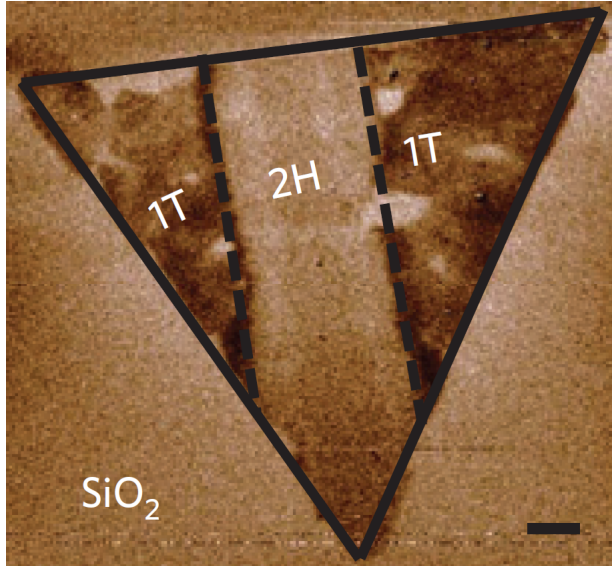


Figure 6.3: Electrostatic force microscopy phase image of a monolayered  $MoS_2$  homojunction. Reproduced from [99]

in solution, careful control of time and temperature of reaction and subsequent deposition of dispersed flakes onto a substrate. Using that method small 2H  $WSe_2$  and  $MoSe_2$  flakes were successfully produced [113][114]. There have been however no successful growths of 1T' TMDCs using this methods.

### 6.3 Conclusions

In this chapter we have summarized the fundamental differences between 2H and 1T/1T' phases of TMDCs with emphasis on the different crystalline phases and electronic properties along with different phenomena that can be enabled by the 1T' phases. Additionally, we have laid out a short summary of the synthesis methods for the metastable 1T/1T' phases.

# Chapter 7

## Chemical vapour deposition of mono-few-layered $WS_2$ : the role of precursors

In this chapter the CVD growth of  $WS_2$  using different precursors is investigated. The as grown samples were characterised by Raman and PL spectroscopy as well as XPS, XRD, AFM and electrical measurements. As a result it was concluded that using  $H_2WO_4 + NaCl$  at 850 °C gives best results. Such grown samples exhibit biggest flakes up to 200  $\mu m$  in size as well as show the strongest and most narrow PL peak with 36 meV FWHM. The samples grown using  $H_2WO_4 + NaCl$  at 950 °C show also best transistor electron mobility in monolayer CVD grown  $WS_2$  while that grown using  $WO_3 + NaCl$  at 950 °C shows best transistor electron mobility in bilayer CVD grown  $WS_2$ .

### 7.1 Introduction

Monolayers of transition metal sulphides and selenides exhibit range of interesting properties such as strong light absorption in the IR and visible range [22][5][115], valley polarisation [116] [117], spin-orbit interactions [118][54], tightly bound excitons [11] or second-harmonic generation [119]. Some of these effects can be attributed to the lack of free dangling bonds and configuration of d-orbitals [120], [121].

Among these materials one of the most promising is the  $WS_2$ . Its visible range optical bandgap of 2 eV as well as an easy and safe manufacturing route via CVD makes it one of the more interesting and studied TMDCs. The typical characterisation by pho-

toluminescence spectroscopy allows to probe the varying synthesis conditions, the grain boundaries or defect population [4] [53] [76] [65]. The PL efficiency in as-grown monolayer  $WS_2$  produced via CVD growth shows  $\sim$ 2-6% efficiency [53][122] [123]. This efficiency is caused mostly by defect-mediated non-radiative recombination centres [124]. LEDs have been successfully produced [125] showing external quantum efficiency up to 10% [126][33].  $WS_2$  is typically a n-type semiconductor due to the presence of sulphur vacancies [4][17][52]. In order to utilise this material in any potential future applications a reliable and scalable manufacturing method must be developed to ensure a high quality crystal on the wafer scale area. The main method for  $WS_2$  synthesis that satisfies these conditions is Chemical Vapour Deposition (CVD) [127]. The growth of tungsten based TMDCs have been less successful than the equivalent molybdenum based TMDCs and has produced mostly isolated flakes of up to  $40\ \mu m$  [4] [75] [65] [63][128][129][77]. Even larger films of monolayer  $WS_2$  have been shown, however they also exhibit low carrier mobility [130][131]. In the typical CVD synthesis process the sulphur and tungsten oxide are evaporated simultaneously in a tubular furnace with a constant flow of carrier gas like argon at temperatures of at least  $900\ ^\circ C$  [4][75][65][63][128][129][77]. Such growth is predicated by topotactic transformation leading to low density distribution of domains on an amorphous [4][75][63][129][77] or crystalline substrate [65][128][78] possibly due to low evaporation rates of  $WO_3$ . Since  $WO_3$  requires high temperatures of  $950$ - $1000\ ^\circ C$  to evaporate while the  $S$  becomes volatile at  $90\ ^\circ C$  the thermodynamics of the process are difficult to control. The low growth dictated by fast evaporation of  $S$  leads to limited domain growth and lack of continuous layer. One of the proposed solutions have been to spread the  $WO_3$  on the target substrate [53][76][131][64][132][133][85]. This has however led to low reproducibility, poor control of thickness and stoichiometry and unreacted material left on the substrate. Another approach has been to use more volatile  $W$  precursors such as  $WCl_6$ [134] or  $W(CO)_6$ [130][135] together with organic compounds as  $S$  precursors. Such method while producing a large area domains at lower temperature has led to lower crystal quality and purity.

Here we propose a different method of CVD synthesis that allows for much larger flake growth of up to  $800\ \mu m$  at temperature of  $750\ ^\circ C$ . Such grown material exhibits high electron mobility in one and two layers of  $WS_2$ , higher than other values reported in literature. The photoluminescence peak is also very narrow at  $36\ meV$  FWHM at room temperature.

## 7.2 Results

For the purpose of comparing the CVD synthesis method conditions the several sets of precursors were used:  $WO_3$ ,  $WO_3 + NaCl$  and  $H_2WO_4 + NaCl$ . The standard growth procedure involves two separate crucibles placed at distance from each other in a quartz tube. Each of these crucibles is independently heated to ensure that the S and the W precursors evaporation rate is maximised at the same time. The vapours then are deposited on  $SiO_2/Si$  (285 nm) substrate which is placed close to the W precursor crucible. The entire process is performed under low vacuum and a supply of Ar gas. The furnace setup can be seen in Figure 6.1.

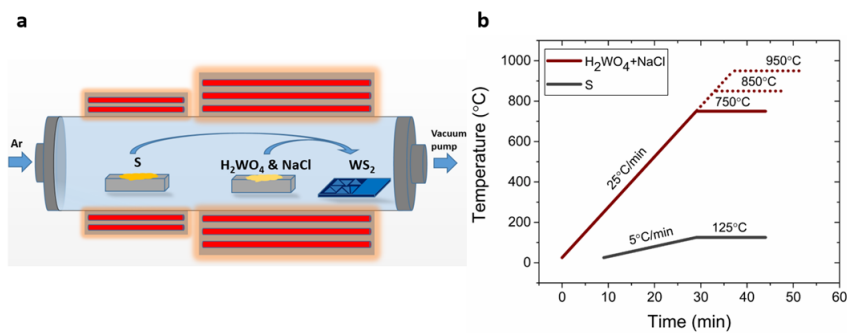


Figure 7.1: a) CVD furnace setup; b) Temperature profiles for the W and S precursors.  
Adopted from [136]

By following this method a reproducible deposition of large area flakes can be shown. As seen in Figure 6.2 the size of the flakes increases from left to right as the precursors used ( $WO_3$ ,  $WO_3 - NaCl$  and  $H_2WO_4 - NaCl$ ) change as well as demonstrating the lower temperature required to achieve these growths. All of these growths result in formation of triangular flakes with sharp edges and uniformity of colour throughout which suggest a high quality, pristine material across the flake. The growth using only  $WO_3$  results in formation of small flakes of 10  $\mu m$  at 950 °C while no growth occurs at lower temperatures (Figure 6.2). This can be explained by the high sublimation temperature of  $WO_3$ .

The growth can also be observed using  $WO_3 + NaCl$  at 950 °C and 850 °C with the former showing flakes of size of about 60  $\mu m$  while the latter showing smaller flakes of about 30  $\mu m$  in size. To explain this difference in size a Robinson & Robin model can be used which states that at higher temperatures the diffusivity of the adsorbed precursors is favourable to the expansion of the existing domains [137]. On the other hand the desorption of the adsorbed species is high which limits the supersaturation and formation

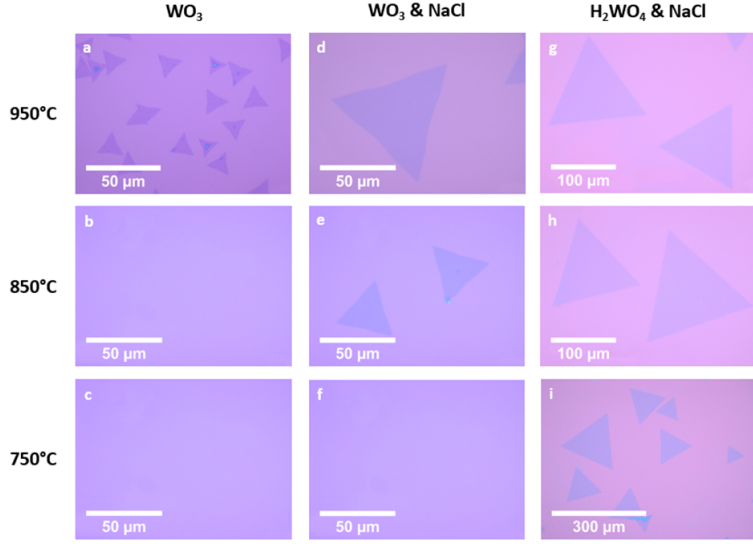
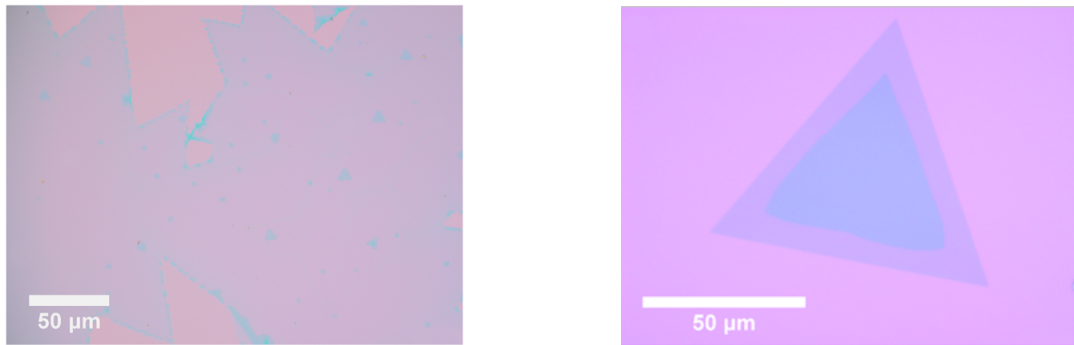


Figure 7.2: OM image of  $WS_2$ . Adopted from [136].

of new domains. If the temperature is lowered even further to 750 °C then no growth is observed at all, most likely due to slow evaporation of  $WO_3$  precursor.

With the change of precursors from  $WO_3$  to  $H_2WO_4$  a significant change in size of flakes is observed at 850 °C and higher temperatures with lengths exceeding 200  $\mu m$ . Additionally the growth has been shown to occur at 750 °C with flakes of the size of 50-200  $\mu m$ . Moreover continuous monolayer areas of up to 0.8 mm in size has been shown (Figure 6.3a). By increasing the growth pressure (1.6 mbar to 13 mbar) at 950 °C bilayer  $WS_2$  flakes can be preferentially formed (Figure 6.3b).



(a) Continuous layer of  $WS_2$ .

(b)  $WS_2$  bilayer.

Figure 7.3: OM Images of  $WS_2$ . Adopted from [136].

To understand the facilitated synthesis of  $WS_2$  using  $H_2WO_4$  and  $NaCl$ , we conducted X-ray diffraction (XRD) analysis of the reaction products between  $H_2WO_4 + NaCl$  and  $WO_3 + NaCl$  systems at different temperatures (500 °C, 650 °C and 750 °C) to under-

stand the chemical differences (Figure 6.4). We found that the main products of the reactions between  $NaCl$  and  $H_2WO_4$  are:  $Na_xW_yO_z$  and tungsten oxychloride ( $WClO_4$  and  $WO_2Cl_2$ ). The  $Na_xW_yO_z$  possesses a high evaporation temperature as it remains in the crucible (Figure 6.5) after the synthesis of  $WS_2$  is completed. Further, using this compound as precursors for a new growth of  $WS_2$  at 950 °C did not lead to the formation of any  $WS_2$  flakes, confirming the high evaporation temperature. On the bases of previous studies on the synthesis of bulk crystals, the formation of tungsten oxychloride species ( $WO_2Cl_2$  and/or  $WOCl_4$ ) is likely to occur while the formation of metal halides is less favourable (e.g.  $WCl_6$ ) [138][139]. Tungsten oxychlorides are volatile already at 200 °C [140] and they can be sulfidised in vapour phase and then be deposited onto the target substrate as atomic clusters. There has been successful growths of bulk  $WS_2$  using  $WOCl_4$  as a precursor [134]. Owing to clean decomposition pathways  $WOCl_4$  has proven to be an effective precursor avoiding the formation of tungsten oxysulfide. We have shown that growth of  $WS_2$  is possible at low temperatures of 550 °C using this precursor. When the growth is attempted using only tungsten as sole precursor the role of the oxyhalide species becomes highlighted. In such a growth only small  $WS_2$  flakes are observed with PL performance similar to that of the pure  $WO_3$  precursor growth. By replacing the  $NaCl$  by similar precursor,  $KCl$ , we further confirmed the key role of Cl in this growth.

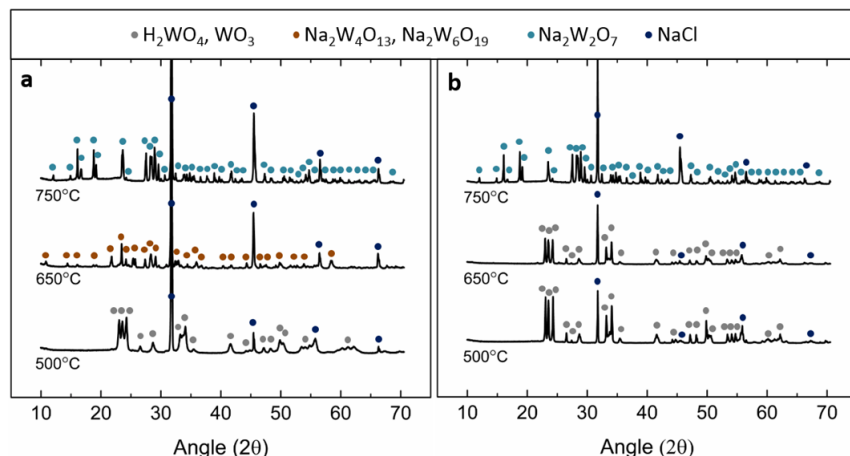


Figure 7.4: XRD spectra of residuals after annealing, a)  $H_2WO_4 + NaCl$  b)  $WO_3 + NaCl$ . Adopted from [136].

The flakes were investigated using HRTEM to confirm high crystallinity of the material (Figure 6.6). The lattice constant measured in this way has been found to be 0.3 nm, which is consistent with that of 2H-WS<sub>2</sub> (0.318 nm). The AFM characterisation allowed to confirm the presence of monolayer (Figure 6.6) and bilayer (Figure 6.3b) flakes with

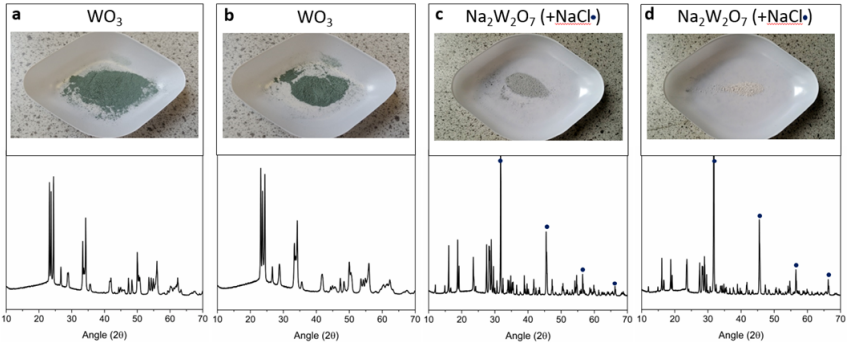


Figure 7.5: Images of residuals of the tungsten precursors after annealing at 750°C. The blue show possible NaCl. Adopted from [136].

the step of 0.8 nm [141][142].

The Raman spectroscopy characterisation of  $WS_2$  flakes obtained under different growth conditions can be seen in Figure 6.6. All of these spectra exhibit the main 2 peaks at  $\sim(351\pm0.53) \text{ cm}^{-1}$  and  $\sim(417.6\pm1) \text{ cm}^{-1}$ . The latter peak corresponds to the  $A_{1g}$  vibrational mode while the former peak can be further resolved into two peaks, one related to 2LA vibrational mode and the second to  $E_{2g}^1$ . As seen in the Figure 6.9a and Figure 6.9c the distribution of intensity of both main peaks is uniform across the flakes. Similarly the difference between peak positions of  $A_{1g}$  and  $E_{2g}^1$  is also uniformly distributed as seen in Figure 6.10 and is equal to  $\sim(66.5\pm0.53) \text{ cm}^{-1}$  which is indicative of monolayer [143].

As seen in Figure 6.7 maps of PL intensity has been collected for samples grown using different growth condition. The sample grown using  $WO_3$  at 950 °C appears to be trisected into 3 symmetrical areas. The intensity is lowest along the the trisecting lines and highest in the centre of each of the sub-triangles. The PL peak position is inversely proportional to the intensity of the PL peak as seen in Figure 6.11a. The distribution of the PL peak positions seems to be bimodal with maxima at 1.96 eV and 1.94 eV. The FWHM is distributed mostly uniformly with few small areas of greater and few of smaller FWHM (Figure 6.11b with the average value of 65 meV. These peak position and FWHM values are comparable with those reported in literature [4][65][144][145]. The PL spectra taken from one of the three smaller parts of the flake are redshifted by about 0.02 eV and are wider than average. This can be explained by the presence of defects, in particular sulfur vacancies, which effectively cause the  $WS_2$  to be n-doped [146][147]. This in turn increases the trion population which introduces new peak, redshifted by about 30 meV, which results in overall shift and broadening of the PL peak [148][4]. Additionally such

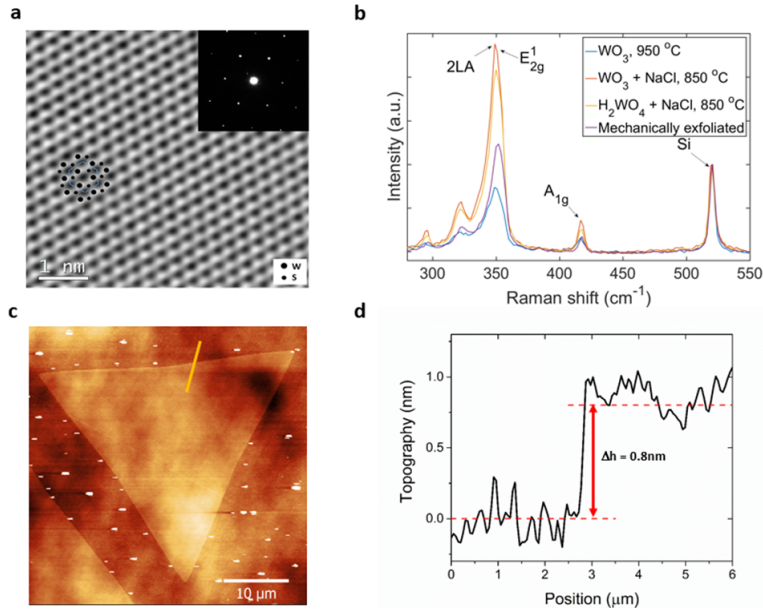


Figure 7.6: a) HRTEM image of  $WS_2$  grown with  $H_2WO_4 + NaCl$ , inset shows a hexagonal diffraction pattern. b) Raman spectra taken from  $WS_2$  grown various precursors with characteristic peaks indicated. c) AFM image d) height profile of single layer  $WS_2$ . Adopted from [136].

localised changes in PL peak intensity and position can be caused by local strain [149][146]. To investigate the potential effect of strain on the observed PL pattern a flake was cut using high power 532nm laser. As seen in Figure 6.12 the resulting pattern remains the same as before treatment. Therefore the observed pattern is most likely caused by the local variation in defect density [150].

By introducing the NaCl and mixing it with  $WO_3$  precursor  $WS_2$  samples are grown that exhibit higher energy and narrower PL peaks. The spectra are asymmetric and can be therefore deconvoluted to obtain an exciton and trion component (Figure 6.8). The spatial distribution of the PL position and width is mostly uniform throughout the flake. However the distribution of PL peak positions and FWHM across different flakes grown at the same conditions is bimodal (Figure 6.8. The PL peak position is found to be ( $\sim 1.95 \pm 0.002$  eV and  $1.96 \pm 0.002$  eV) while the FWHM is ( $\sim 43 \pm 2.8$  meV and  $51 \pm 3$  meV) which is smaller than most reported works [4][65][144][145]. This can be explained by smaller trion component in the PL spectrum which in turn means that  $WS_2$  samples grown at these conditions contain less structural defects compared to the pure  $WO_3$  growth. A difference in growth mechanism (topotactic or molecular conversion) which results in different defect distribution can be attributed to the differences in samples.

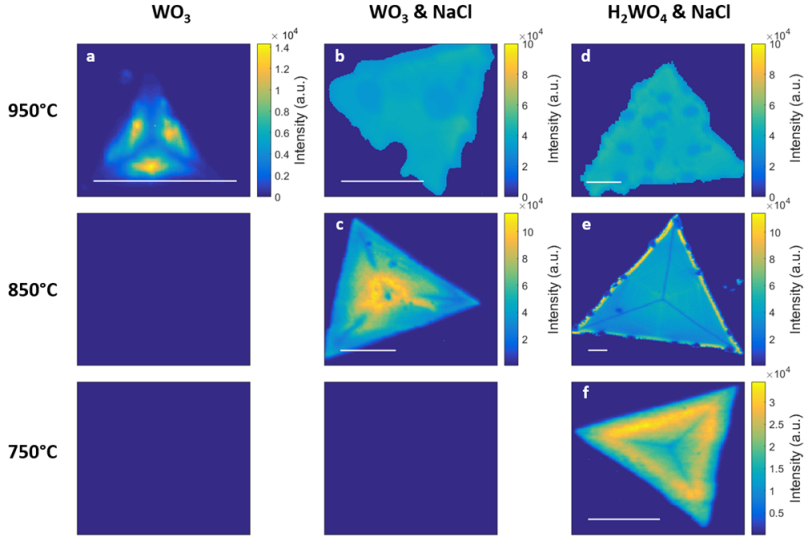


Figure 7.7: Maps of  $WS_2$  PL intensity. The scale bar is  $10\mu\text{m}$ . Adopted from [136].

By changing the  $WO_3$  precursor to the  $H_2WO_4$  precursor a further shift in PL peak position, as well as increase in PL intensity and narrowing of the PL peak is observed as seen in Figure 6.7, Figure 6.8. The PL peak position distribution across the flake is narrow and is ( $\sim 1.980 \pm 0.005$  eV) which is higher than that of the  $WO_3$  and  $WO_3 + NaCl$  systems. The FWHM is found to be ( $\sim 36 \pm 3$  meV) which is also smaller than that of the  $WO_3$  and  $WO_3 + NaCl$  systems. The PL peak width is also smaller than that reported in literature for CVD grown [4][65][144][145] exfoliated  $WS_2$  [115][17]. At the same time it is comparable to the  $WS_2$  grown on van der Waals substrates [78] as well as mechanically exfoliated  $WS_2$  [125]. Additionally the peak position as well as FWHM variation is also smaller than that of other samples (5meV and 3 meV respectively) (Figure 6.13d). The PL peak intensity map (Figure 6.7) shows that the spatial distribution of intensity is also much more homogeneous with faint weak pattern of three trisecting lines still visible.

As seen in Figure 6.9 the Raman peaks are generally uniform in both intensity and position for most samples. The irregularities in the intensity and position of both the  $E_{2g}^1$  and  $A_{1g}$  in the sample grown at 950 °C with both  $WO_3 + NaCl$  and  $H_2WO_4 + NaCl$  are caused primarily by residue deposited on top of the flakes after the growth as seen in optical micrographs. Additionally as seen in Figure 6.9a the deviations from the mean value are located primarily at the edges of the sample. This suggests that the rest of the flake is pristine and the deviations are associated with residue located at the edges. The coefficient of variation (CV) for the intensity and position for the samples grown at 950 °C with  $WO_3$  and at 850 °C with  $WO_3 + NaCl$  and  $H_2WO_4 + NaCl$  is on the order of up

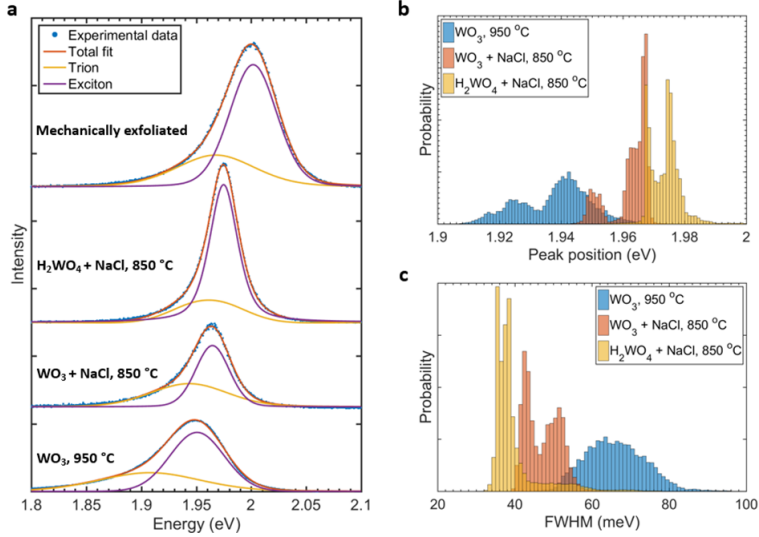


Figure 7.8: a)  $WS_2$  PL spectra grown using various precursors b) histograms of PL peak positions c) histograms of PL peak widths. Adopted from [136].

to  $10^{-4}$  which indicates a very high homogeneity across the samples. This further shows that the crystal quality of the flakes is quite uniform regardless of the growth method.

By looking at the difference in position between  $A_{1g}$  and  $E_{2g}^1$  peak positions as seen in Figure 6.10 it can be further concluded that the flakes are uniformly monolayer. The deviations from the mean are heavily localised and correlated with differences in PL as well as optical images and are most likely caused by precursors residue. Additionally no trisecting lines (as seen in Figure 6.7) can be seen in the maps of Raman spectra.

The maps of PL peak positions and widths can be seen in Figure 6.11. The PL positions map of the sample grown at 950 °C using  $WO_3$  shows some variability with spots of lower energy that loosely correlate with the PL intensity. There is still faintly visible pattern of three trisecting lines of higher energy as seen in Figure 6.7. This indicates the areas with higher intensity correlate with lower peak position, especially along the trisecting lines. The other maps, especially the ones grown at 850 °C and 750 °C with  $WO_3 + NaCl$  and  $H_2WO_4 + NaCl$ , are more uniform in terms of PL peak position and PL peak width. The deviations are again highly localised and correlated with the deviations in Raman and PL intensity. These deviations are generally of lower PL peak position as well as greater PL peak width which generally indicates lower crystal quality.

One possible explanation of the pattern of trisecting lines as seen in e.g. Figure 6.7 is the thermal strain caused by difference in thermal expansion coefficient between  $WS_2$  and the  $SiO_2$  substrate. Since it is known that the strain in TMDCs including  $WS_2$  can cause

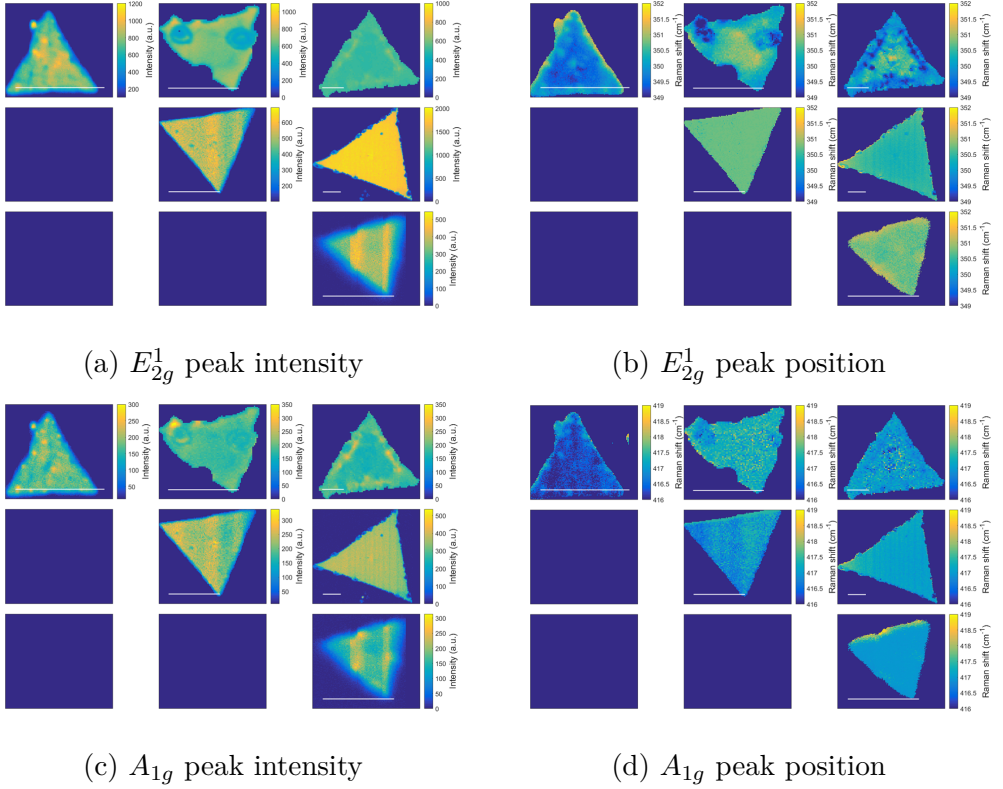


Figure 7.9: Raman peaks maps. Adopted from [136].

the change in Raman and PL spectrum [149][146] then removing a piece of the material should cause the strain to adapt to new bounding conditions. In order to investigate the trisecting pattern a flake with such pattern has been cut using 532 nm high intensity laser (50 mW). As seen in Figure 6.12 both the PL intensity maps and Raman  $E_{2g}^1$  maps show a clear separation. The resulting PL and Raman intensity maps however do not show any significant change in the pattern. The trisecting lines as well as local maxima can still be seen in PL intensity map. The Raman shows few spots of increased intensity on one of the halves of the flake as well as a very weak increased intensity area along the cut. Since there is no observed increased intensity along any edges before cutting the flake it does not appear that the increased intensity along the cut is a result of strain being resolved into new bounding conditions. It appears therefore that cutting the material did not alter the pattern nor alter the rest of the PL or Raman spectra maps.

The spectral maps from different flakes grown with the same conditions were then collected and plotted as graphs of intensity or width versus position. As seen in Figure 6.13d the PL intensity seems to be largely independent of the PL position. If PL is present at given position then intensity is mostly uniformly distributed in terms of intensity. The PL width seems to be inversely related with regards to PL position. In samples grown at

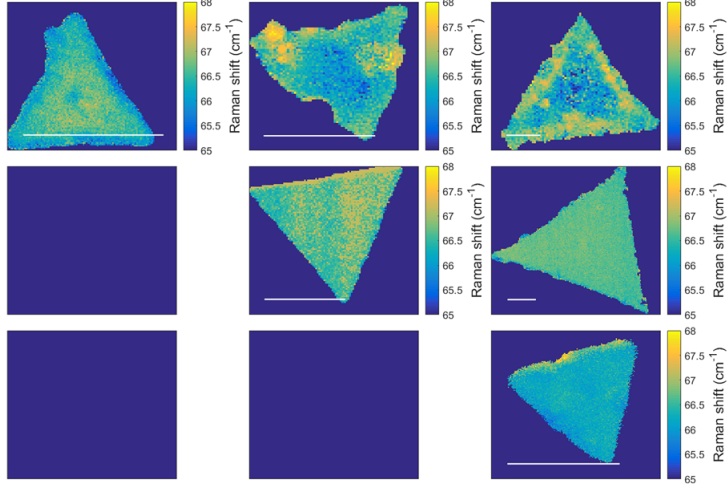


Figure 7.10: Raman peaks  $2LA$ ,  $A_{1g}$  positions difference. Scale bar is  $10 \mu\text{m}$ . Adopted from [136].

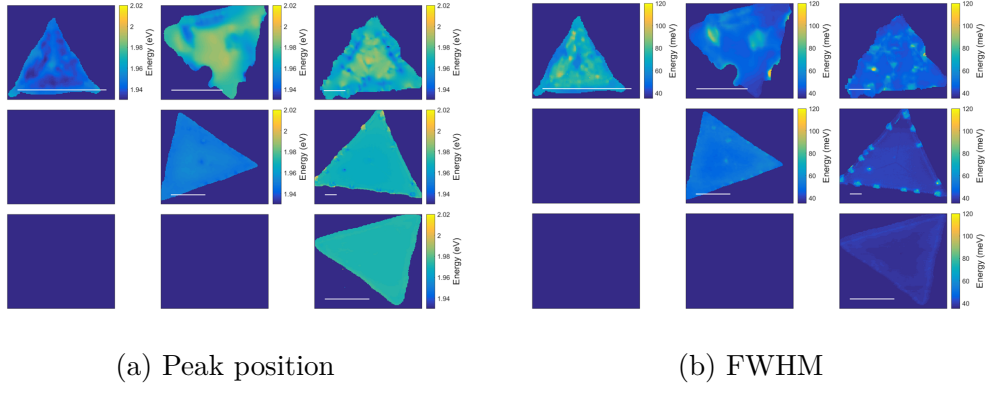


Figure 7.11: PL peak positions and FWHM maps. Adopted from [136].

$850^\circ\text{C}$  with  $WO_3 + NaCl$  the relation seems to be the strongest. Across all the samples the values vary between around 60-80 meV at low PL energies (1.92 eV) to 40-60 meV at high PL energies (1.98 eV). This seems to be related to overall quality of the crystals, i.e. the presence of defects, stoichiometry, crystallinity, doping, adatoms. The more uniform the sample the less mechanisms for peak broadening as well as fewer added energy levels facilitating different electron recombination paths.

The chemical composition of the flakes grown using  $H_2WO_4 + NaCl$  has been investigated using XPS. The W 4f $5/2$  and W 4f $7/2$  core levels show peak positions that of the  $W^{4+}$  in  $WS_2$  [151][152] (32.7 eV 34.8 eV respectively) with FWHM of 1 eV (Figure 6.14, the smallest possible using Mg K $\alpha$  x-ray source. It means therefore that the  $WS_2$  is of perfect stoichiometric ratio of W and S. Additionally by integrating the intensity of the

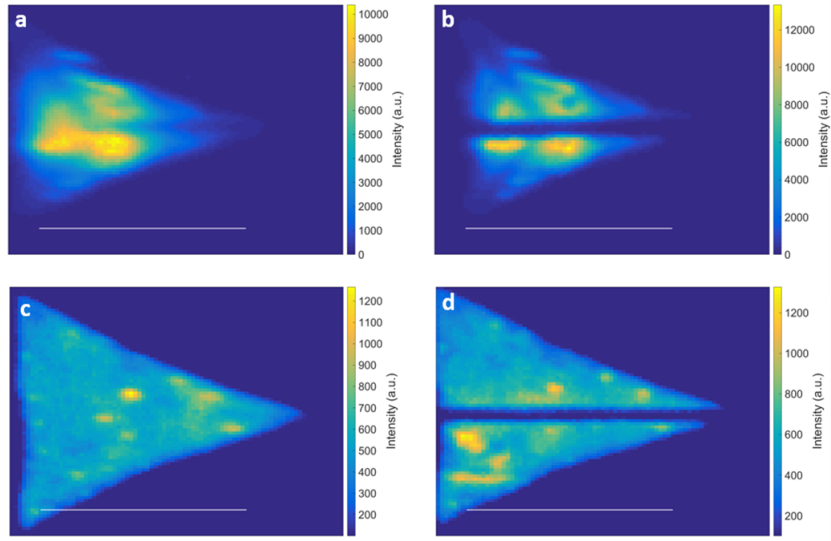
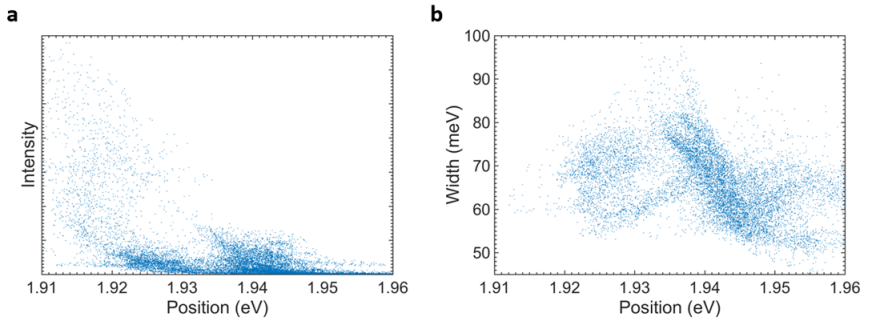


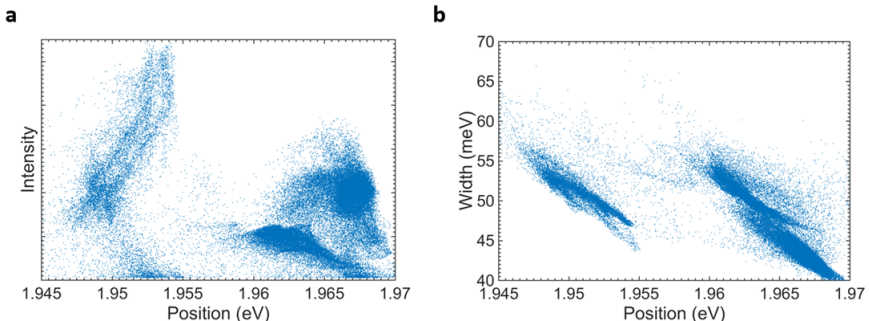
Figure 7.12: Maps of PL intensity a) before b) after performing the cut. Maps of  $2LA+E_{2g}^1$  Raman peak intensity c) before d) after performing the cut. Scale bar is  $10 \mu\text{m}$ . Adopted from [136].

$\text{W } 4\text{f}$  and  $\text{S } 2\text{p}$  core level peaks the same result is achieved. Furthermore the  $\text{S } 2\text{p}\frac{1}{2}$  and  $2\text{p}\frac{3}{2}$  core levels are also present at the expected position for  $WS_2$  (162.3 eV and 163.4 eV respectively, Figure 6.14) and small FWHM of 1 eV [152]. Small peaks indicative of  $W^{6+}$  ( $\text{W } 4\text{f}\frac{5}{2}$  and  $\text{W } 4\text{f}\frac{7}{2}$  at 35.9 eV and 38.1 eV respectively, Figure 6.14) can be attributed to presence of  $WO_3$  and which partially overlaps with  $\text{W } 5\text{p}$  core level (38.5 eV). These peaks however disappear after the flakes are transferred to another  $Si/SiO_2$  substrate, suggesting that they can be caused by residue  $WO_3$  given that the XPS spot size is relatively big ( $\sim 1 \text{ mm}$ ). The FWHM of the  $\text{W } 4\text{f}$  core levels was unchanged after the transfer, indicating that the crystallinity and the quality of the flakes was preserved with no extra defects introduced.

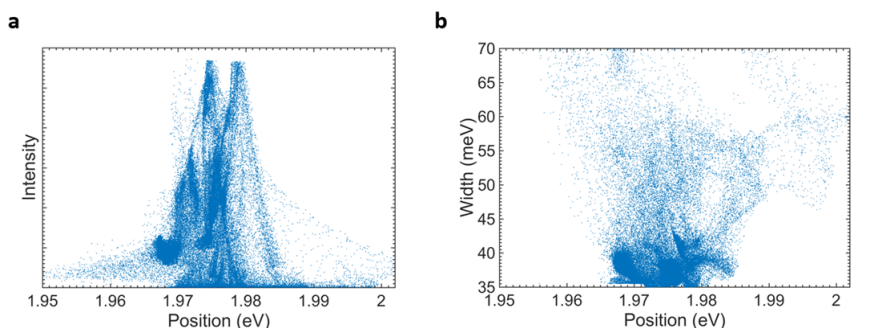
The  $WS_2$  samples grown using  $WO_3 + NaCl$  have been characterised by XPS as well and the stoichiometric ratio of 2:1 for S:W has been found. However the  $W^{6+}$  component, caused most likely by presence of  $WO_3$  ( $\text{W } 4\text{f}\frac{5}{2}$  and  $\text{W } 4\text{f}\frac{7}{2}$  at 35.9 eV and 38.1 eV respectively) is more pronounced indicating incomplete sulfurisation. Similarly to the sample grown with  $H_2WO_4 + NaCl$  this component disappears entirely upon transferring the sample onto new  $Si/SiO_2$  indicating it is present around the flakes, distributed across the substrate. The  $W^{4+}$   $4\text{f}$  core levels peak width is  $\sim 1.2 \text{ eV}$  which indicates higher defect concentration compared to that of the sample grown using  $H_2WO_4 + NaCl$ . This FWHM however increases after the transfer, which is most likely caused by the increase



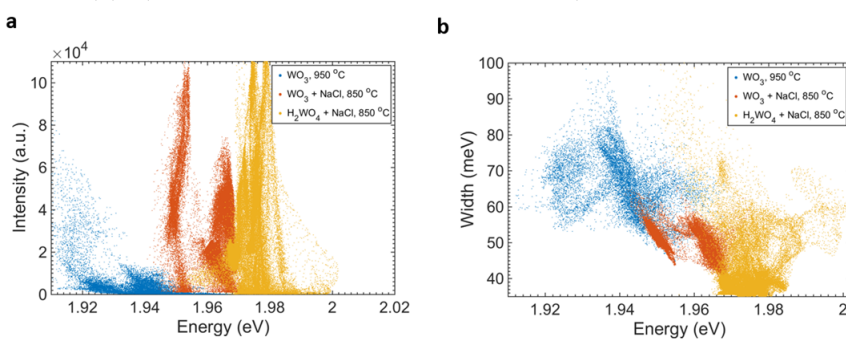
(a) a) PL peak intensity vs position, b) PL FWHM vs position



(b) a) PL peak intensity vs position, b) PL FWHM vs position



(c) a) PL peak intensity vs position, b) PL FWHM vs position



(d) a) PL peak intensity vs position, b) PL FWHM vs position

Figure 7.13: a), b)  $WS_2$  grown using  $WO_3$  at  $950\text{ }^\circ C$ ; c), d)  $WS_2$  grown using  $WO_3 + NaCl$  at  $850\text{ }^\circ C$ ; e) f)  $WS_2$  grown using  $H_2WO_4 + NaCl$  at  $850\text{ }^\circ C$ ; g), h)  $WS_2$  grown using  $WO_3, WO_3 + NaCl, H_2WO_4 + NaCl$ . Adopted from [136].

in the concentration of the defects caused by the mechanical stress during the transfer. In conclusion the  $H_2WO_4$  is shown to be a better precursor compared to  $WO_3$ .

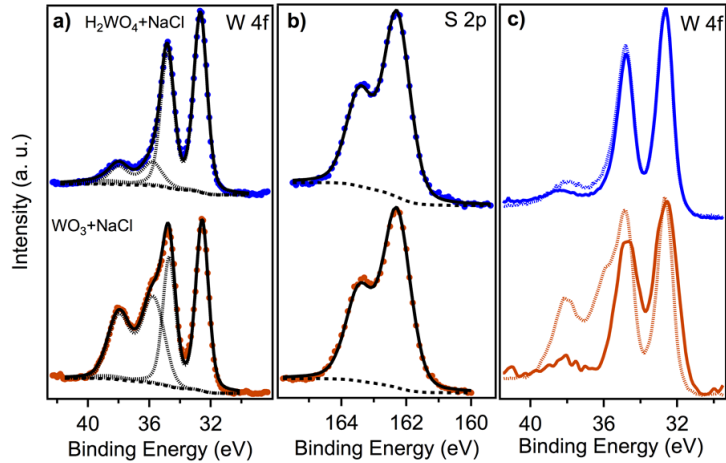


Figure 7.14: XPS spectra of the  $WS_2$  samples. a) W 4f $5/2$ , W 4f $7/2$ , W 5p core levels of sample grown with  $H_2WO_4 + NaCl/950\text{ }^\circ C$  (top), sample grown with  $WO_3 + NaCl/950\text{ }^\circ C$  (bottom). Black dashed line - deconvolution of the peaks, black continuous line - total fit. (b) S 2p $1/2$ , 2p $3/2$  core levels for corresponding samples. (c) W 4f $5/2$  , W 4f $7/2$ , W 5p core levels taken from samples before (dashed line) and after (solid line) transfer. Adopted from [136].

The samples were further characterised for their electrical properties. Bottom-gated field effect transistors were prepared as seen in Figure 6.15. The FET transfer curve indicates accumulation-type n-channel transistor, where the drain current increases with applied gate bias after a threshold is crossed. Once the current-bias curve reaches linear range it can be described by  $I_d = \mu_n C_{ox} (W/L)((V_{gs} - V_{th})V_{ds})$ , where  $\mu_n$  is the electron field-effect mobility,  $C_{ox}$  is the oxide dielectric and  $V_{th}$  is the threshold voltage. As seen in Figure 6.15 a typical response curve for both the as grown as well as transferred samples of  $WS_2$  grown with  $H_2WO_4$  show an asymmetry around  $V_{ds} = 0\text{ V}$  due to difference in the source and drain potentials. The Schottky barrier at the source is pinned by the gate, while the barrier at the drain diminishes proportionally to the drain bias and vice versa. The contacts however become more "Ohmic", when the bands bend more at the semiconductor/metal interface while the gate bias increase, leading to more significant tunnelling current.

By looking at the linear regime of the transport graph (red-dashed line in Figure 6.15) the field-effect mobility can be calculated as  $\mu_n = C_{ox}^{-1}(d\sigma/dV_{gs})$ . The electron

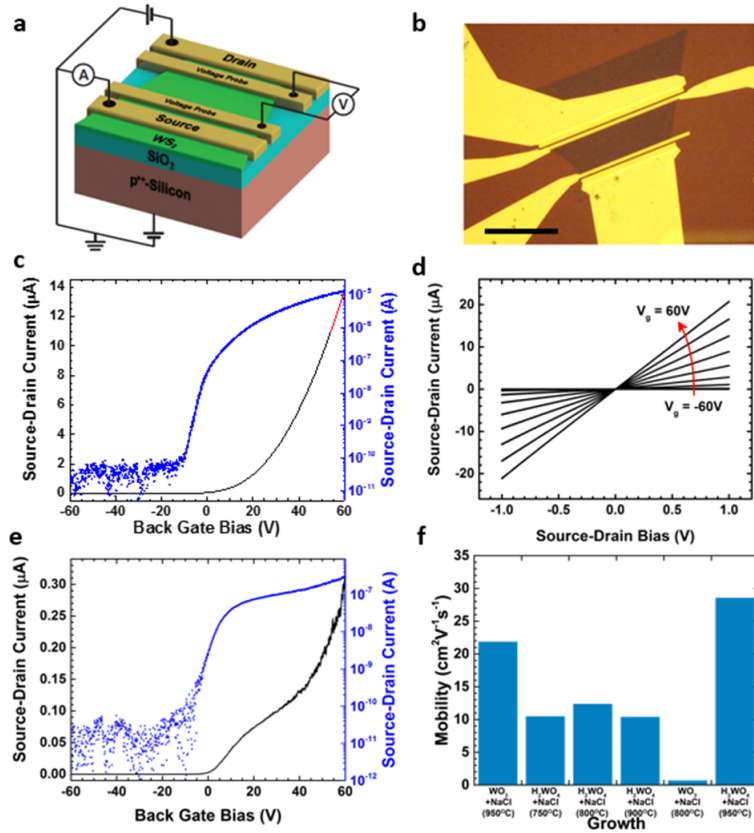


Figure 7.15: a) FET diagram; b) OM image of the FET (scale bar is  $20\mu\text{m}$ ); c) FET transfer curve taken from the single layer sample made with  $\text{H}_2\text{WO}_4 + \text{NaCl}/950\text{ }^\circ\text{C}$ ; d) I-V curves taken at different gate biases for sample made with  $\text{H}_2\text{WO}_4 + \text{NaCl}$ ; e) FET transfer curve taken for single layer sample made with  $\text{WO}_3 + \text{NaCl}/800\text{ }^\circ\text{C}$ ; f) comparison of electron mobilities of single layer  $\text{WS}_2$  made with different precursors.

Adopted from [136].

mobility calculated for  $\text{WS}_2$  grown with  $\text{H}_2\text{WO}_4 + \text{NaCl}$  is generally higher than that of  $\text{WS}_2$  grown with  $\text{WO}_3 + \text{NaCl}$  (Figure 6.15) which further indicates higher crystal quality when using  $\text{H}_2\text{WO}_4$ . The monolayer  $\text{WS}_2$  exhibits electron mobility of  $28\text{ }cm^2\text{V}^{-1}\text{s}^{-1}$ , the highest reported value for CVD grown  $\text{WS}_2$  and transferred onto  $\text{SiO}_2$  [76][130][131][75][128][77][132][153][154][155][156] and comparable to mechanically exfoliated  $\text{WS}_2$  [143][157][158][159]. The highest mobilities were recorded in  $\text{WS}_2$  grown at  $950\text{ }^\circ\text{C}$ , grown with either  $\text{H}_2\text{WO}_4 + \text{NaCl}$  or  $\text{WO}_3 + \text{NaCl}$ , which indicates a role of the growth temperature in improving the quality of the  $\text{WS}_2$ . As the temperature is lowered the difference between precursors becomes more pronounced in terms of the crystal quality. The  $\text{H}_2\text{WO}_4 + \text{NaCl}$  precursor system grown  $\text{WS}_2$  shows electron mobility of 10 to  $20\text{ }cm^2\text{V}^{-1}\text{s}^{-1}$  at temperatures of  $750\text{ }^\circ\text{C}$  and  $850\text{ }^\circ\text{C}$ . The electron mobilities of  $\text{WS}_2$

grown using  $WO_3 + NaCl$  are much lower,  $\sim 2 \text{ cm}^2 V^{-1} s^{-1}$  at 800  $^\circ\text{C}$ . Bilayer  $WS_2$  samples have overall greater electron mobility than their monolayer equivalent (between  $\sim 38 \text{ cm}^2 V^{-1} s^{-1}$  and  $52 \text{ cm}^2 V^{-1} s^{-1}$ ), similarly to the mechanically exfoliated flakes [160][159]. The electron mobility of bilayer  $WS_2$  ( $52 \text{ cm}^2 V^{-1} s^{-1}$ ) (Figure 6.17 and Figure 6.16) is also higher than that of other CVD grown  $WS_2$  as well as mechanically exfoliated onto  $SiO_2$  samples of  $WS_2$  reported [52][160][159]. The highest mobility has been obtained for bilayer system using  $WO_3 + NaCl$  indicating that the precursor choice is less important for electron mobility in such systems.

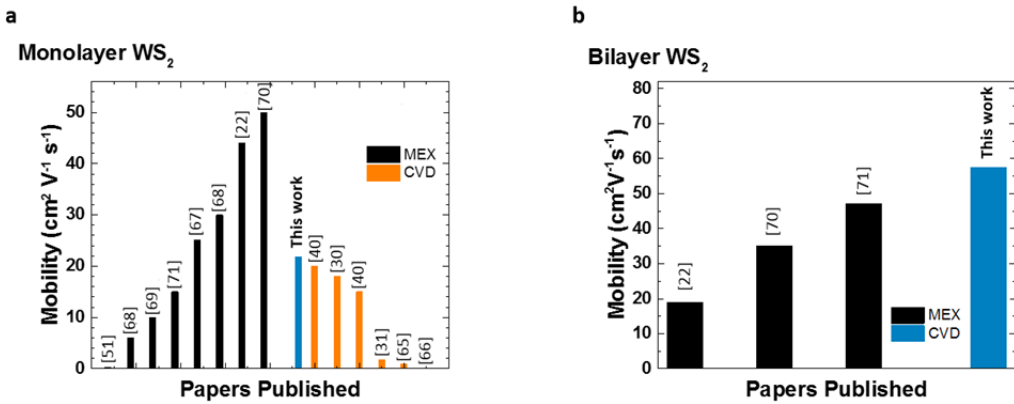


Figure 7.16: Comparison of electron mobility with literature for a) monolayer b) bilayer. Adopted from [136].

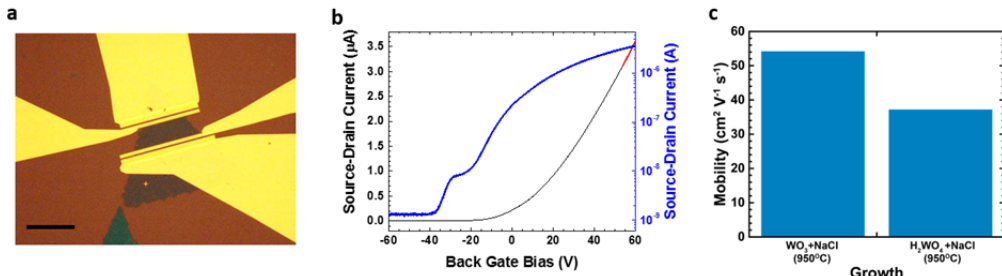


Figure 7.17: a) OM image of FET from bilayer  $WS_2$  (scale bar is  $30\mu\text{m}$ ); (b) FET transfer curve taken from  $WS_2$  made with  $WO_3 + NaCl/950 \text{ } ^\circ\text{C}$  c) electron mobility of double layer sample made with different precursors. Adopted from [136].

## 7.3 Conclusions

In conclusion a synthesis route has been developed that allows for high quality monolayer and bilayer  $WS_2$  CVD growth. This quality is demonstrated by highest recorded electron

FET mobility for both monolayer and bilayer CVD grown  $WS_2$  compared to the literature and comparable to that of mechanically exfoliated ones. Additionally, the triangle flakes grown using  $H_2WO_4 + NaCl$  are much larger (up to  $\sim 200 - 300\mu m$ ) compared to ones grown using standard  $WO_3$ . The CVD growth using  $H_2WO_4$  has also been demonstrated to work at lower temperatures, down to 750 °C compared to more commonly used 950 °C. Finally, the PL of the  $WS_2$  grown using  $H_2WO_4$  is uniform throughout the flake and has very narrow FWHM (36 meV) which again points to high crystal quality and lack of defects in form of sulphur vacancies. These findings allow to develop further the TMDCs synthesis method of CVD and can potentially lead to industrially scalable synthesis of monolayer  $WS_2$  or other TMDCs over large area.

# Chapter 8

## Transfer procedure of monolayer TMDCs from the native substrate to *SiO<sub>2</sub>/Si* wafer

### 8.1 Introduction

The most common method of producing the TMDCs is CVD. During the CVD growth the process the substrate and the sample are heated to very high temperatures, up to 1000 °C. Because of that there is substantial thermal expansion in both substrate and sample. However due to difference in thermal expansion coefficient between those two elements there is potential build up of thermal strain. Additionally because the substrate, upon which the sample is grown, is heated to such high temperatures that it cannot be used for electrical measurements. More specifically the thermal expansion coefficients of *WS<sub>2</sub>* and *SiO<sub>2</sub>* are on the order of  $10^{-3}$  and  $10^{-7} K^{-1}$  respectively [161][162]. Therefore it is expected that during cooling down the *WS<sub>2</sub>* will come under tension due to thermal expansion coefficient misalignment. There has been studies showing variation in PL position and FWHM under strain [163]. Similarly Raman peaks have also been shown to become shifted under strain, especially when using polarised light source [164]. Theoretical studies have also shown effect of change in lattice constants on electronic band structure of TMDCs [50]. Moreover in order to use TMDCs as components in devices different layers have to be arranged together either vertically or laterally. Due to aforementioned reasons there is a need to develop methods for transferring single layers of TDMCs from one substrate to another one. In this chapter a focus is put on transferring *WS<sub>2</sub>* monolayer

flakes from  $SiO_2/Si$  onto other surfaces.

## 8.2 Experimental

The most common method of transferring flakes synthesised via CVD method is a wet transfer method utilising as an intermediate substrate. In such procedure a thin layer of PMMA is first spun on top of the substrate. After drying the substrate is placed in a KOH aqueous solution (6% to 8%) heated to about 50 °C. As a result the thin layer of  $SiO_2$  on top of  $Si$  is dissolved leaving a PMMA with the sample attached to it floating on top of the solution. The PMMA is then rinsed in water several times and scooped up onto a new substrate. Next the sample is dried and annealed to ensure good adhesion and remove wrinkles and strain. Then the PMMA is removed with a solution of acetone and IPA at about 50 °C. Any remaining PMMA can be removed by annealing the sample at about 100 °C.

## 8.3 Results

A sample has been investigated using Raman and PL spectroscopy before and after transfer. In Figure 8.1 a comparison between samples before and after transfer can be seen in PL spectra. The as grown sample shows mostly homogeneous PL intensity, position and FWHM across the sample with the exception of the edge and trisecting lines in the middle where the PL intensity is higher and lower accordingly. In the sample after transfer the PL intensity, position and FWHM is more randomly distributed across the flake and there is a distinct lack of edge enhancement or the presence of trisecting lines.

The position of the PL peak from the as grown sample is  $1.97 \pm (9.84 \times 10^{-4})$  eV, while the PL peak position from transferred sample  $1.97 \pm (8.35 \times 10^{-3})$  eV. Therefore the peak position is shifted by 6.2 meV after transfer while the relative standard deviation is about 8.5 times greater in the transferred sample than in the as grown sample. The FWHM in the as grown sample is  $36.37 \pm 0.79$  meV while in the transferred sample the FWHM is  $83.27 \pm 6.79$  meV. The FWHM then increases by 46.90 meV while the relative standard deviation increases 3.72 times compared to the as grown sample.

The Raman  $E_{2g}^1$  peak position in the as grown sample is  $350.87 \pm 0.21\text{ }cm^{-1}$  while in the transferred sample is  $351.34 \pm 0.29\text{ }cm^{-1}$ . The relative uncertainty is therefore 1.39 greater in the transferred sample. The position of the Raman  $A_{1g}$  peak in the as grown

sample is  $418.65 \pm 0.28 \text{ cm}^{-1}$  while in the transferred sample it is  $417.32 \pm 0.48 \text{ cm}^{-1}$ . The relative uncertainty is therefore 1.69 times greater in the transferred sample. The position difference between these two peaks is  $67.79 \pm 0.24 \text{ cm}^{-1}$  in the as grown sample while it is  $66.01 \pm 0.48 \text{ cm}^{-1}$  in the transferred sample. The relative uncertainty increases therefore by 2.03 after the transfer. The intensity ratio between those peaks in the as grown sample is  $5.75 \pm 0.68$  and after transfer it is  $7.16 \pm 0.89$ . The relative uncertainty changes 1.58 times after transfer.

It can be therefore seen that after transfer the relative uncertainty increases for every parameter of Raman and PL spectra maps. This indicates that the sample after the transfer is much less homogeneous. Because both the position of PL as well as the position of Raman peaks is affected by the strain the inhomogeneity can indicate a relaxation or build up of strain. Since the CVD growth method involves heating up the sample and the substrate to very high temperatures, up to  $850^\circ\text{C}$ , there is possibility of residual thermal strain after cooling down. Since the PMMA is much more flexible than the  $\text{SiO}_2$ , that the sample is grown on, the  $WS_2$  can relax before being placed on a new  $\text{SiO}_2$  substrate. On the other hand the water present in between the  $WS_2$  and PMMA can also be a source of strain. During the water evaporation the surface tension can induce local strain leading to high inhomogeneity. The PMMA can also have varying thickness and can swell to small degree therefore contracting in size during drying. Any or all of these effects can potentially contribute to the variation in parameters observed.

The average values of peak fitting parameters can be then compared between the two sample states to estimate the strain in the sample. The average position of  $E_{2g}^1 + 2LA$  peak changes from  $350.8601 \text{ cm}^{-1}$  to  $351.34 \text{ cm}^{-1}$ , a  $0.48 \text{ cm}^{-1}$  difference. Since the position of this peak changes by  $-3.1 \text{ cm}^{-1}/\%$  this indicates the change in strain of  $-0.16\%$ . The  $E_{2g}^1 + 2LA$  peak intensity change ( $\Delta I/I_0$ ) of  $23.15\%$  indicates a  $0.23\%$  change in strain. The average value of  $A_{1g}$  peak position changes from  $418.65 \text{ cm}^{-1}$  to  $417.32 \text{ cm}^{-1}$ , a difference of  $1.33 \text{ cm}^{-1}$ . This indicates then a strain of  $-4.45\%$ . The intensity change of  $A_{1g}$  peak of  $25.64\%$  corresponds to  $0.33\%$  strain [164].

The PL peak position changes from 1.9765 eV to 1.9703 which corresponds to change from about 1% to 0.75% strain, a -0.25% change [163].

By comparing different average Raman and PL peaks fit parameters it is not clear to what extent the  $WS_2$  is strained before or after the transfer. Neither the direction nor the extent of strain can be estimated then in the sample overall. The difference in deviation of these values however indicates that the sample after transfer is less homogeneous than

before. Therefore while it cannot be said that the sample strain changes on average as a whole, there is a change in strain across the sample. While the thermal strain should result in the sample as a whole being under tension due to thermal expansion and contraction other effects could still take place like aforementioned variation in water presence, inhomogeneity of PMMA layer thickness or folds in PMMA layer.

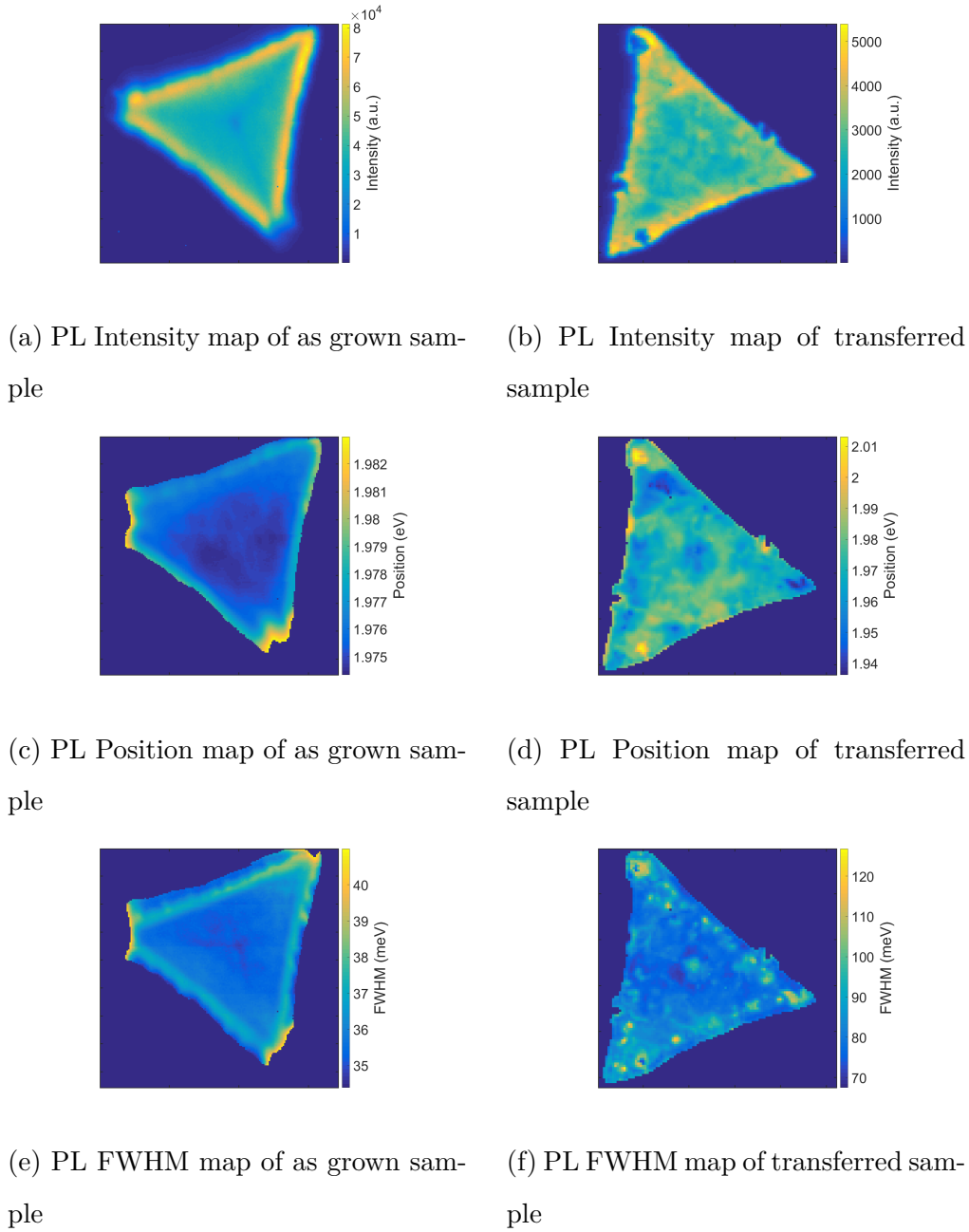
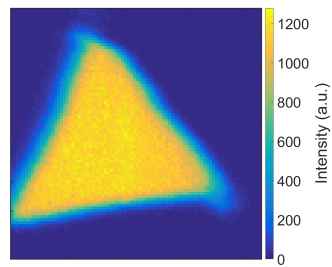
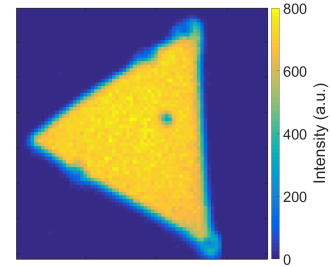


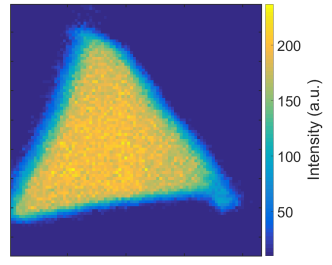
Figure 8.1: PL spectra maps of samples before and after transfer



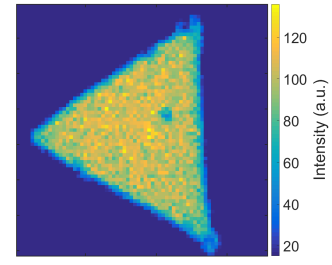
(a) Raman  $E_{2g}^1$  intensity map of as-grown sample



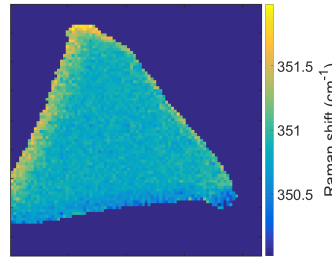
(b) Raman  $E_{2g}^1$  intensity map of transferred sample



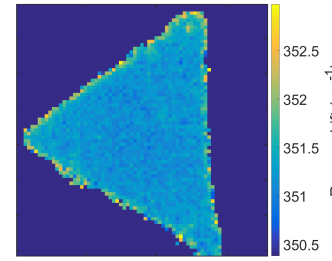
(c) Raman  $A_{1g}$  intensity map of as-grown sample



(d) Raman  $A_{1g}$  intensity map of transferred sample



(e) Raman  $E_{2g}^1$  position map of as-grown sample



(f) Raman  $E_{2g}^1$  position map of transferred sample

Figure 8.2: Raman spectra maps of samples before and after transfer

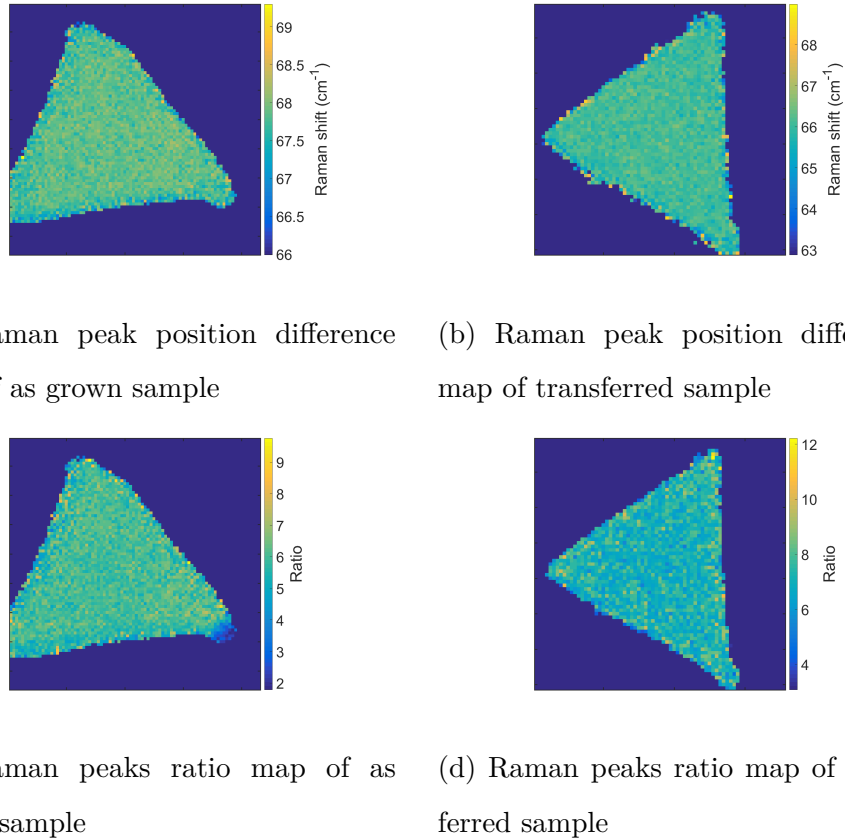


Figure 8.3: Raman spectra maps of samples before and transfer

## 8.4 Conclusions

In this Chapter we have presented the transfer methodology that we have developed in our own way for monolayer TMDCs. Overall the quality of the transfer material is good and the flakes are pristine in shape. It is unclear to what extent the CVD grown  $WS_2$  sample is strained prior to transfer or after it. The difference in relative uncertainty of different fitting parameters of PL and Raman spectra however reveals that the sample becomes less homogeneous following the procedure. This could indicate that a certain degree of strain is introduced as a result of the transfer. This in turn could be attributed to the presence of a non uniform distribution of water molecules, non uniform thickness of PMMA layer, folds in the PMMA layer or presence of residue PMMA.

# Chapter 9

## Post-transition metal doping of monolayer $WS_2$

### 9.1 Introduction

Single layer TMDC materials present a range of unique optical, electrical and mechanical properties which make them promising materials beyond graphene in future nanotechnologies. Atomic doping can further extend the potential of TMDCs since it has been predicted that a number of properties can be tuned through compositional variation. Up until now doping has relied on charge transfer induced by changing the environmental conditions such as surface adsorption, metal contacts and dielectric interfaces. This approach has demonstrated to severely limit the device working conditions thus doping through stable incorporation of non-volatile metal atoms is highly preferred. Achieving controlled doping is a challenge which is aggravated by the fact that established synthesis protocols for these materials are still lacking.

Doping of monolayer  $WS_2$  with post-transition metals has not been reported as yet. Doping of  $WS_2$  with post-transition metals can lead to chemisorbed intercalated atoms between layers which can be regarded as analogous to deep level impurities. It can lead to an additional energy level near to the top of the valence band or, alternatively, as a modification of the energy band of the host crystal due to the interaction between the intercalate and W or S atoms [165][166]. In particular indium may generate an additional energy state at the top of the valence band which leads to a subsequent upward shift of this band [167]. A gradual increase in this shift with increasing number of intercalating atoms would lead to a linear decrease in the energy gap with increasing In content as observed in

In-intercalated bulk  $WS_2$  [167]. This led to the demonstration of higher conductivity and photocurrent than both pure  $WS_2$  films thus proving to be highly photo-active. Unlike their alkali and alkaline earth metal analogues, In-intercalated bulk  $WS_2$  compounds were found to be stable against oxidation when exposed to air or chemical due to a fairly strong guest-host bonding which hinders deintercalation processes and preserving a perfect 2H crystalline phase [167][168]. Further, In has lower melting and boiling points than B, Al and Ga enabling doping via CVD or MOCVD synthesis of  $WS_2$  at low temperatures. These characteristics make Indium a very interesting prospected dopant of  $WS_2$  to pave the way towards applications as photoelectrodes in solar cells. Post transition metals are prone to intercalate between the layers however displaying very different effect with respect to the alkali and alkaline earth metal intercalates of  $WS_2$ .

Here we demonstrate indium doping of monolayer  $WS_2$  in-situ during CVD synthesis of  $WS_2$ . The process relies on the addition of a volatile indium precursor which results in large-area In-doped  $WS_2$  atomic layers exhibiting tunable optical properties and a semiconducting-to-metallic transition at high doping levels. We also demonstrate controlled indium content from 0 up to 45% in  $WS_2$  maintaining a 2D morphology and atomically thin nature of the material without sacrificing the lateral extension and scalability of the synthesis process.

## 9.2 Results

The In doped  $WS_2$  samples were grown by following the synthesis route developed for the monolayer  $WS_2$  as discussed in Chapter 6 [136]. The main change was to add  $In(OH)_3$  powder as an indium precursor to the same crucible as W precursor. Such mixed powders in a crucible were then placed in the centre of the furnace similarly to the established procedure.

A first indication of the effect of indium in the  $WS_2$  is provided by the morphology of the triangular domains. SEM and OM images of  $WS_2$  domains grown by using different  $In(OH)_3/H_2WO_4$  weight ratios [ $In_{0.25}WS_2$ ,  $In_{0.5}WS_2$ ,  $In_{0.75}WS_2$ ,  $In_1WS_2$ ] are shown in Figure 9.1. While from the optical contrast it is possible to see that the monolayer nature of the domains is unchanged, it can be noticed how the shape of triangles progressively change. Triangles with straight edges similar to that of pristine  $WS_2$  are displayed for low In content while convex and jagged edges appear by increasing the Indium content, which might suggest a more significant incorporation of the latter.  $WS_2$  with high indium

content can also present different morphologies and even large coverage.

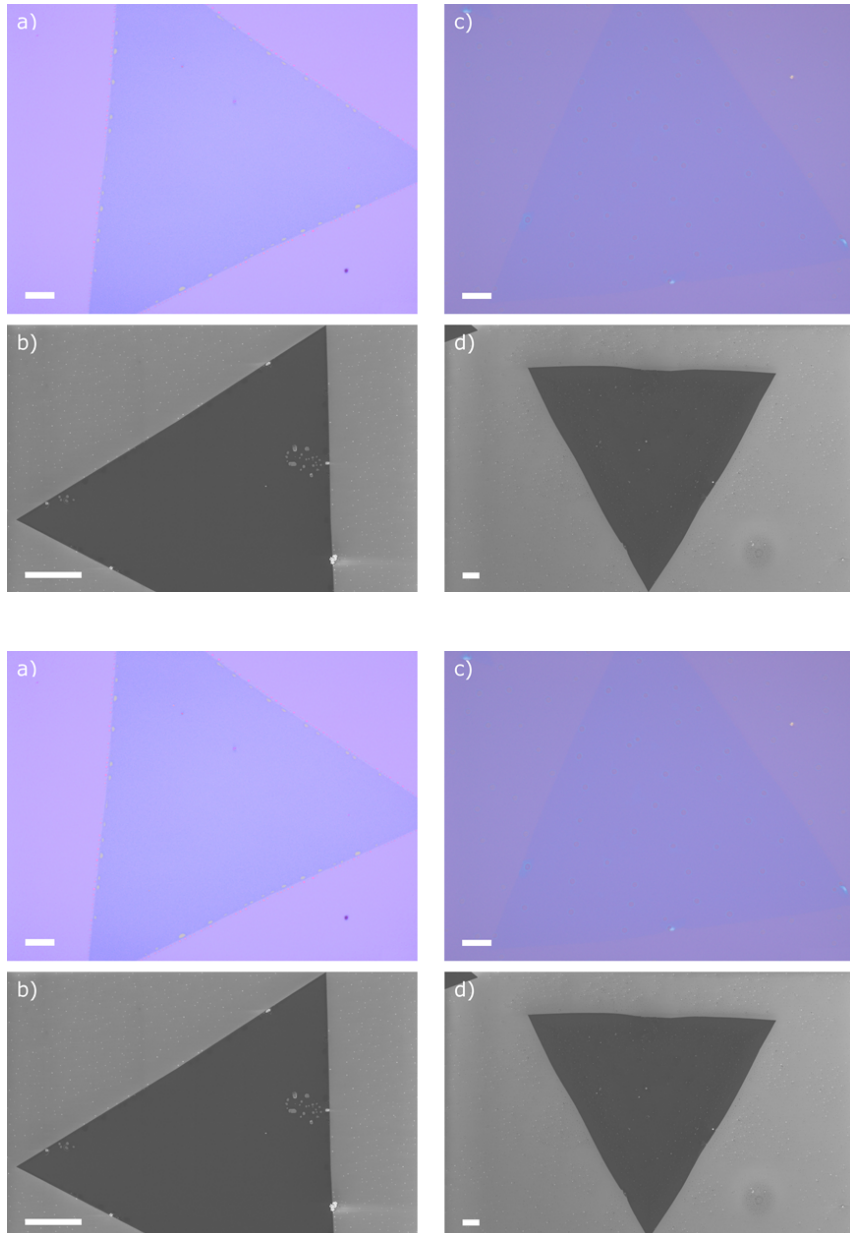
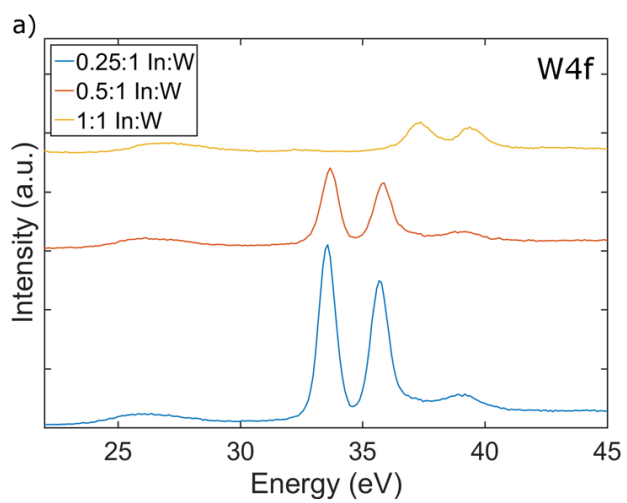


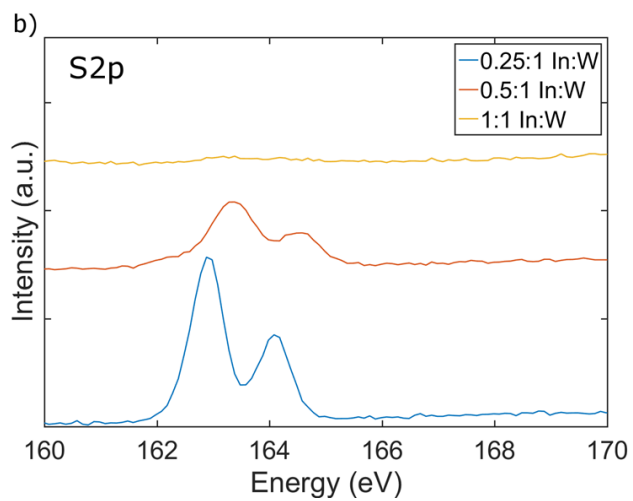
Figure 9.1: OM and SEM images of flakes grown with different  $In(OH)_3/H_2WO_4$  weight ratios: (a, b) 0.25, (c, d) 0.5, (e, f) 0.75 and (g, h)=1.

The samples were further characterised using XPS to assess the exact chemical content and therefore the level of doping.

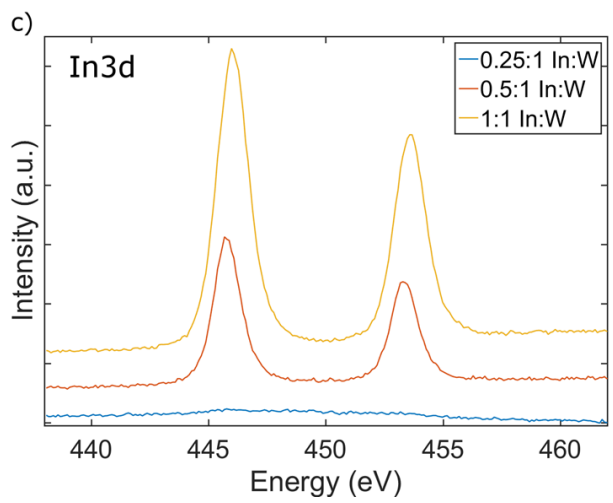
Figure 9.2 shows the In 3d, W 4f and S 2p core levels XPS spectra for pure  $WS_2$  and In-doped  $WS_2$  ( $In/W=0.25$ ,  $In/W=0.5$ ,  $In/W=1$ ). It is immediately noticeable that the sample with 0.25:1 In:W precursor ratio does not exhibits any In 3d peak. At the same time the samples with 0.5:1 In:W as well as 1:1 In:W show pronounced In 3d<sub>5/2</sub> core



(a) W 4f



(b) S 2p



(c) In 3d

Figure 9.2: XPS spectra comparison

level peak at 445.8 eV and 446.0 eV respectively and In 3d3/2 at 453.3 eV and 453.8 eV respectively. This slight shift might be attributed to the presence of  $In_xW_yS_z$  compounds [169]. The In 3d core levels for 1:1 In:W sample are also about twice as intense as the ones for the 0.5:1 In:W sample. Furthermore the W 4f core levels for the 1:1 In:W sample are significantly shifted to the blue which might indicate presence of  $W^{6+}$  in the doped sample compared to  $W^{4+}$  to pure  $WS_2$ . This would indicate bonding between W and In atoms. The S 2p1/2 and S 2p3/2 core levels for 0.25:1 In:W ratio can be observed at 162.9 eV and 164.1 eV respectively while for the 0.5:1 In:W sample they are at 163.4 eV and 164.6 eV respectively. No to very weak peak can be observed for the 1:1 In:W ratio sample. There is therefore indication of interaction between the S and In atoms, with stronger S 2p core level peak shifts than those of the W 4f core levels. It is therefore possible that the In atoms became chemisorped on the surface, intercalated in between the layers or incorporated as an interstitial. The stoichiometric composition was then calculated using the concentrations of elements from peak integration of In 3d, W 4f and S 2p core levels as seen in Table 9.1.

Table 9.1: In:W and S:W ratios obtained by calculating the In, W and S concentrations from the integrated intensity of the In3d, W4f and S2p core levels.

Sample	In/W	S/W
In/W = 0.25	0.038:1	2.32:1
In/W = 0.5	0.45:1	2.22:1
In/W = 1	1.98:1	0.27:1

The XRD diffraction patterns of all the In-doped  $WS_2$  samples can all be indexed on a hexagonal unit cell basis (Figure 9.3a) and an analogy can drawn to the pattern of  $2H - WS_2$ . The most intense reflection is the (002) and for pure and In-doped  $WS_2$  (Figure 9.3b) it can be seen that the FWHM decreases as the In precursor concentration increases and that a peak shift towards a larger d spacing (Table 9.2) occurs for the highest indium content. Additionally the samples with indium content of In/W=0.5, In/W=0.75 and In/W=1 show an additional reflection at  $2\Theta = 13.44$  not belonging to  $WS_2$ , which can be an indicator of successful incorporation of In atoms.

Table 9.2: Data for the (002) XRD peak and lattice parameters for pure  $WS_2$  and In-doped  $WS_2$  samples.

Sample	Position ( $2\Theta$ )	FWHM ( $2\Theta$ )	a ( $\text{\AA}$ )	c ( $\text{\AA}$ )	d ( $\text{\AA}$ )
$WS_2$	14.44	0.703	3.23	11.02	5.51
In/W = 0.25	14.47	0.294	3.23	11	5.50
In/W = 0.5	14.444	0.168	3.22	11.02	5.51
In/W = 0.75	14.479	0.137	3.22	11	5.50
In/W = 1	14.307	0.182	3.21	11.14	5.57

Therefore, it can be concluded that the crystal structure remains unchanged for Indium content of less than 0.038, corresponding to a precursor ratio of In/W = 0.25. For large indium contents an expansion of the van der Waals gap is observed due to the large amount of indium intercalated between the layers in few-layered regions and also a small portion of indium can result incorporated in the crystal structure.

Our results are comparable to previous reports on the In intercalation in bulk  $MoS_2$  which showed that smaller ions can lead to a significant change in the crystallographic order [170] changing it to a octahedral coordination, while the large metal ions (In, Ga) do not disrupt it but instead preserve the hexagonal structure. The presence of d-bands in indium metal contributes additionally to the bonding stabilization.

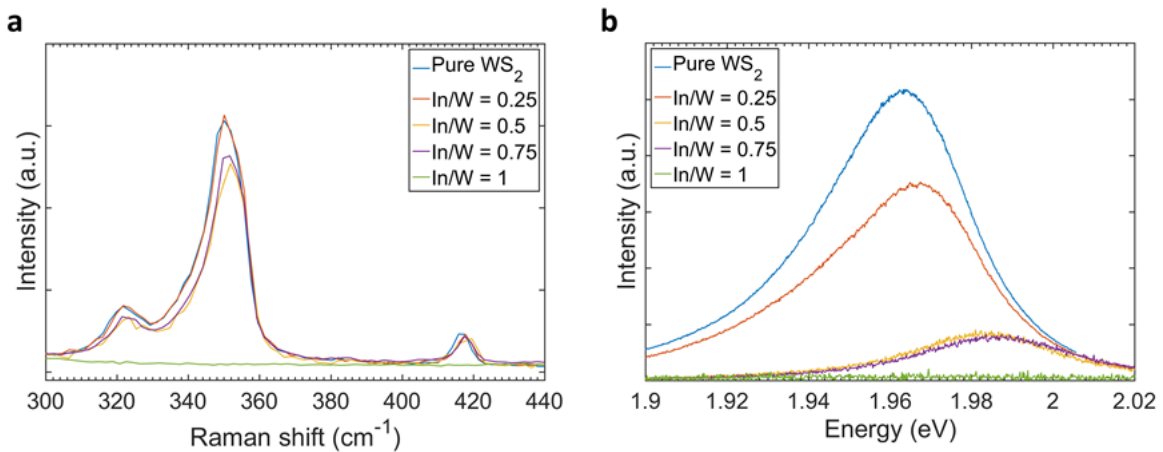
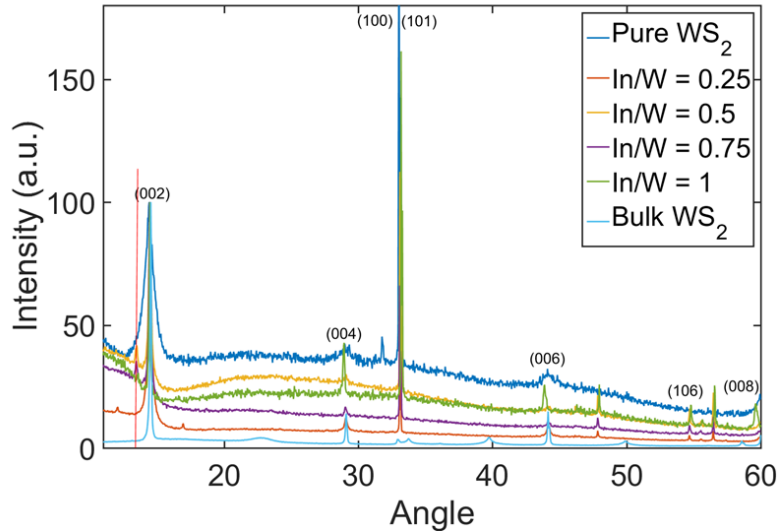
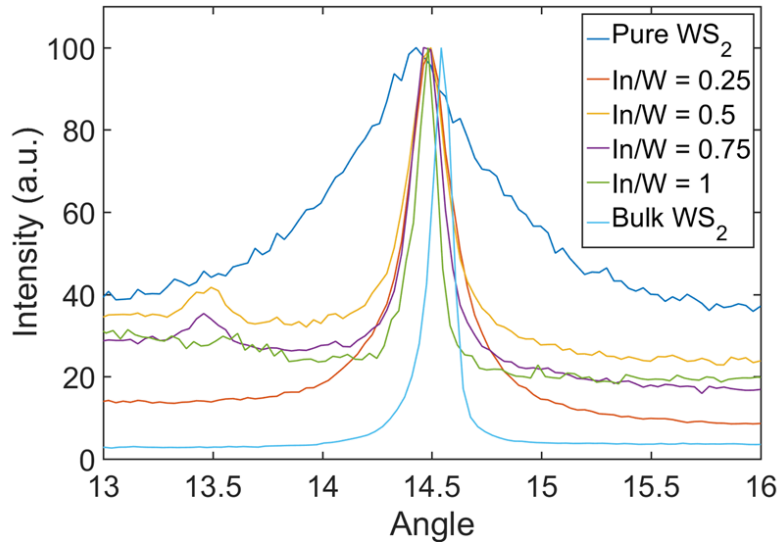


Figure 9.4: Representative a) Raman and b) PL spectra for pure  $WS_2$  (grown by using  $H_2WO_4$  as metal precursor) and In-doped  $WS_2$

Further evidence of  $In_2S_3$  can be inferred by the presence of peaks at  $2\Theta = \sim 48$  and  $\sim 57$  [171], specifically the (002) plane. This has been observed in the form of thick



(a) XRD patterns for CVD-grown pure  $WS_2$  and In-doped  $WS_2$ .



(b) (002) XRD peak for CVD-grown pure  $WS_2$  and In-doped  $WS_2$

Figure 9.3: XRD spectra of  $WS_2$  samples

crystals in the centre of atomically thin flakes (Figure 9.5) and has been confirmed by Raman (Figure 9.5). The  $In_2S_3$  have been rarely observed and can therefore be the result of secondary reaction products.

The representative Raman spectra for undoped  $WS_2$  and In-doped  $WS_2$  are reported in Figure 9.4 a). It can be observed that  $WS_2$  sample with In:W ratio of 0.25:1, 0.5:1 and 0.75:1 show the characteristic in-plane  $2LA - E_{2g}^1$  and out-of-plane  $A_{1g}$  vibrational Raman active modes of  $WS_2$ , while the sample with In content of 1 is not Raman active. Similarly,  $WS_2$  with In content between 0.038-0.45 exhibit PL while  $WS_2$  with In content

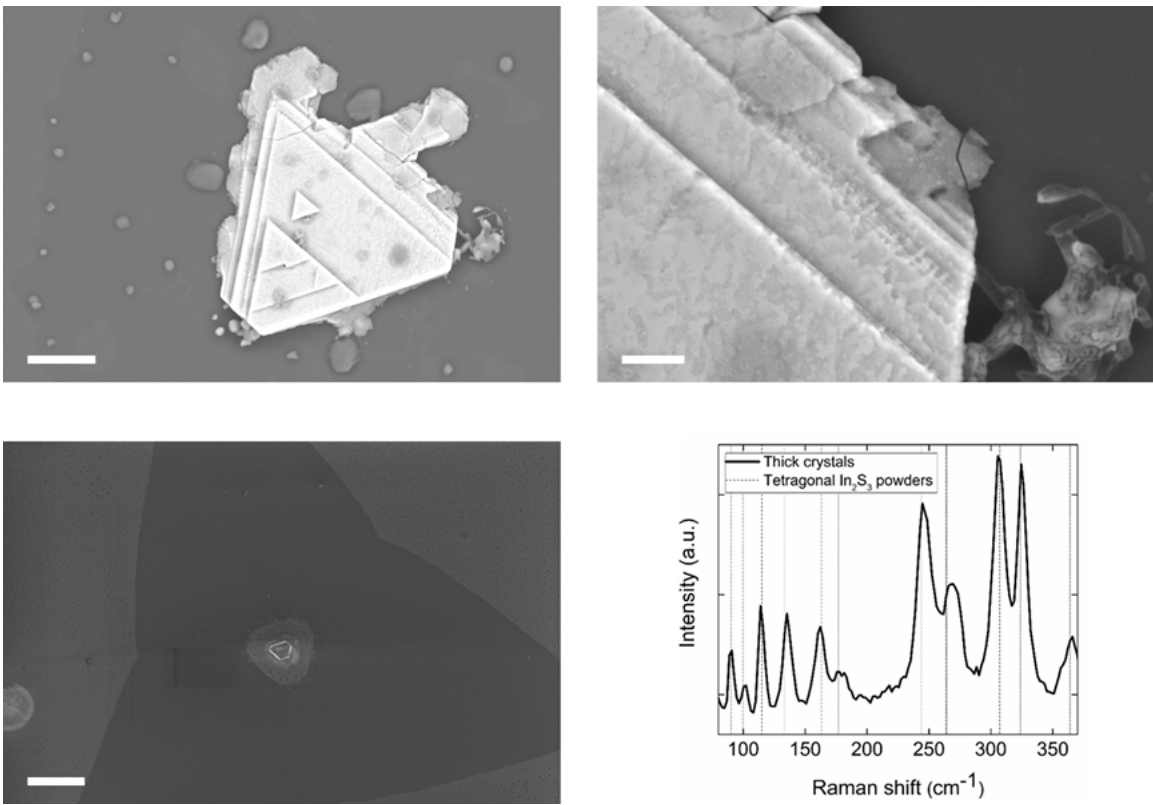


Figure 9.5: Low-magnification SEM images in (a) SE and (b) BSD imaging mode of the same area of sample In/W=1. High-magnification SEM images in (c) SE and (d) BSD imaging mode of the same area of sample In/W=1, revealing compositional variation across the flakes

of 1 does not luminescence (Figure 9.4 b)). Therefore, a very large amount of In (equal to 1) changes the crystal lattice and properties of the base material. The  $E_{2g}^1$  and  $A_{1g}$  Raman peaks (Figure 9.7) of the 0.25:1, 0.5:1 and 0.75:1 In-doped samples are shifted towards higher frequencies ( $E_{2g}^1$  at  $\sim 351.5\text{cm}^{-1}$  and  $A_{1g}$  at  $\sim 418\text{cm}^{-1}$ ) as compared to pure  $WS_2$  sample. This could be due to the differences in the binding energy between W–S and (W-In)–S bonds. The shifts in Raman peak position observed in mono and few layer thick TMDCs are however not fully yet understood and further characterisations are necessary.

The excitons-to-trions ratio (Figure 9.8) calculated for the samples that exhibit PL is lower compared to that of the undoped  $WS_2$ , which indicates increase in n doping behaviour as the In content increases. It can be explained due to the presence of fully filled d-orbital in In atoms with an additional electron in the p-orbital in the most outer shell. These extra electrons may therefore contribute to the semiconductor to metal transition with high enough In concentration. To confirm that electrical measurements

were performed, which revealed direct increase in resistivity with increase in temperature which is indicative of the metals (Figure 9.6).

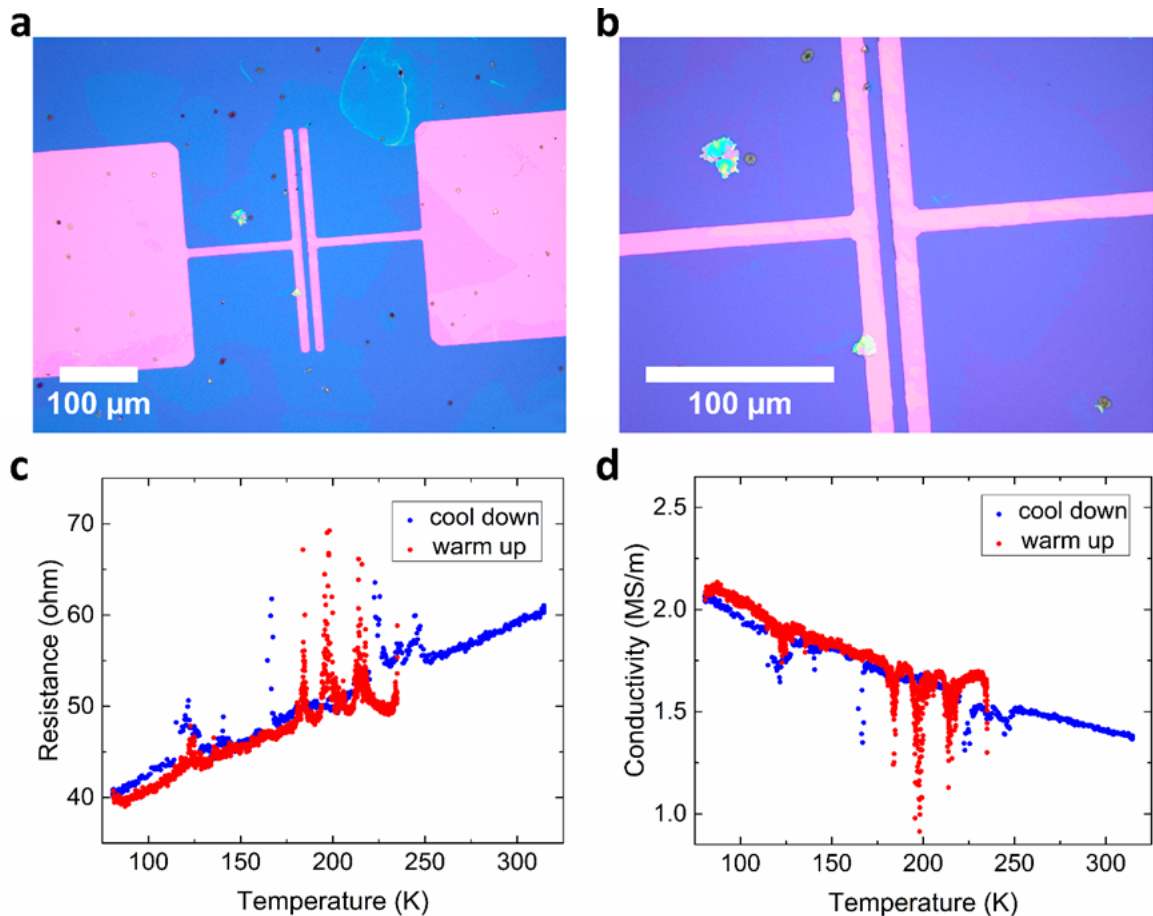


Figure 9.6: (a, b) Optical micrographs of Ti and Au contacts deposited on In/W=1 flakes. (c) Measured resistance as a function of temperature. (d) Calculated conductivity vs. temperature revealing a semi-metallic behaviour.

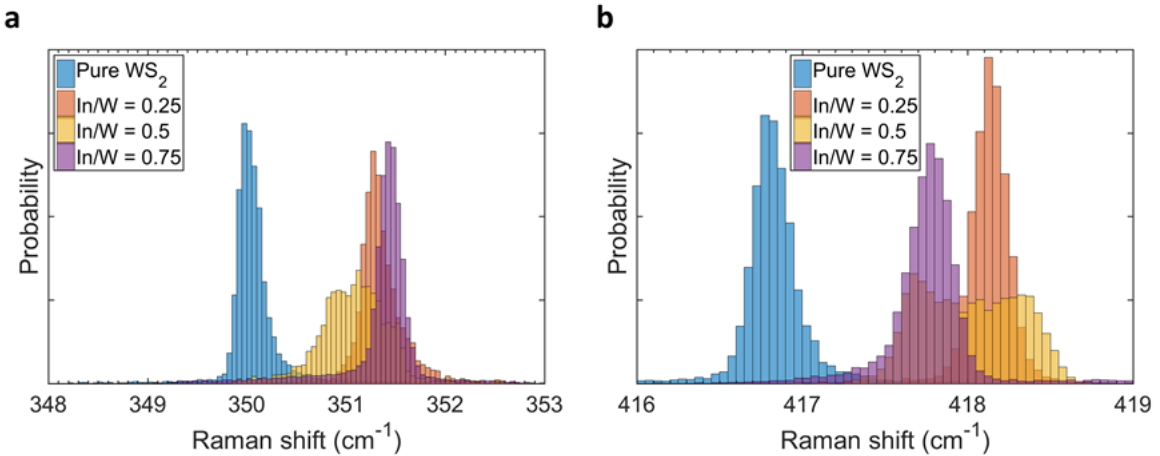


Figure 9.7: a)  $E_{2g}^1$  and b)  $A_{1g}$  peak positions for pure  $WS_2$  and Raman active In-doped  $WS_2$  samples.

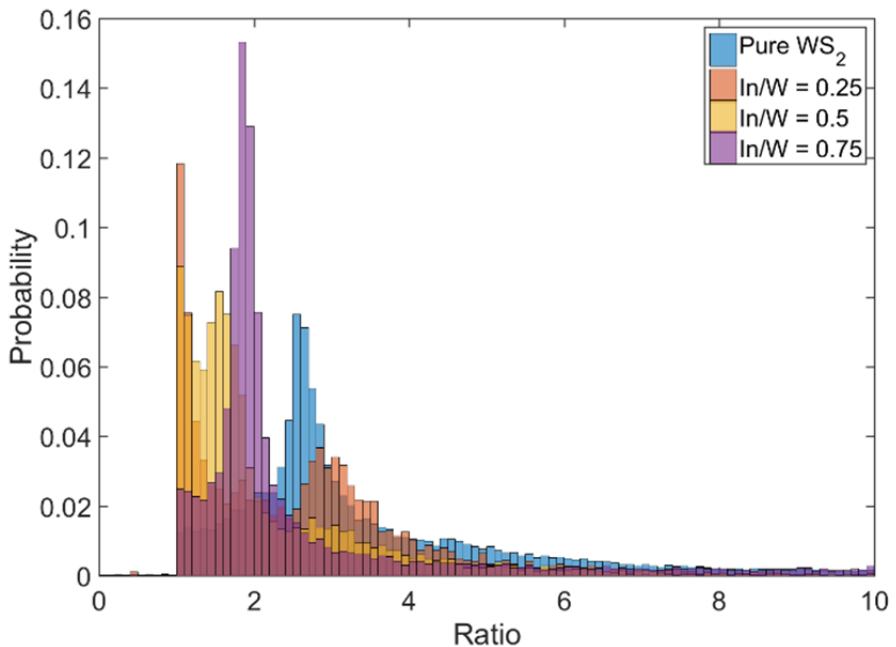
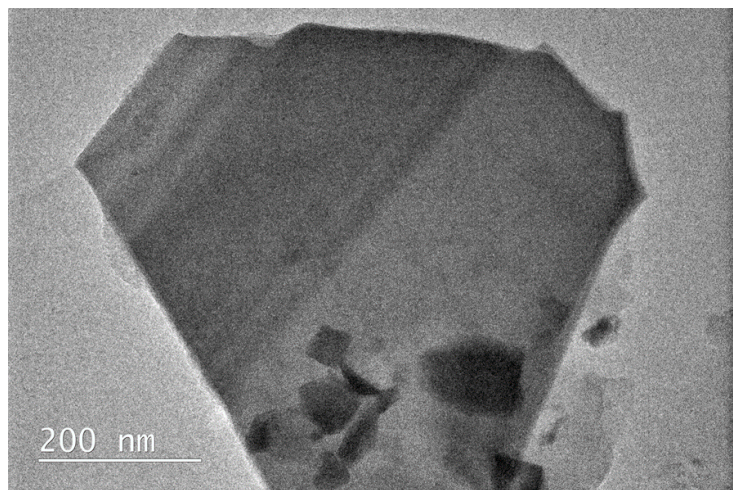


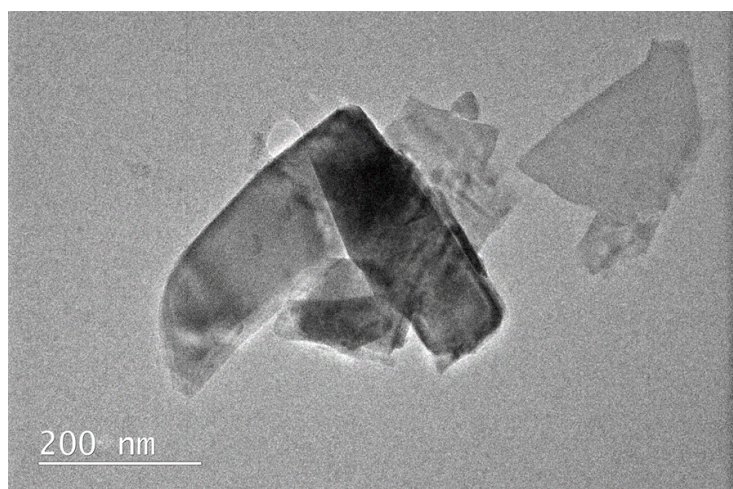
Figure 9.8: Excitons-to-trions ratio for pure  $WS_2$  and PL active In-doped  $WS_2$  samples XPS

The sample with In:W growth ratio of 0.5:1 was further analysed using transmission electron microscopy (TEM). In order to prepare the samples for the measurement the as grown flakes of  $WS_2$  on  $SiO_2/Si$  have to be transferred onto a TEM grid made of thin (200 nm) carbon layer stretched across copper grid. The samples were therefore transferred using the standard wet transfer method described in chapter 8. Due to irregular surface of TEM grid consisting of shallow holes as well as delicate carbon film the wet transfer

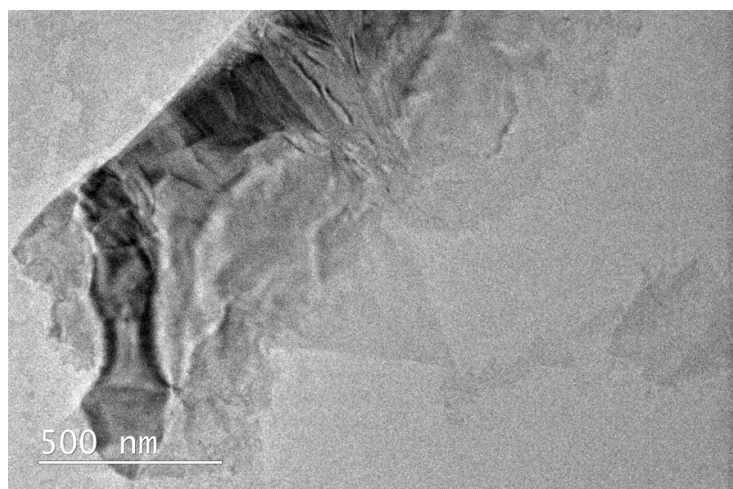
method proved to be less efficient than when transferring onto a flat  $SiO_2/Si$  surface. Due to acetone bath and several steps of heating and cooling the carbon film breaks in many places leading to partial loss of the transferred material. The TEM images of the transferred  $WS_2$  flakes can be seen in Figure 9.9. The contrast in those images is primarily caused by the size of the atoms with smaller atoms of C contributing very little and being barely distinguishable from an empty space, while the bigger W atoms resulting in much more noticeable contrast. The Figure 9.9a shows relatively thick  $WS_2$  flake of < 10 layers with some smaller areas of more layers. The Figure 9.9b shows a folded and crumpled flake with thickness ranging from few, 2-3 layers up to very thick. There is also a thin, flat flake on the right side which retained most of the triangular shape. In Figure 9.9c there is a larger crumpled flake seen across the image. In the center there is one corner of a thin, flat triangular flake.



(a)



(b)

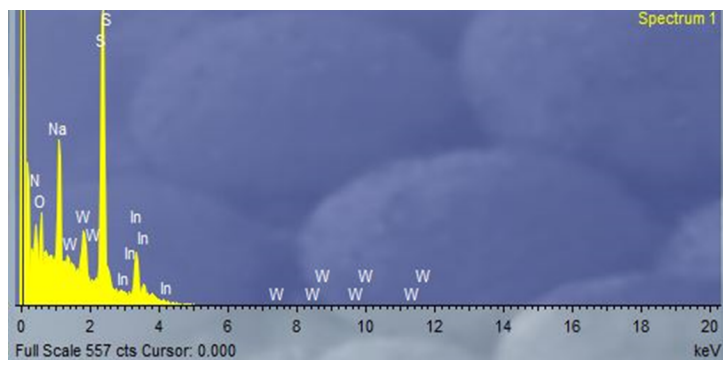


(c)

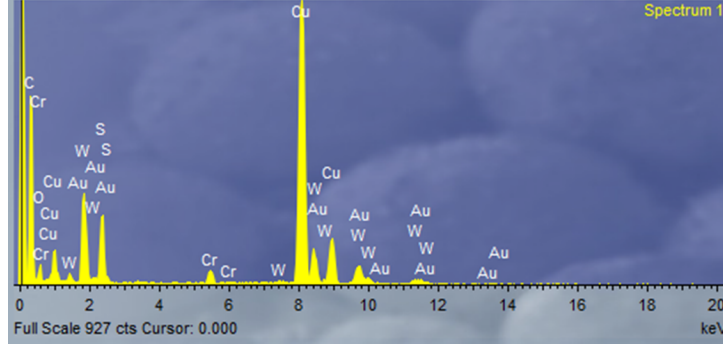
Figure 9.9: TEM images of the  $WS_2$  sample with  $In : W = 0.5 : 1$ 

The energy dispersive x-ray spectroscopy (EDS) has been then utilised to find the chemical makeup of the sample. First the as grown sample was characterised using SEM

EDS which requires no sample transfer. As seen in Figure 9.10a there are In peaks present at:  $L_{\alpha 1} = 3286.94\text{eV}$ ;  $L_{\alpha 2} = 3279.29\text{eV}$ ;  $L_{\beta 1} = 3487.21\text{eV}$ ;  $L_{\beta 2} = 3713.81\text{eV}$ ;  $L_{\gamma 1} = 3920.81\text{eV}$ . This indicates that there is some In in, on or around the  $WS_2$  flake. There is also visible Na peak which indicates remaining Na from  $NaCl$  used for synthesis. In order to compare the as grown sample, the transferred sample was characterised using TEM EDS. AS seen in Figure 9.10b there is no visible In peak. This indicates that the In is somehow removed during the transfer process. It is therefore most likely that the In is not present inside the  $WS_2$  as a dopant, as substitution or an interstitial, or that it is located in between the layers, but that it is present on top of or around the as grown  $WS_2$  flake.



(a) Before transfer



(b) After transfer

Figure 9.10: EDS spectra collected using TEM from  $WS_2$  sample with  $In : W = 1 : 2$

Additionally the electron diffraction (ED) measurement was performed. As seen in Figure 9.11 the present pattern correspond to the expected pattern for  $WS_2$ . The spots are sharp and narrow indicating mostly monolayer  $WS_2$  with no elongation or broadening expected due to the presence of irregular presence of doping element. There is also no additional pattern that could indicate a super structure of ordered atoms of the dopant. The faint halo indicates presence of the amorphous carbon of the TEM grid. The faint

signal is therefore indicative of a lack of polymer remains after the transfer. Finally the calculated lattice parameter  $a$  was found to be  $a = 2.71 \text{ \AA}$  which is in agreement to the  $a$  parameter found for the un doped  $WS_2$  from the XRD spectrum as seen in Figure 9.3 ( $a = 2.71 \text{ \AA}$ ) as well as the one found for the bulk  $WS_2$  ( $a = 2.73 \text{ \AA}$ ). This indicates therefore that the transferred sample shows no change in strain after the transfer.

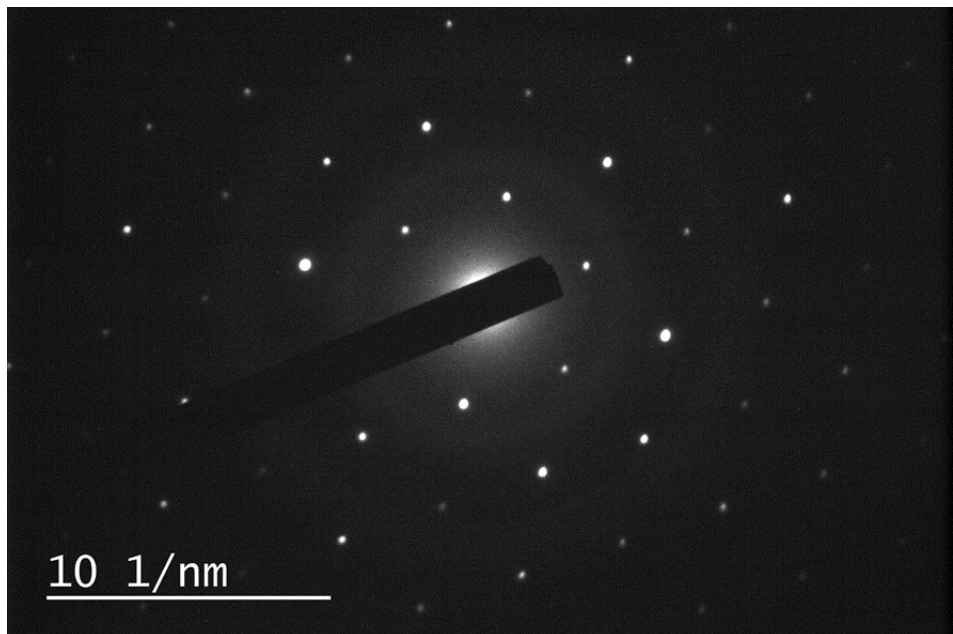


Figure 9.11: Electron diffraction pattern of  $WS_2$  flake with  $In : W = 1 : 2$

### 9.3 Conclusions

In summary, we have reported indium atoms doping of  $WS_2$  atomic layers in situ during synthesis, without sacrificing the lateral extension or the reproducibility of the synthesis process. Remarkably, the In-doped  $WS_2$  samples exhibit tunable light emission and a semiconducting-to-semimetallic transition at high doping levels. Therefore, the present synthesis strategy can be employed to achieve tailorabile optical and electrical characteristics of atomically-thin  $WS_2$  through stable incorporation of non-volatile post-transition metal atoms.

# Chapter 10

## CVD of mono-few-layered 2H $WSe_2$

### 10.1 Introduction

In this chapter we present our work on the characterization of CVD monolayer  $WSe_2$ . The novelty of this work resides in the use of a solid state inorganic precursor of Se for the first time which replaces the commonly used toxic  $H_2Se$  and Se powder in presence of Hydrogen gas. The purpose of the work reported here is to assess the quality of the  $WSe_2$  synthesized using this precursor as compare to the current literature.  $WSe_2$  is a TMDC material very similar to the  $WS_2$ . In its 2H semiconducting form the main difference between 2H  $WSe_2$  and  $WS_2$  is its optical bandgap which for monolayer is about 1.65 eV compared to 2 eV for  $WS_2$ . This allows for potential application in the near infrared range. Its crystal structure is the same as the other TDMCs as outlined in 2.

### 10.2 Results

The  $WSe_2$  were grown using standard growth procedure developed for growth of the  $WS_2$ . The mix of  $H_2WO_4$  and  $NaCl$  was placed in one crucible near the target substrate while  $ZnSe$  powder was placed in a separate crucible in a separate heating element. The growth was performed at 850 °C and W and S precursors were exposed to the same temperature in order to enable the evaporation. The resulting flakes as seen in Figure 10.1 are triangularly shaped similarly to the  $WS_2$  flakes. The monolayer flakes are up to about 30  $\mu m$  and are similarly distributed to the growths observed for  $WS_2$ . The  $WSe_2$  triangles optical images also show relatively thin strip of contrast along the border.

These flakes have been characterized by PL and Raman spectroscopy (Figure 10.2.

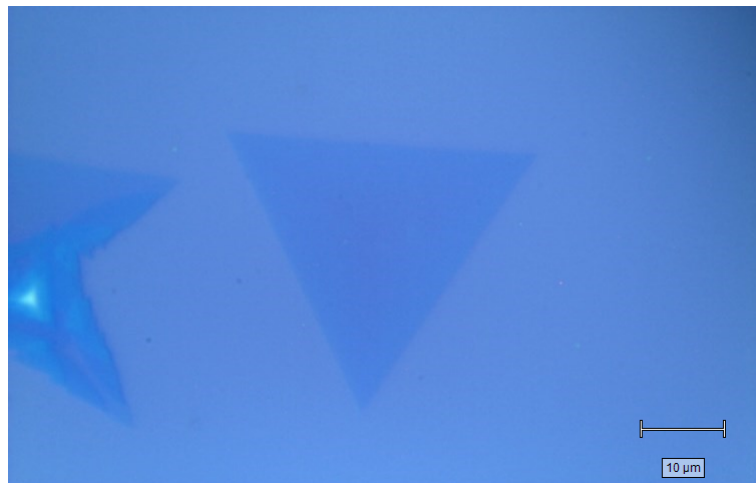
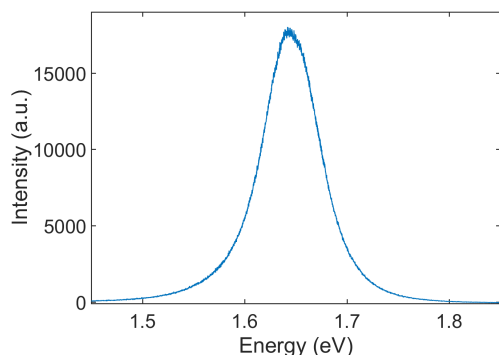
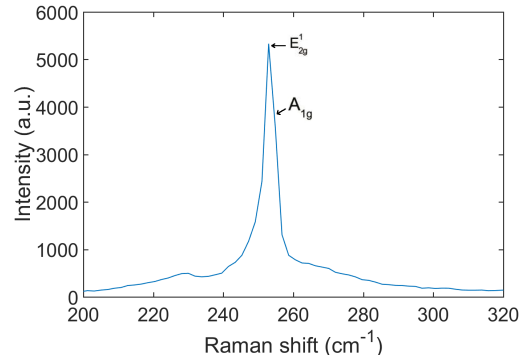


Figure 10.1: An optical micrograph of the  $WSe_2$  monolayer flake

A typical PL and Raman spectrum can be seen in Figure 10.2. The peak is centred at 1.65 eV which suggest a monolayer nature of the flake (as the direct band gap of monolayer is 1.65 eV) and the peak appears mostly symmetrical with FWHM of 66 meV. The symmetry of the peak and the fact it can be fitted with a single function, suggest a negligible contribution from trions in contrast we what observed for  $WS_2$  flakes. The Raman peak around  $250\text{ cm}^{-1}$  is a convolution of 2 peaks, an  $E_{2g}^1$  and  $A_{1g}$  vibrational modes, as already observed for bulk as well as exfoliated  $WSe_2$ .



(a) Typical PL spectrum from monolayer  $WSe_2$



(b) Typical Raman spectrum from monolayer  $WSe_2$

Figure 10.2: PL and Raman spectra from monolayer  $WSe_2$

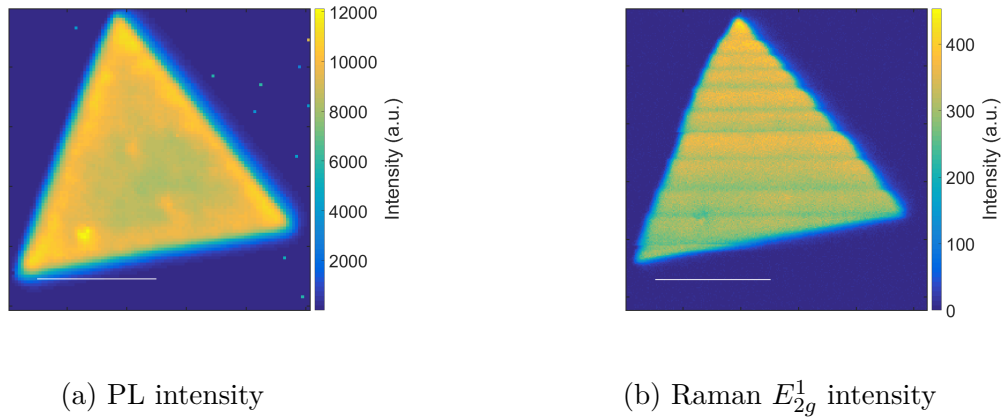


Figure 10.3: PL intensity and Raman  $E_{2g}^1$  intensity maps

A typical map of PL intensity of a  $WSe_2$  sample can be seen in Figure 10.3a. The PL intensity is homogeneous throughout the flake. It does not exhibit the trisecting pattern as seen in  $WS_2$  samples e.g. Figure 10.3a.

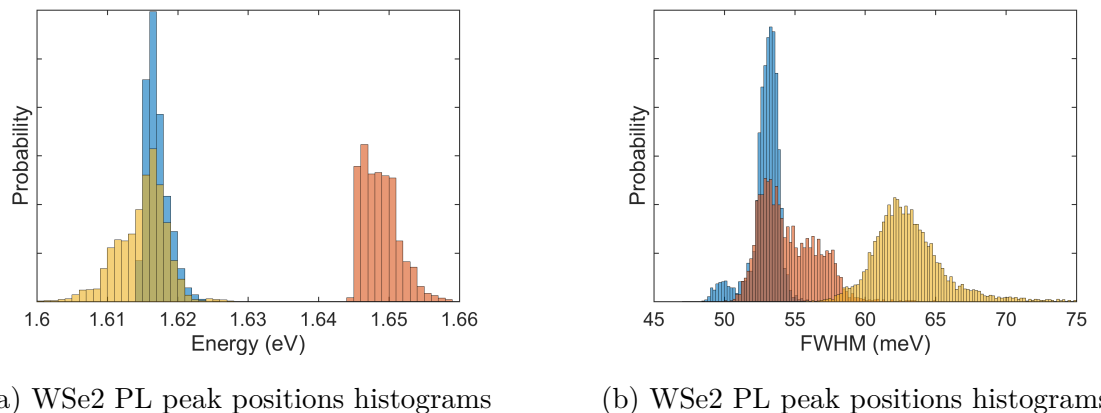


Figure 10.4: Comparison of PL peak positions and widths in different  $WSe_2$  samples

A comparison of PL peak positions and widths between different samples of  $WSe_2$  can be seen in Figure 10.4.

By plotting the intensity and width of the PL peaks against the peak position as seen in Figure 10.5 certain patterns can be observed. The intensity is mostly grouped around maximum values and relatively narrowly spread across the position spectrum. The thick flakes show much more even distribution of intensity across the position, which combined with the wide distribution of positions results in a much more inhomogeneous sample. The width and positions are generally well grouped with flakes with smaller width having more narrow distribution than those with greater width. Also few-layer flake shows a

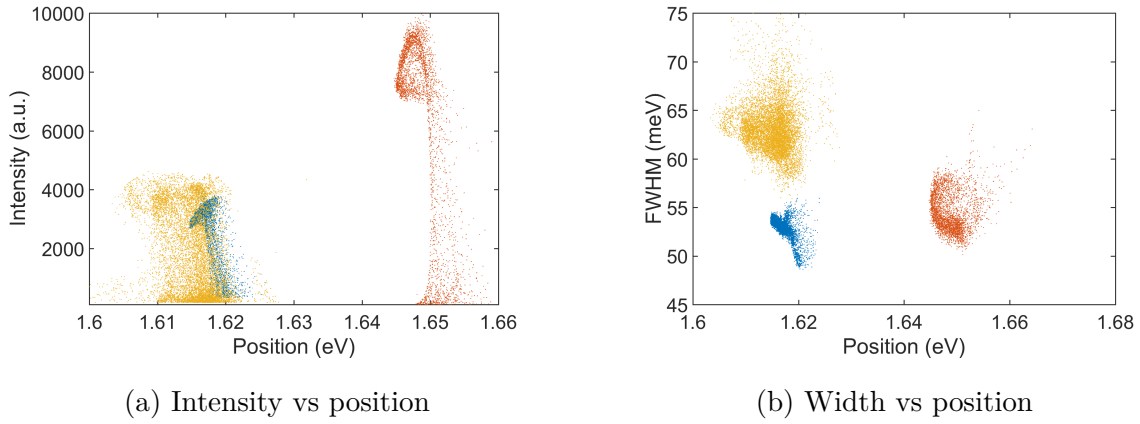


Figure 10.5: PL peak parameters distribution

smaller peak width. Overall there is no obvious relation between position and width.

The Raman spectroscopy is a very useful characterisation technique for TMDCs. For most TMDCs it can be used to identify the number of layers or strain within the layer. However in the case of  $WSe_2$  the position of the  $E_{2g}^1$  and  $A_{1g}$  largely overlaps and therefore it is difficult to accurately determine the difference in their position. Because of that this method of identifying the number of layers cannot be employed easily. It is however still possible to examine the strain within the layers by noting the shift of the  $E_{2g}^1$  peak. A Raman  $E_{2g}^1$  peak position distribution from a representative sample can be seen in Figure 10.6. The strain can be then determined from the mean position of  $250.678 \pm 0.095 \text{ cm}^{-1}$  to be 2.44 % [164].

The sample has been further characterised with XPS. Three areas were selected for measurements, one with thin, mono or double layer  $WSe_2$ , one with thick bulk  $WSe_2$  and one with no visible  $WSe_2$  flakes. The Figure 10.7 shows W4f core levels measured in those spots. The first area (Figure 10.7a), with thin flake shows one doublet at 32.08 eV and 34.23 eV and a second doublet at 35.33 eV and 37.68 eV. The first doublet corresponds to  $WSe_2$  while the second one can be attributed to  $WO_3$ . Since the spot size in the measurement covers both the flake as well as some surrounding substrate it is possible that the  $WO_3$  is located outside of the flake. Furthermore the background indicates that the emission from  $WSe_2$  came from surface and therefore the  $WSe_2$  flake is not contaminated with  $WO_3$ . The second area with thicker flakes (Figure 10.7b) shows similarly two doublets: one at 32.28 eV and 34.43 eV and a second one at 35.38 eV and 37.63 eV. Similarly to the thin area with thin flake we can ascribe the former to the  $WSe_2$  and the latter to  $WO_3$ . There is a small shift of 0.2 eV between  $WSe_2$  from the thin flake and  $WSe_2$

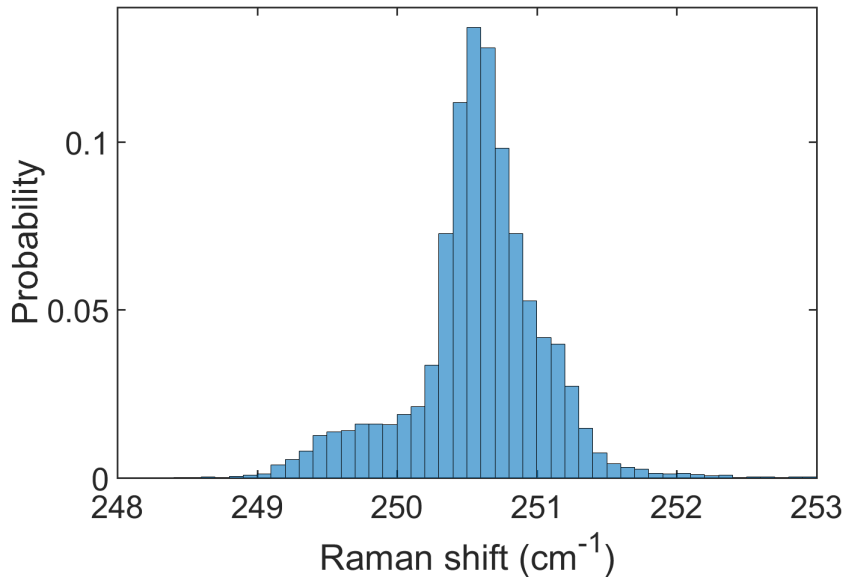


Figure 10.6: Histogram of Raman  $E_{2g}^1$  peak position from monolayer  $WSe_2$

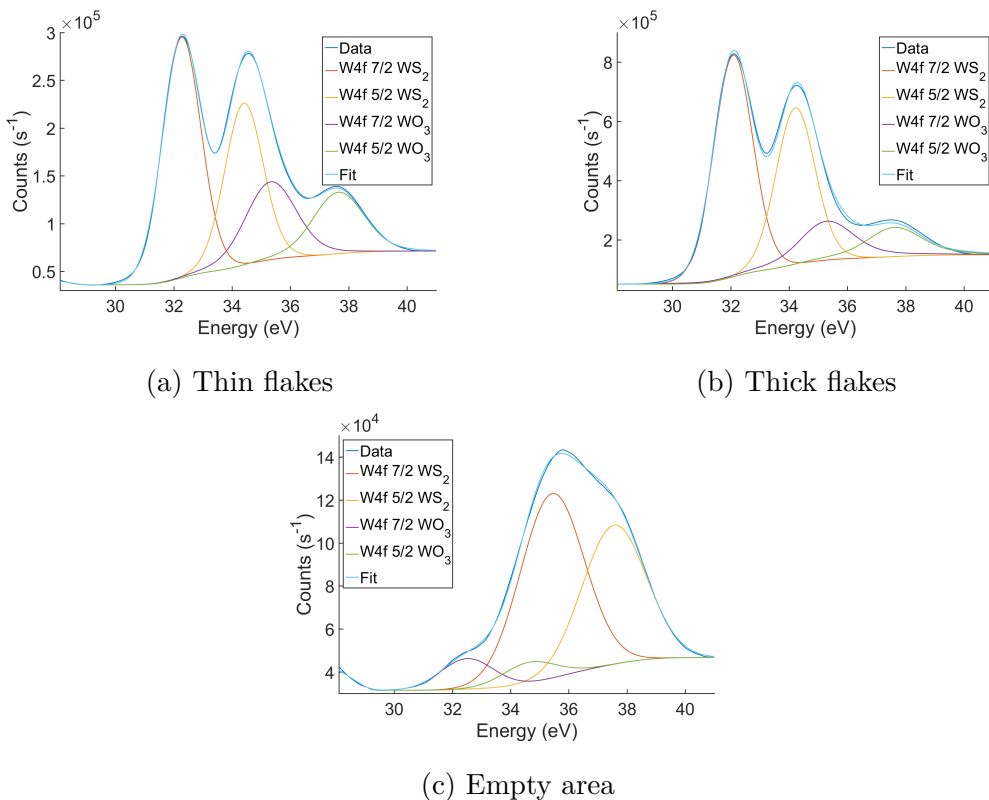


Figure 10.7: XPS spectra of W4f peaks in different areas of the sample

from the thick flake. It is possible that XPS is sensitive to the number of layers in  $WSe_2$  and TMDCs in general since it is known that number of layers does modify the electronic structure of the material. The  $WO_3$  is found to be at the same position in both areas.

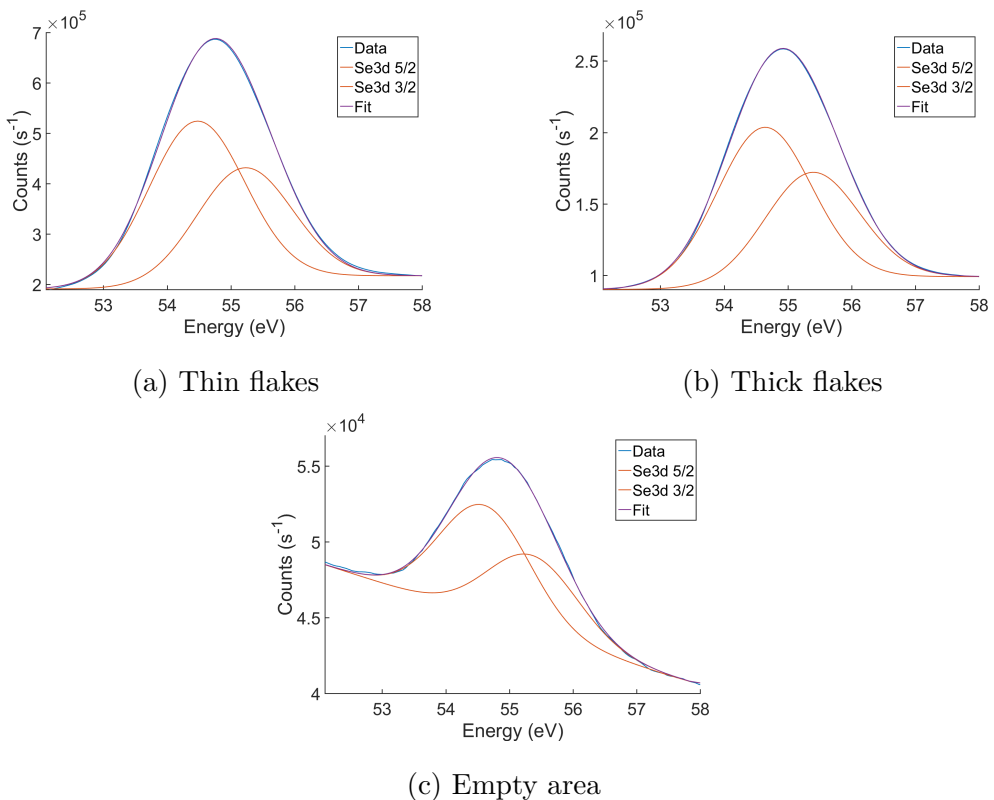


Figure 10.8: XPS spectra of Se3d peaks in different areas of the sample

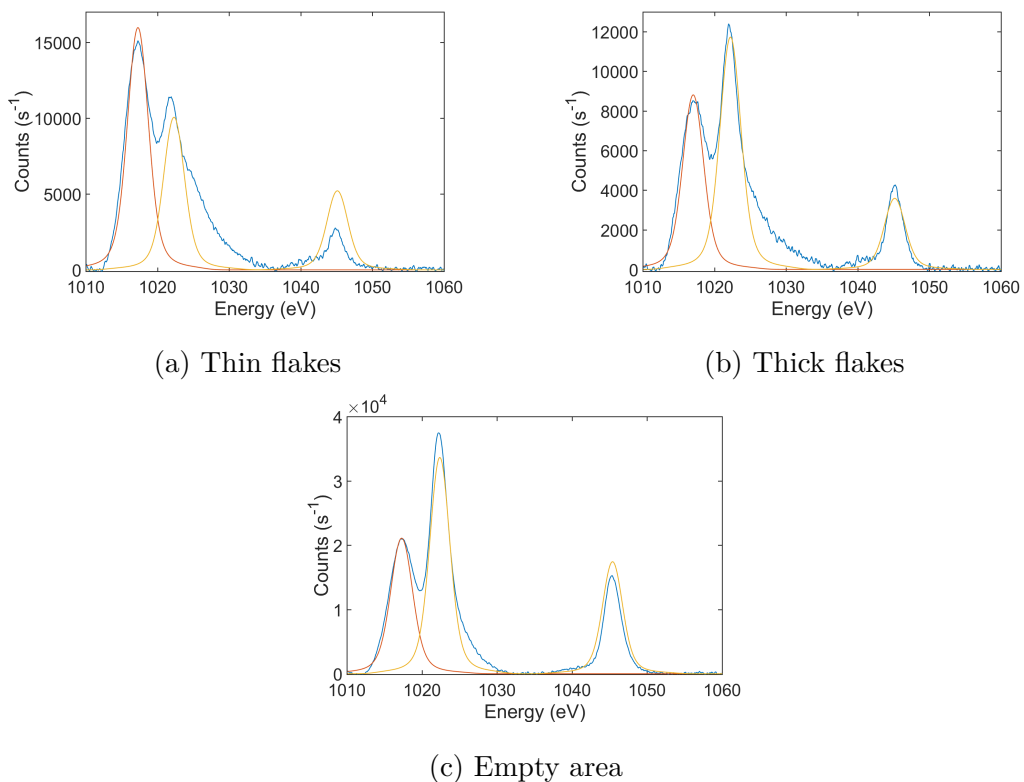


Figure 10.9: XPS spectra of Zn2p peaks in different areas of the sample

The  $WO_3$  peak is also relatively weaker in the area with the thick flake than in the area with thin flake which could be a result of the thick flake having larger surface area than the thin flake and smaller presence of  $WO_3$  around the flake. Additionally an empty area (Figure 10.7c) with no visible flakes has been measured. Similarly two doublets, one at 32.58 eV and 34.73 eV and a second one at 35.48 eV and 37.58 eV have been fitted and their presence can be again explained by presence of  $WSe_2$  and  $WO_3$ . The  $WSe_2$  peak is shifted in relation to that from the thin flake by 0.5 eV which could indicate presence of a highly defective  $WS_2$  or very small amounts of very bulk  $WS_2$ . The  $WS_2$  peak is also much weaker than that of the  $WO_3$  which is expected since there is no visible  $WS_2$ . This result suggesting presence of residues of tungsten oxide species across the whole substrate and thus also possibly across the grown flakes of  $WSe_2$ . This result corroborates the evidence of chemical purity of  $WSe_2$ .

We can also look at Se3d core levels measured at the same locations. As seen in Figure 10.8a, taken from an area with the thin flake, we can fit it with one doublet corresponding to the presence of  $WSe_2$  at 54.48 eV and 55.23 eV. Similarly in Figure 10.8b we can see Se3d peaks taken from area with the thick flake and can fit it with a doublet at 54.63 eV and 55.38 eV which also corresponds to the  $WSe_2$ . Similar to the W4f levels there is a shift of 0.15 eV between those two flakes which can be explained by their thickness which changes the electronic structure. The Se3d levels measured in the reference empty area also can be fitted with a doublet at 54.53 eV and 55.33 eV which can be attributed to  $WSe_2$ . Similarly there is a shift of 0.05 eV from the peak associated with the thin flake, which is much smaller than the W4f peak shift. The Se3d peak from the empty area is about a magnitude weaker than that from either the thin or thick flake which is expected as no visible flake was observed. It does however indicate a non insignificant presence of  $WSe_2$ , perhaps in the form of nuclei that never grew into proper flakes or flakes that shrunk or became etched and are highly defective and thinner than monolayer. The Se3d from the empty area also exhibits a steep background which indicates that the Se is covered with some layer, perhaps that of  $WO_3$ .

Finally the Zn2p levels were measured across the same areas. As seen in Figure 10.9a a doublet can be identified at 1022.02 eV and 1045.11 eV together with a single peak at 1017.33 eV taken from a thin flake. Similarly in Figure 10.9b the doublet is located at 1022.23 eV and 1045.16 eV and a single peak at 1017.03 eV. The reference area shows a doublet at 1045.39 eV and 1022.38 eV and a single peak at 1017.29 eV. It seems therefore that the peak position of the Zn2p doublet does not change significantly from the empty

reference area and the thin or thick flake. The peak intensity in the empty area is also much greater than that of the peak in the area with thin or thick flakes. It suggests then that the Zn that was used in the synthesis is therefore located mostly on a substrate and not on the  $WSe_2$  flakes.

Table 10.1:  $WSe_2$  W 4f and Se 3d peak position dependance on number of layers

	Thin (<3 layers)	Thick (~6 layers)
W 4f7	32.08 eV	32.28 eV
W 4f5	34.23 eV	34.43 eV
Se 3d5	54.48 eV	54.63 eV
Se 3d3	55.23 eV	55.38 eV

As seen in Table 10.1 the peak positions of W 4f and Se 3d taken from  $WSe_2$  thin and thick flakes can be compared. The thick flake can be considered to be equivalent to a bulk form. There is a consistent shift of about 0.2 eV for all of those peaks.

## 10.3 Conclusions

In this chapter I have presented and discussed the electronic band structure and the physical characterization of CVD grown 2H  $WSe_2$ . The CVD synthesis of  $WSe_2$  is quite challenging and not much work has been reported so far in the literature due to the low reactivity of Se. We have concluded that the grown material is pure, and possibly have high crystallinity as demonstrated from the relatively small FWHM of the PL peak. Additionally, thanks to micrometric lateral size resolution of the XPS analysis we could distinguish and parameterise the difference in binding energy of W 4f orbitals as a function of the thickness of the flakes for the first time. Furthermore, we could prove that a small amount of  $WO_3$  is spread all over the substrate and it is not chemically bound to  $WSe_2$ . Similarly, it was interesting to observe the presence of elemental Se on the bare substrates. In contrast with the belief that the sticking coefficient of chalcogen elements is very low as compared to metals such as W and Mo, this evidence can shed light into the growth mechanism via CVD of atomically thin materials.

# Chapter 11

## Physical characterisation of few-layered 1T' $WSe_2$

### 11.1 Introduction

The 1T and 1T' phases of group VI TMDCs have only recently gained significant attention compared to the more popular semiconducting 2H and number of reports in the literature has increased. They have been found to show promise in areas of electrocatalytic water splitting and energy storage thanks to lower charge transfer resistance [172], a result of their metallic nature [173]. The 1T' phase is also predicted to be a large gap quantum spin Hall (QSH) insulator which can be useful in spintronic devices application [174]. In contrast to 1T'  $WTe_2$  [97] it can be used in ambient temperatures as well as ambient atmosphere unlike other known large gap QSH insulator materials like stanene [175] or 2D In-Sb compounds [176].

So far the synthesis of 1T and 1T' group VI sulfides and selenides ( $MoS_2$ ,  $WS_2$ ,  $MoSe_2$ ,  $WSe_2$ ) phases has proven difficult due to the metastable nature of them. Most commonly a direct synthesis via e.g. a CVD route results in more thermodynamically stable 2H phase. The difference in energy per formula unit between 1H and 1T'  $WSe_2$  phase is only 0.27 eV which suggests that under certain reaction conditions a metastable 1T' can be synthesised.

The  $WSe_2$  flakes of varying thickness has been successfully grown via the colloidal synthesis method.

## 11.2 Results

In order to ascertain the phase of the as grown  $WSe_2$  a Raman spectrum has been taken. As seen in Figure 11.1 the spectrum of the as grown 1T'  $WSe_2$  looks very different to the Raman spectrum of the CVD grown 2H  $WSe_2$  as seen in e.g. Figure 10.2b. The  $E_{2g}^1$  and  $A_{1g}$  located around  $250\text{ cm}^{-1}$  and are convoluted in case of the monolayer. In spectrum of the 1T' sample (Figure 11.1) the closest peaks to those are located at  $248.6$  and  $260\text{ cm}^{-1}$  and can be therefore ascribed to  $E_{2g}^1$  and  $A_{1g}$  modes respectively. Additionally the absence of the  $B_{2g}^1$  peak suggest that the material is very thin. Furthermore there are 5 more unresolved peaks at  $104.5$ ,  $149$ ,  $177$ ,  $218$  and  $236.3\text{ cm}^{-1}$ . Thus far there is no published information regarding the vibrational modes of 1T'  $WSe_2$  and therefore the peaks cannot be assigned to the modes. Similarly new peaks have been reported for 1T'  $MoS_2$  where new peaks were labelled as  $J_1$ ,  $J_2$  and  $J_3$  [177].

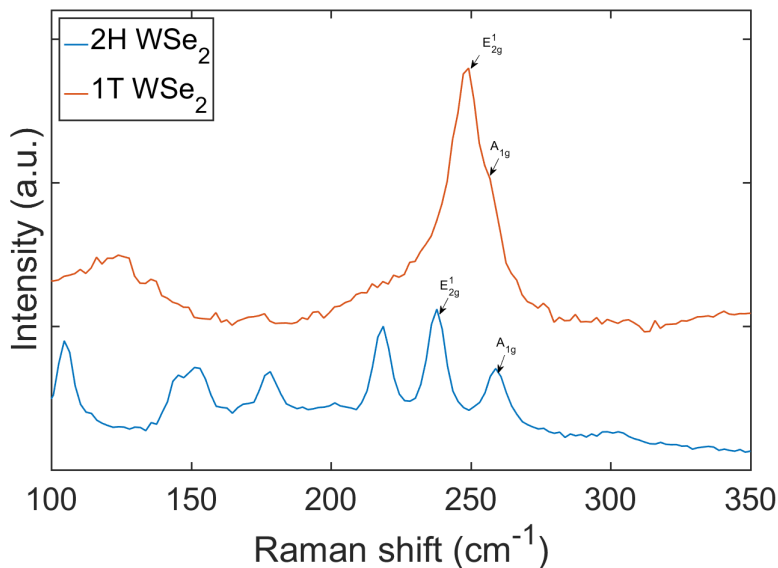
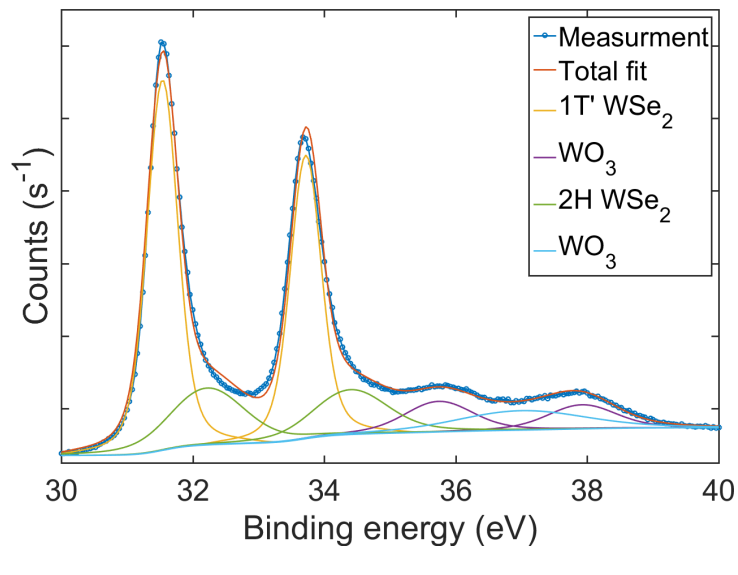


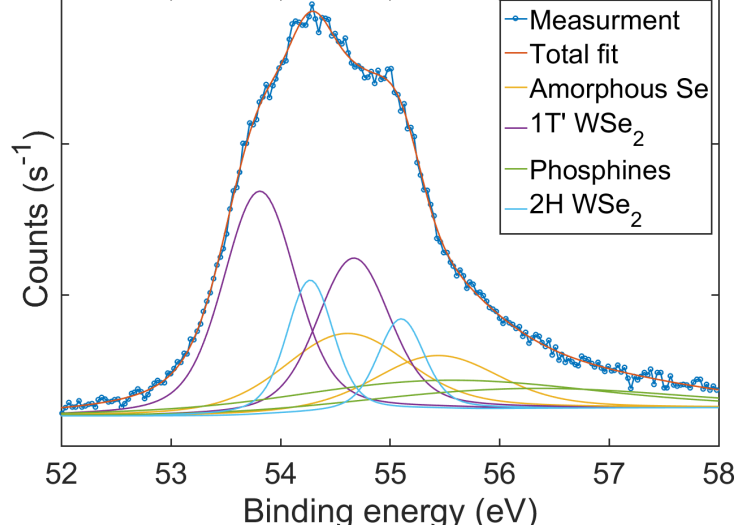
Figure 11.1: Raman spectra of 2H  $WSe_2$  and 1T'  $WSe_2$

Similarly, the XPS spectra were taken of the as-grown sample as seen in Figure 11.2a and Figure 11.2b. The XPS spectrum of the W 4f electron shell shows a doublet of  $W^{+4}$  4f at  $31.49$  and  $33.63\text{ eV}$ . This position varies notably from those reported for 2H  $WSe_2$  and therefore are attributed to 1T'  $WSe_2$ . The shift itself is most likely caused by change in coordination of the metal atom or a change in the W-Se bond length from  $2.531\text{ \AA}$  to  $2.66\text{ \AA}$ . On top of the 1T' phase of  $WSe_2$  additional small contributions to the spectrum can be attributed to the 2H  $WSe_2$  at  $32.22\text{ eV}$  and  $34.30\text{ eV}$ . Additionally an even smaller contribution from tungsten oxides can be identified at  $35.74\text{ eV}$  and  $37.92\text{ eV}$ . The Se

3d level spectrum seen in Figure 11.2b of the as-grown sample has been fitted with 4 doublets. Two of those doublets are associated with  $Se^{-2}$  atoms and are assigned to 1T'  $WSe_2$  (53.60 eV and 54.46 eV) and 2H  $WSe_2$  (54.26 eV and 55.1 eV). The remaining two doublets, with much lower integrated area as compared to the Se bound to W, are assigned to amorphous Se (54.62 eV and 55.46 eV) and Se partially coordinated with phosphines (55.49 eV and 56.36 eV). The latter is remaining from the unreacted precursors of Se for the colloidal synthesis and a small component of amorphous Se is excepted as residual from the synthesis as well.

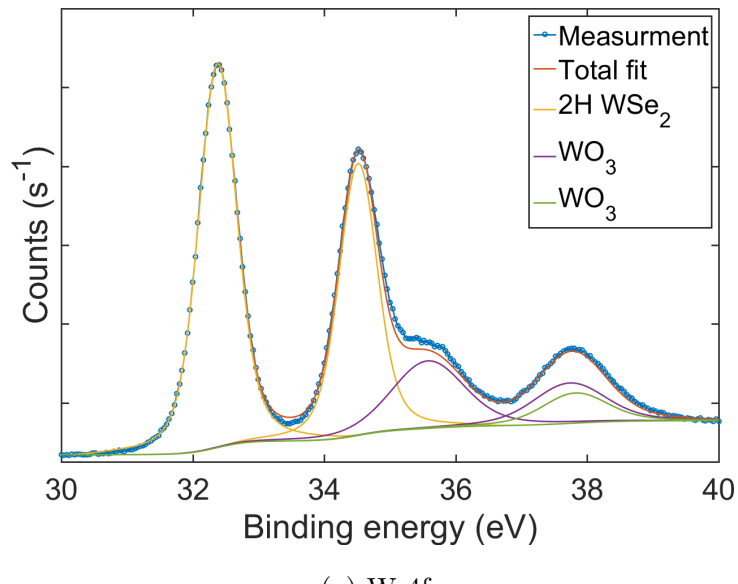


(a) W 4f

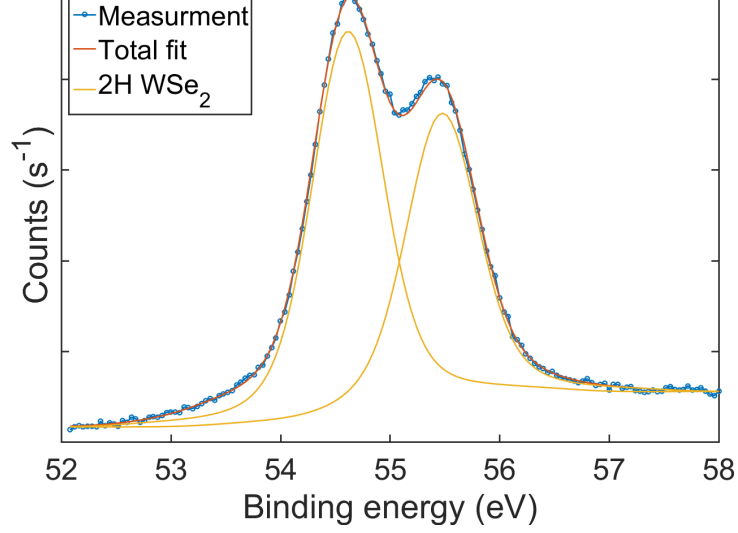


(b) Se 3d

Figure 11.2: XPS spectra of W 4f and Se 3d levels in as grown sample of  $WSe_2$



(a) W 4f



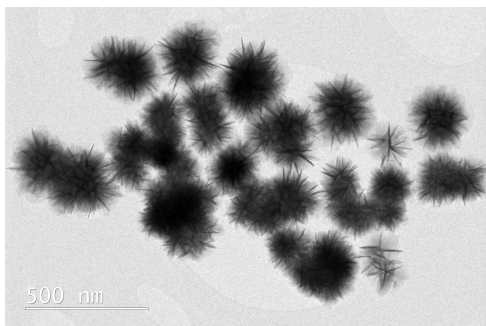
(b) Se 3d

Figure 11.3: XPS spectra of W 4f and Se 3d levels in the annealed sample of *WSe<sub>2</sub>*

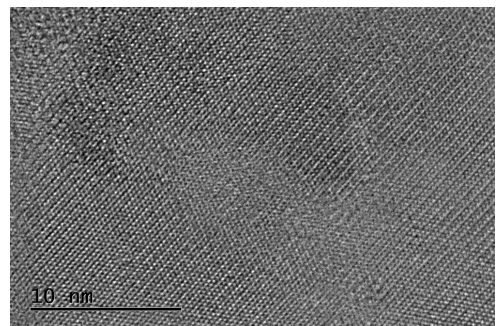
The as-grown sample was then annealed at 400 °C in an argon atmosphere. The Raman spectrum of the annealed sample can be seen in Figure 11.1. The previously unidentified peaks are no longer present except for the two convoluted peaks at around  $250\text{ cm}^{-1}$ . This is indicative of 2H *WSe<sub>2</sub>* and suggests that the entirety of the 1T' phase has been converted to the 2H phase. Additionally the XPS spectra of the annealed sample can be seen in Figure 11.3. The presence of 4f  $\text{W}^{4+}$  peaks 32.40 eV and 34.58 eV and an almost complete absence of the 1T' 4f *WSe<sub>2</sub>* indicates that the sample is primarily a 2H *WSe<sub>2</sub>*. It is worth noting that after annealing the oxidized component of W just

increases by a negligible amount. Following the annealing the XPS spectrum of the Se 3d can be seen in Figure 11.3b. The spectrum can be fitted with one doublet associated with 2H  $WSe_2$  only. This indicates that any residues of unreacted Se can be removed by annealing as expected as the evaporation temperature of elemental Se is  $\sim 270$  °C.

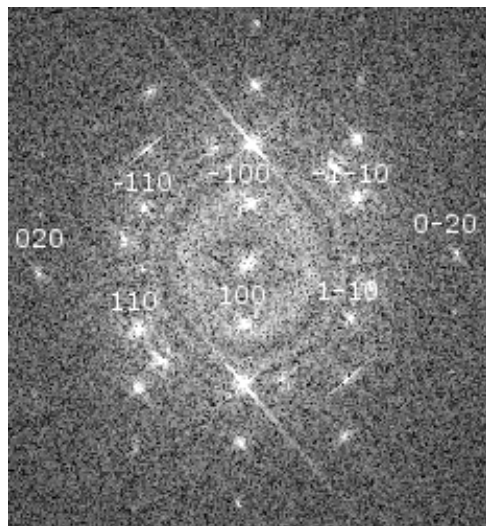
The sample was also characterised using TEM as seen in Figure 11.4. The TEM images show well defined flower shaped nanostructures with the average diameter of 200 nm. The petals stem from the central point and thin down towards the edges down to single layer. The single petals appear to be of 1T' phase while each petal is a single crystal. Additionally the structural parameters  $a = 5.76$  Å and  $b = 3.30$  Å have been identified. Reciprocal lattice created by FFT from high resolution TEM image from a single petal is rectangular and corresponding to monoclinic phase of  $WSe_2$ .



(a) TEM image of as grown 1T'  $WSe_2$  flakes.



(b) High resolution TEM image.



(c) FFT pattern constructed from the image in b).

Figure 11.4: TEM characterisation of as grown 1T' flakes.

In order to investigate the samples electronic properties the Kelvin probe force microscopy

(KPFM) as seen in Figure 11.5. The work function of the 2H and 1T' phase was calculated using the known values of work function for p-doped Si. The values were found to be 2.6 eV and 4.2 eV respectively and they were found to be in good agreement with the values of the 2H (4.08 eV) and 1T' (2.36 eV) produced by potassium surface functionalisation [178].

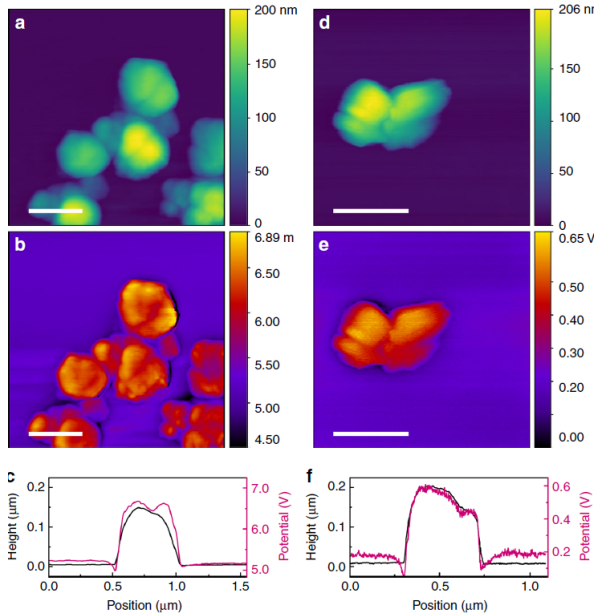


Figure 11.5: a) AFM image using tapping mode b) KPFM image c) black - height profile, purple- contact potential difference variation taken from 1T'  $WSe_2$  flakes deposited on a p-doped Si substrate d) AFM image using tapping mode, e) KPFM image f) same as c) for 2H  $WSe_2$  flakes. Scale bars: 500 nm. Adopted from [179].

### 11.3 Conclusions

In this chapter we have shown how the 1T'  $WSe_2$  has been grown for the first time. The material has then been characterised using Raman spectroscopy, XPS, TEM, and KPFM to ascertain to be in the 1T' crystal phase and to demonstrate to be metallic. Following an annealing at 400 °C the 1T' phase has been almost entirely converted to 2H. We have ascertain the presence of the 2H phase by preforming Raman spectroscopy, XPS, TEM, and characterization. This growth method therefore allows for direct deposition of metastable phase on a functional substrate. Our Raman and XPS characterization of the 1T' phase represent a reference in the literature for future synthesis of 1T' phases of TMDCs.

# Chapter 12

## CVD few-layered MoS<sub>2</sub>/WS<sub>2</sub> Heterostructures

### 12.1 Introduction

One of the potential applications of the TMDC heterostructures is as photocatalyst for water-splitting reaction. The dimensionally confined materials, such as TMDCs offer many advantages in comparison to more commonly used materials. The large surface to volume ratio allows many catalytically active sites, generally higher carrier mobility and tunable bandgap of many of the TMDCs makes them suitable for efficient absorption of sunlight. Most commonly studied TMDCs, *MoS*<sub>2</sub> and *WS*<sub>2</sub> exhibit valence band edge more positive than the oxidation potential of water (1.23 eV) and can therefore act as a photoanode.

While a single material like *MoS*<sub>2</sub> or *WS*<sub>2</sub> can be used alone as a photocatalyst by forming a type II heterojunction additional benefits can be exploited [180][181]. The presence of the heterojunction allows for holes to migrate to *WS*<sub>2</sub> valence band while electrons move to *MoS*<sub>2</sub> conduction band. As a result the physical charge separation delays the exciton recombination and allows for efficient water splitting.

Commonly a liquid phase exfoliation (LPE) has been used to deposit TMDC layers on conductive substrates like gold. However this method results in highly defective material with small flakes and solvent residue adsorbed to the basal plane [182][183][184]. In contrast the other commonly used technique of CVD has been utilised primarily to grow TMDC layers on top of resistive substrates like *SiO*<sub>2</sub>/*Si* [136]. It has also been shown that CVD can produce an epitaxial interface in heterostructure and as a result reduce

trap states [185]. In order to increase the size of the flakes as well as reduce the number of defects the heterostructures were grown by CVD onto gold substrate to allow for direct application as a photocatalyst.

Such grown material can potentially result in both vertical as well as lateral heterostructures as well as alloys. In order to effectively resolve those Raman, PL spectroscopy and XPS were employed to assess the quality of the as grown heterostructures.

The CVD growth setup can be seen in Figure 12.1. The CVD growth was performed using recipes developed in previous work on CVD of monolayers of  $WS_2$  and  $MoS_2$  [136]. Since the high mobility is of upmost importance for the photoelectrocatalytic performance [186] this growth method is particularly useful. As seen in Figure 12.2 the CVD growth on Au substrate may result additionally in formation of vertical flakes [187].

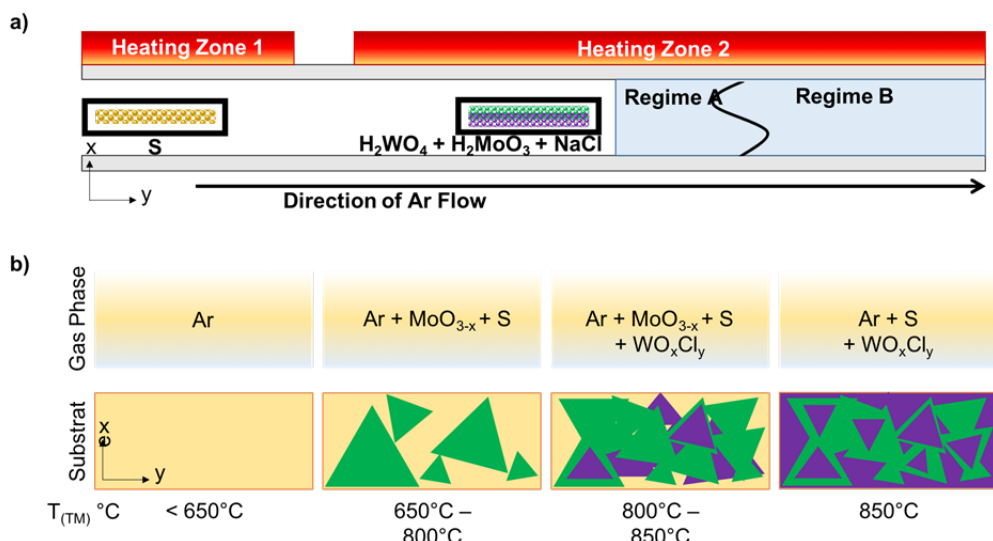


Figure 12.1: CVD furnace setup a) spatial distribution of precursors b) simplified representation of the growth result (green = Mo region; purple = W region).

It is especially easy to achieve vertical growth on Au substrate due to high capture rate of sulphur at the nucleation stage [131]. This results in good adhesion of the flakes parallel to the surface and high surface area caused by the vertical growths. Relatively big flakes can still be grown using this procedure (Figure 12.2).

## 12.2 Results

A  $WS_2/MoS_2$  heterostructure has been prepared by one step growth CVD. As a first step the heterostructure has been grown on  $SiO_2/Si$  using parameters developed for monolayer

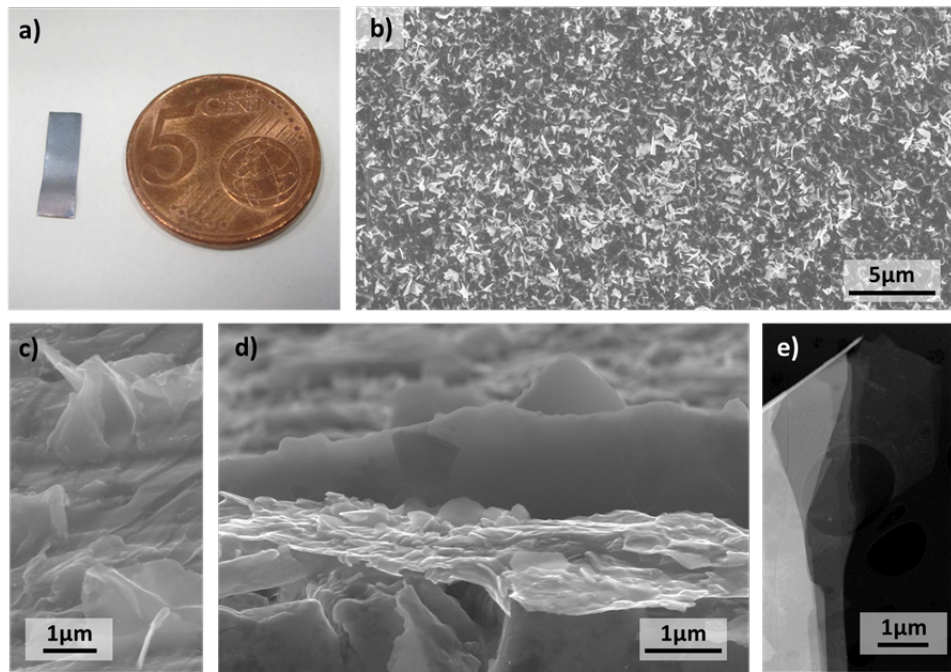


Figure 12.2: a)  $MoS_2/WS_2$  heterostructure on Au substrate b) SEM image of  $MoS_2/WS_2$  heterostructures on Au substrate c) side; d) cross-sectional SEM image e) STEM image of the flake edge. Adopted from [188].

growth. An optical micrograph of a select area of the sample can be seen in Figure 12.3. The sample contains large areas of monolayer and bilayer TMDCs with some very small flake of bulk material. Overall the material coverage is quite high.

The sample was then characterised using Raman and PL spectroscopy. A measurement of Raman spectrum was taken from heterostructure and as seen in Figure 12.4 a distinct spectrum of  $WS_2$  and  $MoS_2$  can be distinguished. The Raman peak positions are  $350.1\text{ }cm^{-1}$ ,  $382\text{ }cm^{-1}$ ,  $408.3\text{ }cm^{-1}$  and  $417.7\text{ }cm^{-1}$  which can be ascribed to  $WS_2\text{ }E_{2g}^1$ ,  $MoS_2\text{ }E_{2g}^1$ ,  $MoS_2\text{ }A_{1g}$  and  $WS_2\text{ }A_{1g}$  respectively. Those peak positions correspond to multi layers of the individual materials which indicates a certain level of interaction between the layers.

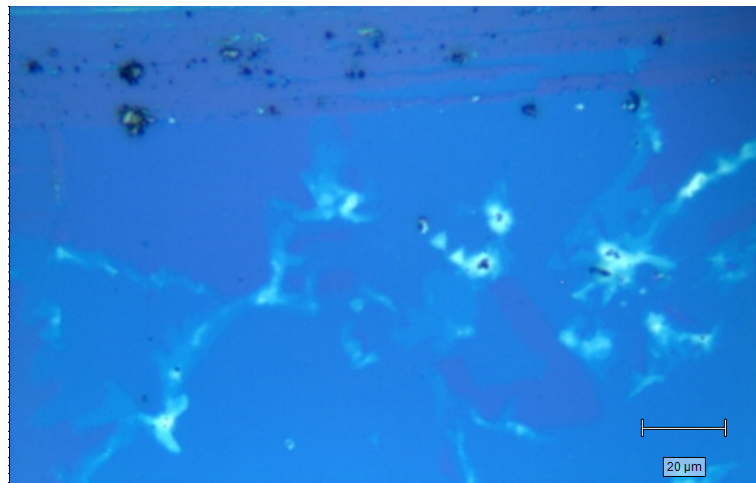


Figure 12.3: Optical micrograph of  $WS_2/MoS_2$  heterostructure on  $SiO_2/Si$

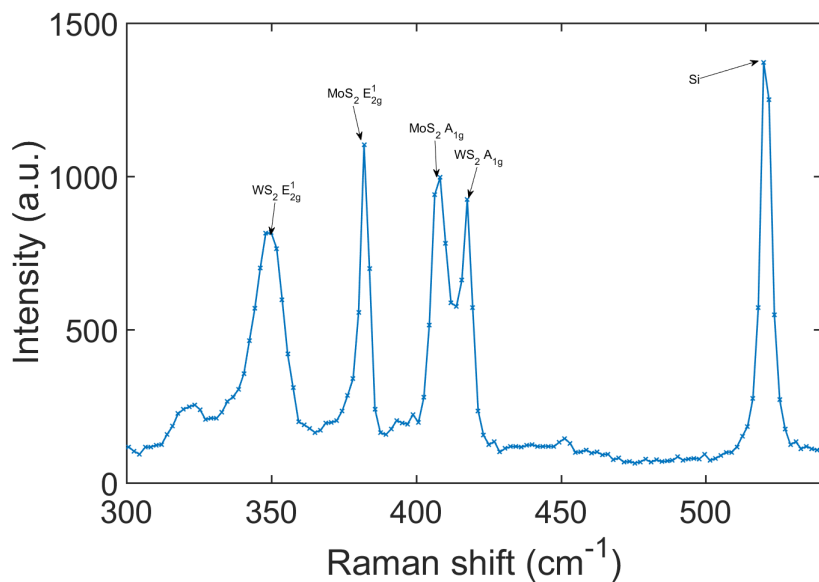


Figure 12.4: Raman spectrum of  $WS_2/MoS_2$  heterostructure

There is a monolayer and bilayer  $MoS_2$  found around the heterostructure area with no  $WS_2$  grown indicating that the  $WS_2$  flake has grown on top of the  $MoS_2$  layer. The area surrounding the heterostructure shows a spectrum as seen in Figure 12.5.

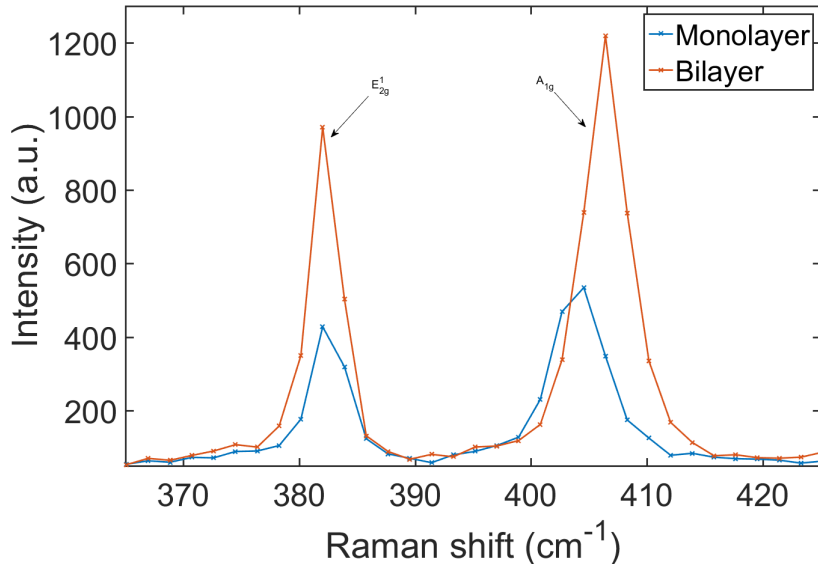


Figure 12.5: Raman spectra of mono and bilayer  $MoS_2$

The positions of the peaks are  $382.7\text{ }cm^{-1}$  and  $404\text{ }cm^{-1}$  for the monolayer and  $382.4\text{ }cm^{-1}$  and  $406.4\text{ }cm^{-1}$  for the bilayer.

It has been shown that in  $WMoSe_2$  alloy as more of the alloying metal is added the characteristic Raman peaks ( $E_{2g}^1$  and  $A_{1g}$ ) of the primary structure become less intense and shifted [10]. Due to presence of both  $WS_2$  and  $MoS_2$  characteristic peaks at relatively high intensity as well as lack of significant shift in the observed peak position it can be concluded that the sample is not a complete alloy. It is possible that each of the monolayer in the heterostructure is alloyed to a small degree but further studies are necessary to properly quantify these results.

The sample was then mapped using Raman spectroscopy. As seen in Figure 12.6 the intensity of  $E_{2g}^1$  peak varies across the mapped area for both  $WS_2$  and  $MoS_2$ . The more intense areas indicate more layers of  $WS_2$  which is placed on top of  $MoS_2$ . Where the intensity of  $WS_2$   $E_{2g}^1$  peak is higher and therefore there is more layers of  $WS_2$  the intensity of  $MoS_2$   $E_{2g}^1$  is reduced.

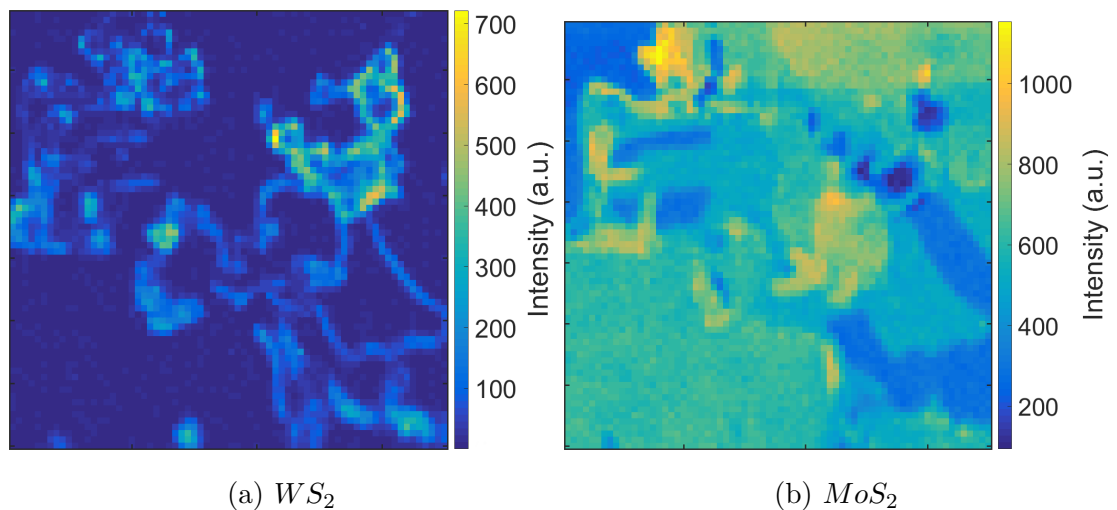


Figure 12.6: Map of Raman  $E_{2g}^1$  peak intensity

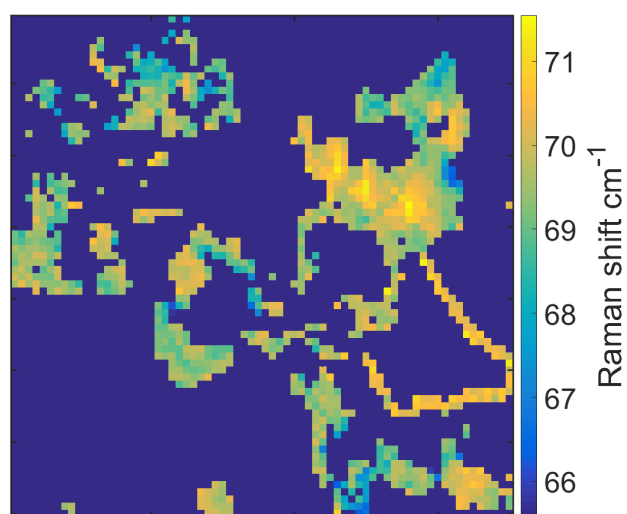


Figure 12.7: Difference between  $WS_2$   $A_{1g}$  and  $E_{2g}^1$  peak position

To better estimate the number of layers the difference between  $A_{1g}$  and  $E_{2g}^1$  peak positions has been also calculated. By excluding the bulk flakes and leaving the flakes with less or equal to 3 layers of  $WS_2$  it can be estimated that about 25% of the area is covered with  $WS_2/MoS_2$  heterostructure.

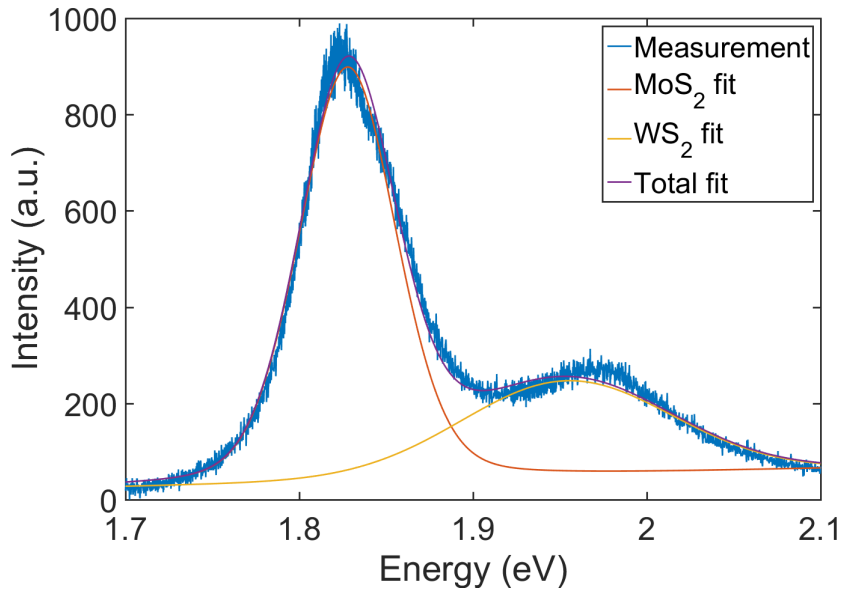


Figure 12.8: PL spectrum of  $MoS_2/WS_2$  heterostructure

The PL spectrum of heterostructure can be seen in Figure 12.8. There are two distinct peaks, one at 1.824 eV and second at 1.971 eV. The position of the  $MoS_2$  PL peak is consistent with the position of the monolayer  $MoS_2$  as seen in Figure 12.9 which is 1.825 eV. Those PL peaks from heterostructure therefore correspond to both  $MoS_2$  and  $WS_2$  monolayers indicating that the spectrum is additive. The  $MoS_2$  peak is also much stronger than  $WS_2$  despite the fact that isolated monolayer of  $WS_2$  shows much stronger PL than a monolayer of  $MoS_2$ . The  $MoS_2$  peak has a FWHM of 65.47 meV while the  $WS_2$  PL peak has a FWHM of 142.4 meV.

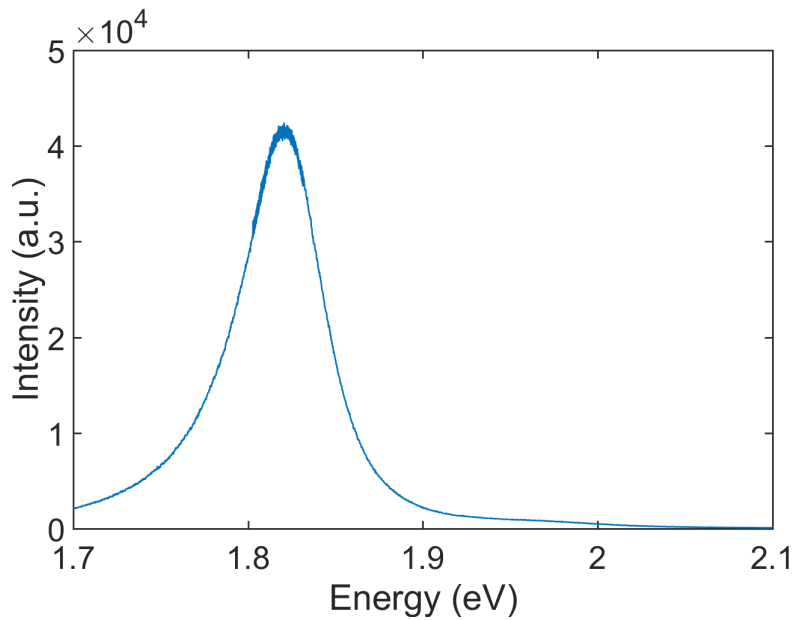


Figure 12.9: PL spectrum of  $MoS_2$  monolayer

The sample was also mapped using PL spectroscopy as seen in Figure 12.10. The most intense PL can be observed in areas of monolayer  $MoS_2$  and much weaker everywhere else. The position map of PL peaks from both  $MoS_2$  and  $WS_2$  can be seen further in Figure 12.11. Most of the PL of  $MoS_2$  is centred around 1.82 eV with smaller part ( $\sim 8\%$ ) centred around 1.802 eV. It seems therefore that majority of the  $MoS_2$  is a monolayer  $MoS_2$  while the PL peaks at 1.802 eV indicate a  $MoS_2$  bilayer. The  $WS_2$  PL position map reveals most of the PL peaks centred around 1.965 eV and smaller part ( $\sim 16\%$ ) centred around 1.935 eV. Similarly to  $MoS_2$  the majority of the  $WS_2$  is therefore monolayer with small part of it being bilayer  $WS_2$ .

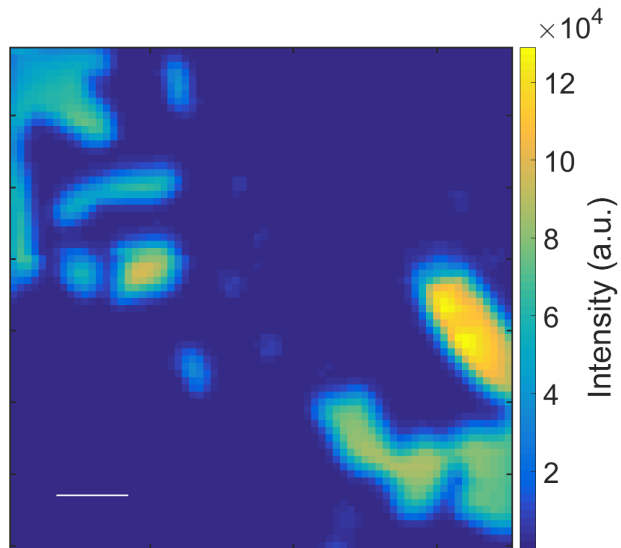


Figure 12.10: Integrated PL intensity map. Scalebar is  $10\mu m$ .

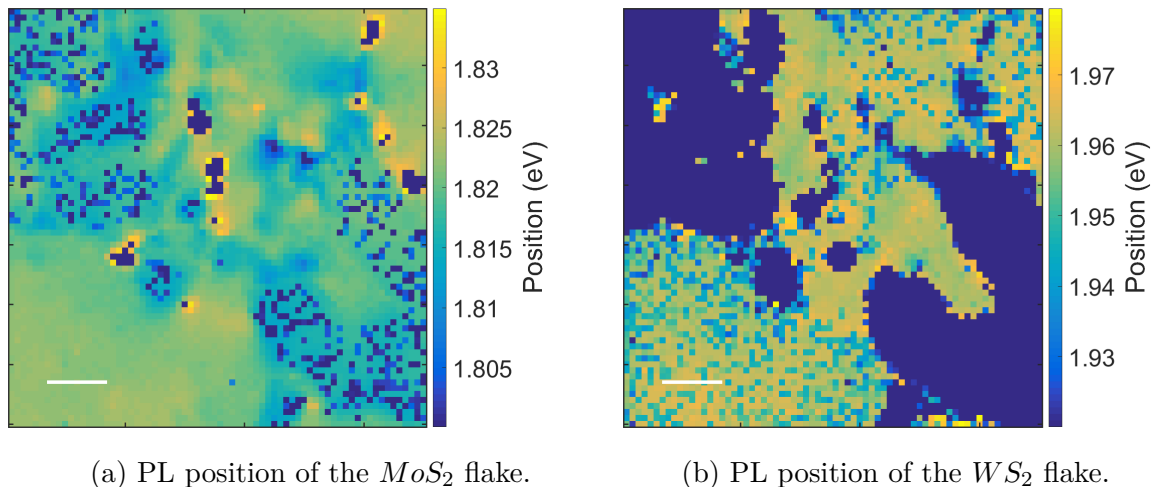


Figure 12.11: Map of PL peak positions. Scalebar is  $10\mu m$ .

The similar growth procedure was then used to grow  $WS_2/MoS_2$  heterostructure on a gold substrate. As seen in Figure 12.12 the material coverage of the substrate is complete. The material also seems to be thick with irregular, rough surface. There are no visible triangles or continuous layers like seen in a  $SiO_2/Si$  substrate. This is most likely due to vertical growth which can occur on gold substrate as opposed to  $SiO_2/Si$  substrate.

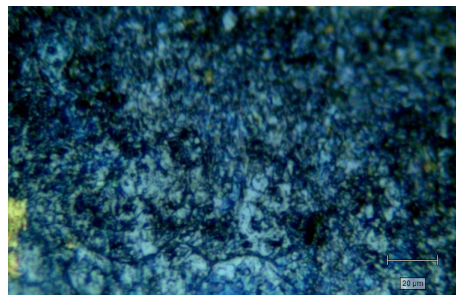


Figure 12.12: Optical micrograph of the  $WS_2/MoS_2$  on Au substrate

The sample was then mapped using Raman spectroscopy. As seen in Figure 12.13 the  $WS_2$  and  $MoS_2$  Raman peaks  $E_{2g}^1$  and  $A_{1g}$  can be identified.

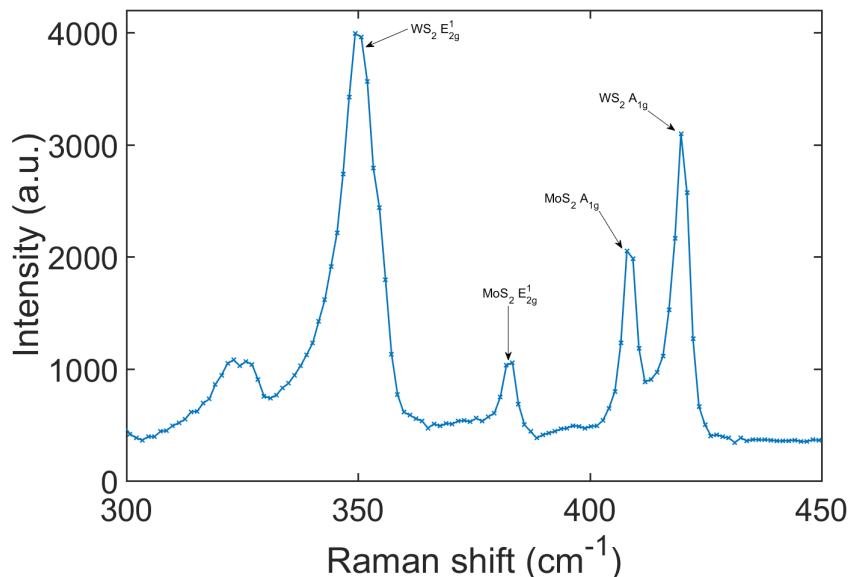


Figure 12.13: Raman spectrum of  $WS_2/MoS_2$  on Au substrate

As seen in Figure 12.14 the  $MoS_2 E_{2g}^1$  can be seen across the entire scanned area. On the other the  $WS_2 E_{2g}^1$  peak can be seen less spread around. Additionally the areas with high intensity  $WS_2 E_{2g}^1$  coincide with low intensity  $MoS_2 E_{2g}^1$ . It implies therefore that similarly to the  $SiO_2/Si$  substrate the  $WS_2$  grows on top of the  $MoS_2$  which results in a weaker Raman signal from  $MoS_2$  from areas where thick  $WS_2$  has grown on top of the underlying  $MoS_2$ .

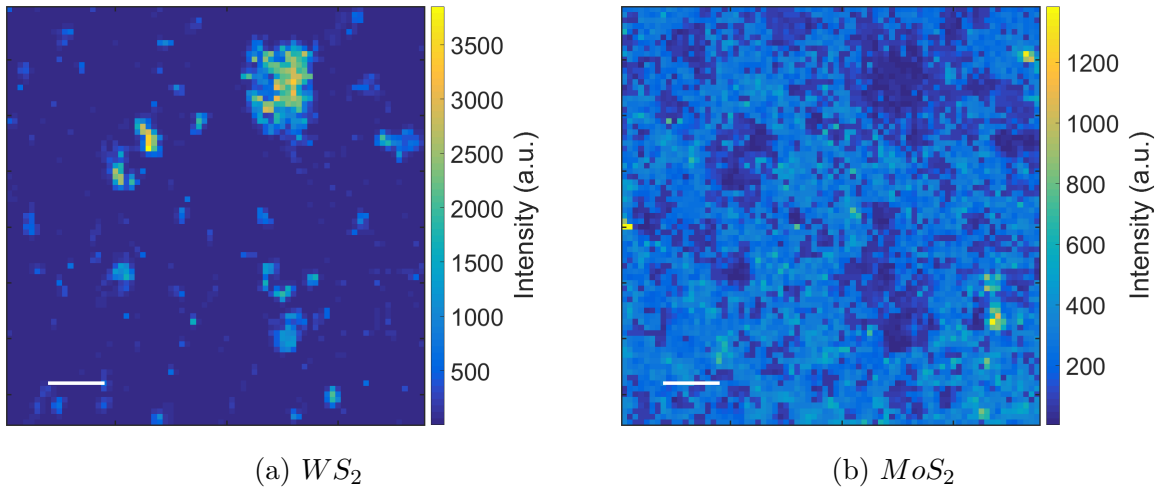


Figure 12.14: Raman  $E_{2g}^1$  intensity maps. Scalebar is  $10\mu m$ .

The peaks positions for  $WS_2$  are on average  $349.1\text{ }cm^{-1}$  and  $418.5\text{ }cm^{-1}$  for  $E_{2g}^1$  and  $A_{1g}$  respectively. Similarly for  $MoS_2$  the peaks positions are  $382.5\text{ }cm^{-1}$  and  $408.6\text{ }cm^{-1}$  for  $E_{2g}^1$  and  $A_{1g}$  respectively. This indicates that both  $MoS_2$  and  $WS_2$  are mostly few layers thick. It can be estimated that in the measured area the  $WS_2$  coverage and therefore the  $WS_2/MoS_2$  heterostructure presence is at least 8%.

Due to the gold substrate the PL is partially quenched which combined with weak PL signal coming from few layer  $WS_2$  and  $MoS_2$  makes it difficult to make any meaningful measurement.

Compared to previously reported work on TMDCs, the performance in both hydrogen evolution ( $\sim 0.1\%$  IPCE) and water oxidation ( $\sim 0.1\%$  IPCE) is improved [129]. Further data and analysis of the photoelectrocatalytical performance of this heterostructure has been reported in [188].

## 12.3 Conclusion

The  $MoS_2/WS_2$  heterostructure has successfully been grown on  $SiO_2/Si$  as well Au substrates. Their structure has been then successfully assessed with the help of PL and Raman spectroscopy. Raman and PL maps revealed that at least 8% of the investigated areas has been covered in heterostructures. Their performance as an photoelectrocatalyst for water oxydation and hydrogen evolution has been further evaluated and found to be superior to the previously reported values. Overall those promising results warrant further research and development of one step growth to achieve better heterostructure coverage

and performance.

# Chapter 13

## Conclusions and future work

We have shown that the CVD synthesis of  $WS_2$  using novel precursors can result in formation of high quality atomically thin flakes at low temperatures up to hundreds of  $\mu m$  in size. In particular this method proves to result in better flakes in essentially every way in comparison to more common oxide precursor like  $WO_3$ . A very narrow PL of 36 meV and record high room temperature electron mobility of  $52\text{ cm}^2/V\text{s}$  proves quality that exceeds even a naturally occurring  $WS_2$ . The used precursors also avoids the problems of commonly used oxy-carbon based precursors of  $W$  in that it does not contaminate the synthesis products and does not produce toxic by products. It has also been shown that Raman spectroscopy and PL spectroscopy can be used as a reliable tool to map the as-grown samples and easily extract properties of the material. The insights brought about through those characterisations can prove to be useful moving forward and applying them to a host of other TMDC materials and systems. Additionally the synthesis routes and the precursors developed here can prove useful for fabrication of high-quality large-scale low-cost flakes in future. Similarly the presented precursors and synthesis method can be expanded to other TMDCs such  $MoS_2$ ,  $WSe_2$  or  $MoSe_2$  to produce material of quality higher than has been otherwise reported in literature.

The synthesis method developed for  $WS_2$  has been then applied to produce  $WSe_2$  flakes. By utilising the tungstic acid ( $H_2WO_4$ ) and  $Se$  powders a similar low temperature synthesis resulted in flakes of up to  $30\text{ }\mu m$  in size. Similarly the PL and Raman spectroscopy has been utilised to characterise the samples and a strong PL with FWHM of about 66 meV in monolayer  $WSe_2$  has been demonstrated. The XPS studies show presence of  $WO_3$  in the as-grown sample which indicates that the synthesis method for  $WSe_2$  needs to be further refined to produce high quality flakes, the likes of which has

been demonstrated for  $WS_2$ . In principle it has been shown that the method developed for  $WS_2$  is transferable and can be further utilised in production in a number of other TMDC materials.

The transfer of TMDC flakes as well as flakes of other 2D materials can prove to be a crucial element in a production route of any future device utilising these materials. We have therefore studied the effects of transferring as grown  $WS_2$  flakes from one  $SiO_2/Si$  substrate onto another  $SiO_2/Si$  substrate to asses the quality of the transferred material and therefore the impact of the transfer. One of the most commonly used methods of wet transfer utilising PMMA has proven to alter the distribution of PL and Raman peaks across the samples. One of the most common effect cited in literature regarding the transfer is that of strain relaxation that can build up during CVD growth due to the high temperatures during the synthesis. Based on our experiments it cannot however be definitively concluded whether the transfer reduces or induces strain in the sample as a whole. There has been however demonstrated potential change in distribution of strain across the sample which manifests itself in shifts in PL peak positions as well as Raman peak positions. Any transfer attempts must therefore be considered carefully and preferably a different, more reliable transfer method be used.

In order to further study the PL behaviour in  $WS_2$  flakes a low temperature studies were performed. It has been demonstrated that low pressure induces changes in PL behaviour due to desorption of  $O_2$ ,  $H_2O$  and  $N_2$  molecules which otherwise result in p-doping. The exciton peak with FWHM of 32 meV has been observed which is higher than expected assuming the temperature is a main contributor to the width of the room temperature PL peak of 36 meV. A number of possible effects, such as sample heating due to poor thermal contacts or fogging of the chamber window can be attributed to the resulting width. Additionally a trion peak has been clearly resolved with binding energy to be about 45 meV.

By using same synthesis method vertical heterostructures of  $Mo_2/WS_2$  have been grown. A single step, one pot growth has been achieved with a degree of tunability. The resulting heterostructure has been shown to be more closely packed than a material produced more commonly via a mechanical transfer. This results in a greater degree of interaction between the layers which in turn manifests itself in both PL and Raman spectroscopy. The growth has then been also performed on a conducting substrate, such as gold. This allows such prepared heterostructure to be readily available as a photoelectrocatalyst for a reaction of water-splitting. Using developed understanding of Raman

and PL spectroscopy it has been shown that at least 8% of the surface has been covered with heterostructures which leaves room for improvement and further refinement of the synthesis.

The developed synthesis methods as well as the characterisation understanding of the as grown samples can form a basis for further improvement of the performance of those materials. One of the promising approaches to enhancing the opto-electronic performance of devices is the use of plasmonic nanoparticles. These nanoparticles have been shown to enhance local electromagnetic field of incident light as well as reflect it to improve the absorption rate of light. This can therefore find application in solar cells or photoelectrocatalysis as presented in our work, the latter of which has not been presented yet.

Additionally further characterisation of the 1T'/2H systems is necessary to evaluate the stability. In particular synthesis of and systematic Raman mapping of large areas could prove useful in understanding these phases.

# Bibliography

- [1] Q. H. Wang, K. Kalantar-Zadeh, A. Kis, J. N. Coleman, and M. S. Strano, “Electronics and optoelectronics of two-dimensional transition metal dichalcogenides,” *Nature Nanotechnology*, vol. 7, pp. 699–712, Nov 2012. Review Article.
- [2] A. Kuc, N. Zibouche, and T. Heine, “Influence of quantum confinement on the electronic structure of the transition metal sulfide TS<sub>2</sub>,” *Physical Review B*, vol. 83, p. 245213, jun 2011.
- [3] A. Splendiani, L. Sun, Y. Zhang, T. Li, J. Kim, C.-Y. Chim, G. Galli, and F. Wang, “Emerging photoluminescence in monolayer MoS<sub>2</sub>,” *Nano Letters*, vol. 10, pp. 1271–1275, apr 2010. PMID: 20229981.
- [4] H. R. Gutiérrez, N. Perea-López, A. L. Elías, A. Berkdemir, B. Wang, R. Lv, F. López-Urías, V. H. Crespi, H. Terrones, and M. Terrones, “Extraordinary room-temperature photoluminescence in triangular WS<sub>2</sub> monolayers,” *Nano Letters*, vol. 13, pp. 3447–3454, dec 2012. PMID: 23194096.
- [5] M. Bernardi, M. Palummo, and J. C. Grossman, “Extraordinary sunlight absorption and one nanometer thick photovoltaics using two-dimensional monolayer materials,” *Nano Letters*, vol. 13, pp. 3664–3670, jul 2013.
- [6] Z. Ye, T. Cao, K. O’Brien, H. Zhu, X. Yin, Y. Wang, S. G. Louie, and X. Zhang, “Probing excitonic dark states in single-layer tungsten disulphide,” *Nature*, vol. 513, pp. 214–218, aug 2014.
- [7] M. Currie, A. T. Hanbicki, G. Kioglou, and B. T. Jonker, “Optical control of charged exciton states in tungsten disulfide,” *Applied Physics Letters*, vol. 106, p. 201907, may 2015.
- [8] H. Nan, Z. Wang, W. Wang, Z. Liang, Y. Lu, Q. Chen, D. He, P. Tan, F. Miao, X. Wang, J. Wang, and Z. Ni, “Strong photoluminescence enhancement of MoS<sub>2</sub>

through defect engineering and oxygen bonding," *ACS Nano*, vol. 8, pp. 5738–5745, may 2014.

- [9] S. Mouri, Y. Miyauchi, and K. Matsuda, "Tunable photoluminescence of monolayer MoS<sub>2</sub> via chemical doping," *Nano Letters*, vol. 13, pp. 5944–5948, nov 2013.
- [10] M. Zhang, J. Wu, Y. Zhu, D. O. Dumcenco, J. Hong, N. Mao, S. Deng, Y. Chen, Y. Yang, C. Jin, S. H. Chaki, Y.-S. Huang, J. Zhang, and L. Xie, "Two-dimensional molybdenum tungsten diselenide alloys: Photoluminescence, raman scattering, and electrical transport," *ACS Nano*, vol. 8, pp. 7130–7137, jun 2014.
- [11] K. F. Mak, K. He, C. Lee, G. H. Lee, J. Hone, T. F. Heinz, and J. Shan, "Tightly bound trions in monolayer MoS<sub>2</sub>," *Nature Materials*, vol. 12, pp. 207–211, dec 2012.
- [12] K. F. Mak, K. He, J. Shan, and T. F. Heinz, "Control of valley polarization in monolayer MoS<sub>2</sub> by optical helicity," *Nature Nanotechnology*, vol. 7, pp. 494–498, jun 2012.
- [13] T. Yan, X. Qiao, X. Liu, P. Tan, and X. Zhang, "Photoluminescence properties and exciton dynamics in monolayer WSe<sub>2</sub>," *Applied Physics Letters*, vol. 105, p. 101901, sep 2014.
- [14] Z. Hu, J. Avila, X. Wang, J. F. Leong, Q. Zhang, Y. Liu, M. C. Asensio, J. Lu, A. Carvalho, C. H. Sow, and A. H. C. Neto, "The role of oxygen atoms on excitons at the edges of monolayer WS<sub>2</sub>," *Nano Letters*, jun 2019.
- [15] H. Haug, S. W. Koch, and L. V. Keldysh, "Quantum theory of the optical and electronic properties of semiconductors," *Physics Today*, vol. 47, pp. 106–108, feb 2004.
- [16] J. S. Ross, S. Wu, H. Yu, N. J. Ghimire, A. M. Jones, G. Aivazian, J. Yan, D. G. Mandrus, D. Xiao, W. Yao, and X. Xu, "Electrical control of neutral and charged excitons in a monolayer semiconductor," *Nature Communications*, vol. 4, feb 2013.
- [17] J. Shang, X. Shen, C. Cong, N. Peimyoo, B. Cao, M. Eginligil, and T. Yu, "Observation of excitonic fine structure in a 2d transition-metal dichalcogenide semiconductor," *ACS Nano*, vol. 9, no. 1, pp. 647–655, 2015. PMID: 25560634.

- [18] Y. You, X.-X. Zhang, T. C. Berkelbach, M. S. Hybertsen, D. R. Reichman, and T. F. Heinz, “Observation of biexcitons in monolayer WSe<sub>2</sub>,” *Nature Physics*, vol. 11, pp. 477–481, may 2015.
- [19] M. Barbone, A. R.-P. Montblanch, D. M. Kara, C. Palacios-Berraquero, A. R. Cadore, D. D. Fazio, B. Pingault, E. Mostaani, H. Li, B. Chen, K. Watanabe, T. Taniguchi, S. Tongay, G. Wang, A. C. Ferrari, and M. Atatüre, “Charge-tunable biexciton complexes in monolayer WSe<sub>2</sub>,” *Nature Communications*, vol. 9, sep 2018.
- [20] J. Feldmann, G. Peter, E. O. Göbel, P. Dawson, K. Moore, C. Foxon, and R. J. Elliott, “Linewidth dependence of radiative exciton lifetimes in quantum wells,” *Physical Review Letters*, vol. 60, pp. 243–243, jan 1988.
- [21] H. Haug and L. Bányai, eds., *Optical Switching in Low-Dimensional Systems*. Springer US, 1989.
- [22] K. F. Mak, C. Lee, J. Hone, J. Shan, and T. F. Heinz, “Atomically ThinMoS<sub>2</sub>: A new direct-gap semiconductor,” *Physical Review Letters*, vol. 105, p. 136805, sep 2010.
- [23] J. Feldmann, G. Peter, E. O. Göbel, P. Dawson, K. Moore, C. Foxon, and R. J. Elliott, “Linewidth dependence of radiative exciton lifetimes in quantum wells,” *Physical Review Letters*, vol. 59, pp. 2337–2340, nov 1987.
- [24] K. F. Mak and J. Shan, “Photonics and optoelectronics of 2d semiconductor transition metal dichalcogenides,” *Nature Photonics*, vol. 10, pp. 216–226, mar 2016.
- [25] M. Massicotte, P. Schmidt, F. Vialla, K. G. Schädler, A. Reserbat-Plantey, K. Watanabe, T. Taniguchi, K. J. Tielrooij, and F. H. L. Koppens, “Picosecond photoresponse in van der waals heterostructures,” *Nature Nanotechnology*, vol. 11, pp. 42–46, oct 2015.
- [26] T. Korn, S. Heydrich, M. Hirmer, J. Schmutzler, and C. Schüller, “Low-temperature photocarrier dynamics in monolayer MoS<sub>2</sub>,” *Applied Physics Letters*, vol. 99, p. 102109, sep 2011.
- [27] R. Wang, B. A. Ruzicka, N. Kumar, M. Z. Bellus, H.-Y. Chiu, and H. Zhao, “Ultrafast and spatially resolved studies of charge carriers in atomically thin molybdenum disulfide,” *Physical Review B*, vol. 86, jul 2012.

- [28] S. M. Sze, *Semiconductor Devices: Physics and Technology*. Wiley, 2002.
- [29] O. Lopez-Sanchez, D. Lembke, M. Kayci, A. Radenovic, and A. Kis, “Ultrasensitive photodetectors based on monolayer MoS<sub>2</sub>,” *Nature Nanotechnology*, vol. 8, pp. 497–501, jun 2013.
- [30] D.-S. Tsai, K.-K. Liu, D.-H. Lien, M.-L. Tsai, C.-F. Kang, C.-A. Lin, L.-J. Li, and J.-H. He, “Few-layer MoS<sub>2</sub> with high broadband photogain and fast optical switching for use in harsh environments,” *ACS Nano*, vol. 7, pp. 3905–3911, apr 2013.
- [31] O. Katz, V. Garber, B. Meyler, G. Bahir, and J. Salzman, “Gain mechanism in GaN schottky ultraviolet detectors,” *Applied Physics Letters*, vol. 79, pp. 1417–1419, sep 2001.
- [32] M. M. Furchi, D. K. Polyushkin, A. Pospischil, and T. Mueller, “Mechanisms of photoconductivity in atomically thin MoS<sub>2</sub>,” *Nano Letters*, vol. 14, pp. 6165–6170, oct 2014.
- [33] F. Withers, O. D. Pozo-Zamudio, A. Mishchenko, A. P. Rooney, A. Gholinia, K. Watanabe, T. Taniguchi, S. J. Haigh, A. K. Geim, A. I. Tartakovskii, and K. S. Novoselov, “Light-emitting diodes by band-structure engineering in van der waals heterostructures,” *Nature Materials*, vol. 14, pp. 301–306, feb 2015.
- [34] R. Cheng, D. Li, H. Zhou, C. Wang, A. Yin, S. Jiang, Y. Liu, Y. Chen, Y. Huang, and X. Duan, “Electroluminescence and photocurrent generation from atomically sharp WSe<sub>2</sub>/MoS<sub>2</sub> heterojunction p–n diodes,” *Nano Letters*, vol. 14, pp. 5590–5597, sep 2014.
- [35] J. S. Ross, P. Klement, A. M. Jones, N. J. Ghimire, J. Yan, D. G. Mandrus, T. Taniguchi, K. Watanabe, K. Kitamura, W. Yao, D. H. Cobden, and X. Xu, “Electrically tunable excitonic light-emitting diodes based on monolayer WSe<sub>2</sub> p–n junctions,” *Nature Nanotechnology*, vol. 9, pp. 268–272, mar 2014.
- [36] M. Fontana, T. Deppe, A. K. Boyd, M. Rinzan, A. Y. Liu, M. Paranjape, and P. Barbara, “Electron-hole transport and photovoltaic effect in gated MoS<sub>2</sub> schottky junctions,” *Scientific Reports*, vol. 3, apr 2013.

- [37] B. W. H. Baugher, H. O. H. Churchill, Y. Yang, and P. Jarillo-Herrero, “Opto-electronic devices based on electrically tunable p–n diodes in a monolayer dichalcogenide,” *Nature Nanotechnology*, vol. 9, pp. 262–267, mar 2014.
- [38] C.-H. Lee, G.-H. Lee, A. M. van der Zande, W. Chen, Y. Li, M. Han, X. Cui, G. Arefe, C. Nuckolls, T. F. Heinz, J. Guo, J. Hone, and P. Kim, “Atomically thin p–n junctions with van der waals heterointerfaces,” *Nature Nanotechnology*, vol. 9, pp. 676–681, aug 2014.
- [39] R. S. Sundaram, M. Engel, A. Lombardo, R. Krupke, A. C. Ferrari, P. Avouris, and M. Steiner, “Electroluminescence in single layer MoS<sub>2</sub>,” *Nano Letters*, vol. 13, pp. 1416–1421, mar 2013.
- [40] A. Pospischil, M. M. Furchi, and T. Mueller, “Solar-energy conversion and light emission in an atomic monolayer p–n diode,” *Nature Nanotechnology*, vol. 9, pp. 257–261, mar 2014.
- [41] Y. J. Zhang, T. Oka, R. Suzuki, J. T. Ye, and Y. Iwasa, “Electrically switchable chiral light-emitting transistor,” *Science*, vol. 344, pp. 725–728, apr 2014.
- [42] S. Wu, S. Buckley, J. R. Schaibley, L. Feng, J. Yan, D. G. Mandrus, F. Hatami, W. Yao, J. Vučković, A. Majumdar, and X. Xu, “Monolayer semiconductor nanocavity lasers with ultralow thresholds,” *Nature*, vol. 520, pp. 69–72, mar 2015.
- [43] Y. Ye, Z. J. Wong, X. Lu, X. Ni, H. Zhu, X. Chen, Y. Wang, and X. Zhang, “Monolayer excitonic laser,” *Nature Photonics*, vol. 9, pp. 733–737, oct 2015.
- [44] O. Salehzadeh, M. Djavid, N. H. Tran, I. Shih, and Z. Mi, “Optically pumped two-dimensional MoS<sub>2</sub> lasers operating at room-temperature,” *Nano Letters*, vol. 15, pp. 5302–5306, jul 2015.
- [45] K. F. Mak, K. L. McGill, J. Park, and P. L. McEuen, “The valley hall effect in MoS<sub>2</sub> transistors,” *Science*, vol. 344, pp. 1489–1492, jun 2014.
- [46] H. Yuan, X. Wang, B. Lian, H. Zhang, X. Fang, B. Shen, G. Xu, Y. Xu, S.-C. Zhang, H. Y. Hwang, and Y. Cui, “Generation and electric control of spin–valley-coupled circular photogalvanic current in WSe<sub>2</sub>,” *Nature Nanotechnology*, vol. 9, pp. 851–857, sep 2014.

- [47] W. Zhao, Z. Ghorannevis, K. K. Amara, J. R. Pang, M. Toh, X. Zhang, C. Kloc, P. H. Tan, and G. Eda, “Lattice dynamics in mono- and few-layer sheets of WS<sub>2</sub> and WSe<sub>2</sub>,” *Nanoscale*, vol. 5, p. 9677, August 2013.
- [48] A. Berkdemir, H. R. Gutiérrez, A. R. Botello-Méndez, N. Pereira-López, A. L. Elías, C.-I. Chia, B. Wang, V. H. Crespi, F. López-Urías, J.-C. Charlier, H. Terrones, and M. Terrones, “Identification of individual and few layers of WS<sub>2</sub> using raman spectroscopy,” *Scientific Reports*, vol. 3, apr 2013.
- [49] C. Lee, H. Yan, L. E. Brus, T. F. Heinz, J. Hone, and S. Ryu, “Anomalous lattice vibrations of single- and few-layer MoS<sub>2</sub>,” *ACS Nano*, vol. 4, pp. 2695–2700, apr 2010.
- [50] W. S. Yun, S. W. Han, S. C. Hong, I. G. Kim, and J. D. Lee, “Thickness and strain effects on electronic structures of transition metal dichalcogenides: 2h-MX<sub>2</sub>semiconductors (m=mo, w;x=s, se, te),” *Physical Review B*, vol. 85, jan 2012.
- [51] H. Terrones, E. D. Corro, S. Feng, J. M. Poumirol, D. Rhodes, D. Smirnov, N. R. Pradhan, Z. Lin, M. A. T. Nguyen, A. L. Elías, T. E. Mallouk, L. Balicas, M. A. Pimenta, and M. Terrones, “New first order raman-active modes in few layered transition metal dichalcogenides,” *Scientific Reports*, vol. 4, feb 2014.
- [52] M. W. Iqbal, M. Z. Iqbal, M. F. Khan, M. A. Shehzad, Y. Seo, J. H. Park, C. Hwang, and J. Eom, “High-mobility and air-stable single-layer WS<sub>2</sub> field-effect transistors sandwiched between chemical vapor deposition-grown hexagonal BN films,” *Scientific Reports*, vol. 5, jun 2015.
- [53] N. Peimyoo, J. Shang, C. Cong, X. Shen, X. Wu, E. K. L. Yeow, and T. Yu, “Nonblinking, intense two-dimensional light emitter: Monolayer WS<sub>2</sub> triangles,” *ACS Nano*, vol. 7, no. 12, pp. 10985–10994, 2013. PMID: 24266716.
- [54] Z. Y. Zhu, Y. C. Cheng, and U. Schwingenschlögl, “Giant spin-orbit-induced spin splitting in two-dimensional transition-metal dichalcogenide semiconductors,” *Physical Review B*, vol. 84, p. 153402, oct 2011.
- [55] F. Reale, K. Sharda, and C. Mattevi, “From bulk crystals to atomically thin layers of group VI-transition metal dichalcogenides vapour phase synthesis,” *Applied Materials Today*, vol. 3, pp. 11–22, jun 2016.

- [56] P. Schmidt, M. Binnewies, R. Glaum, and M. Schmidt, “Chemical vapor transport reactions—methods, materials, modeling,” in *Advanced Topics on Crystal Growth*, InTech, feb 2013.
- [57] A. Al-Hilli and B. Evans, “The preparation and properties of transition metal dichalcogenide single crystals,” *Journal of Crystal Growth*, vol. 15, pp. 93–101, jul 1972.
- [58] L. Brixner, “Preparation and properties of the single crystalline AB<sub>2</sub>-type selenides and tellurides of niobium, tantalum, molybdenum and tungsten,” *Journal of Inorganic and Nuclear Chemistry*, vol. 24, pp. 257–263, mar 1962.
- [59] M. Lenz and R. Gruehn, “Developments in measuring and calculating chemical vapor transport phenomena demonstrated on cr, mo, w, and their compounds,” *Chemical Reviews*, vol. 97, pp. 2967–2994, dec 1997.
- [60] B. E. Brown, “The crystal structures of WTe<sub>2</sub>and high-temperature MoTe<sub>2</sub>,” *Acta Crystallographica*, vol. 20, pp. 268–274, feb 1966.
- [61] K. Sunil and M. A. Ittyachen, “The growth and thermodynamical feasibility of tungsten diselenide single crystals using chemical vapour transport technique,” *Bulletin of Materials Science*, vol. 20, pp. 231–238, apr 1997.
- [62] J.-W. Chung, Z. Dai, and F. Ohuchi, “WS<sub>2</sub> thin films by metal organic chemical vapor deposition,” *Journal of Crystal Growth*, vol. 186, pp. 137–150, mar 1998.
- [63] A. L. Elías, N. Perea-López, A. Castro-Beltrán, A. Berkdemir, R. Lv, S. Feng, A. D. Long, T. Hayashi, Y. A. Kim, M. Endo, H. R. Gutiérrez, N. R. Pradhan, L. Balicas, T. E. Mallouk, F. López-Urías, H. Terrones, and M. Terrones, “Controlled synthesis and transfer of large-area ws<sub>2</sub> sheets: From single layer to few layers,” *ACS Nano*, vol. 7, no. 6, pp. 5235–5242, 2013. PMID: 23647141.
- [64] C. Cong, J. Shang, X. Wu, B. Cao, N. Peimyoo, C. Qiu, L. Sun, and T. Yu, “Synthesis and optical properties of large-area single-crystalline 2d semiconductor WS<sub>2</sub>monolayer from chemical vapor deposition,” *Advanced Optical Materials*, vol. 2, pp. 131–136, dec 2013.

- [65] Y. Rong, Y. Fan, A. L. Koh, A. W. Robertson, K. He, S. Wang, H. Tan, R. Sinclair, and J. H. Warner, “Controlling sulphur precursor addition for large single crystal domains of WS<sub>2</sub>,” *Nanoscale*, vol. 6, pp. 12096–12103, sep 2014.
- [66] D. Dumcenco, D. Ovchinnikov, K. Marinov, P. Lazić, M. Gibertini, N. Marzari, O. L. Sanchez, Y.-C. Kung, D. Krasnozhon, M.-W. Chen, S. Bertolazzi, P. Gillet, A. F. i Morral, A. Radenovic, and A. Kis, “Large-area epitaxial monolayer MoS<sub>2</sub>,” *ACS Nano*, vol. 9, pp. 4611–4620, apr 2015.
- [67] Y.-H. Lee, X.-Q. Zhang, W. Zhang, M.-T. Chang, C.-T. Lin, K.-D. Chang, Y.-C. Yu, J. T.-W. Wang, C.-S. Chang, L.-J. Li, and T.-W. Lin, “Synthesis of large-area MoS<sub>2</sub>atomic layers with chemical vapor deposition,” *Advanced Materials*, vol. 24, pp. 2320–2325, mar 2012.
- [68] X. Ling, Y.-H. Lee, Y. Lin, W. Fang, L. Yu, M. S. Dresselhaus, and J. Kong, “Role of the seeding promoter in MoS<sub>2</sub> growth by chemical vapor deposition,” *Nano Letters*, vol. 14, pp. 464–472, jan 2014.
- [69] S. Najmaei, Z. Liu, W. Zhou, X. Zou, G. Shi, S. Lei, B. I. Yakobson, J.-C. Idrobo, P. M. Ajayan, and J. Lou, “Vapour phase growth and grain boundary structure of molybdenum disulphide atomic layers,” *Nature Materials*, vol. 12, pp. 754–759, jun 2013.
- [70] Q. Ji, Y. Zhang, T. Gao, Y. Zhang, D. Ma, M. Liu, Y. Chen, X. Qiao, P.-H. Tan, M. Kan, J. Feng, Q. Sun, and Z. Liu, “Epitaxial monolayer MoS<sub>2</sub> on mica with novel photoluminescence,” *Nano Letters*, vol. 13, pp. 3870–3877, aug 2013.
- [71] Y. Zhang, Q. Ji, G.-F. Han, J. Ju, J. Shi, D. Ma, J. Sun, Y. Zhang, M. Li, X.-Y. Lang, Y. Zhang, and Z. Liu, “Dendritic, transferable, strictly monolayer MoS<sub>2</sub> flakes synthesized on SrTiO<sub>3</sub> single crystals for efficient electrocatalytic applications,” *ACS Nano*, vol. 8, pp. 8617–8624, jul 2014.
- [72] Y. Yu, C. Li, Y. Liu, L. Su, Y. Zhang, and L. Cao, “Controlled scalable synthesis of uniform, high-quality monolayer and few-layer MoS<sub>2</sub> films,” *Scientific Reports*, vol. 3, may 2013.
- [73] M. Bosi, “Growth and synthesis of mono and few-layers transition metal dichalcogenides by vapour techniques: a review,” *RSC Advances*, vol. 5, no. 92, pp. 75500–75518, 2015.

- [74] Y. Shi, H. Li, and L.-J. Li, “Recent advances in controlled synthesis of two-dimensional transition metal dichalcogenides via vapour deposition techniques,” *Chemical Society Reviews*, vol. 44, no. 9, pp. 2744–2756, 2015.
- [75] Y. Zhang, Y. Zhang, Q. Ji, J. Ju, H. Yuan, J. Shi, T. Gao, D. Ma, M. Liu, Y. Chen, X. Song, H. Y. Hwang, Y. Cui, and Z. Liu, “Controlled growth of high-quality monolayer ws<sub>2</sub> layers on sapphire and imaging its grain boundary,” *ACS Nano*, vol. 7, no. 10, pp. 8963–8971, 2013. PMID: 24047054.
- [76] S. Li, S. Wang, D.-M. Tang, W. Zhao, H. Xu, L. Chu, Y. Bando, D. Golberg, and G. Eda, “Halide-assisted atmospheric pressure growth of large WSe<sub>2</sub> and WS<sub>2</sub> monolayer crystals,” *Applied Materials Today*, vol. 1, pp. 60–66, nov 2015.
- [77] Y.-H. Lee, L. Yu, H. Wang, W. Fang, X. Ling, Y. Shi, C.-T. Lin, J.-K. Huang, M.-T. Chang, C.-S. Chang, M. Dresselhaus, T. Palacios, L.-J. Li, and J. Kong, “Synthesis and transfer of single-layer transition metal disulfides on diverse surfaces,” *Nano Letters*, vol. 13, pp. 1852–1857, mar 2013.
- [78] M. Okada, T. Sawazaki, K. Watanabe, T. Taniguchi, H. Hibino, H. Shinohara, and R. Kitaura, “Direct chemical vapor deposition growth of ws<sub>2</sub> atomic layers on hexagonal boron nitride,” *ACS Nano*, vol. 8, no. 8, pp. 8273–8277, 2014. PMID: 25093606.
- [79] G. H. Ahn, M. Amani, H. Rasool, D.-H. Lien, J. P. Mastandrea, J. W. A. III, M. Dubey, D. C. Chrzan, A. M. Minor, and A. Javey, “Strain-engineered growth of two-dimensional materials,” *Nature Communications*, vol. 8, sep 2017.
- [80] W.-T. Hsu, L.-S. Lu, D. Wang, J.-K. Huang, M.-Y. Li, T.-R. Chang, Y.-C. Chou, Z.-Y. Juang, H.-T. Jeng, L.-J. Li, and W.-H. Chang, “Evidence of indirect gap in monolayer WSe<sub>2</sub>,” *Nature Communications*, vol. 8, oct 2017.
- [81] B. Amin, N. Singh, and U. Schwingenschlögl, “Heterostructures of transition metal dichalcogenides,” *Physical Review B*, vol. 92, aug 2015.
- [82] X. Hong, J. Kim, S.-F. Shi, Y. Zhang, C. Jin, Y. Sun, S. Tongay, J. Wu, Y. Zhang, and F. Wang, “Ultrafast charge transfer in atomically thin MoS<sub>2</sub>/WS<sub>2</sub> heterostructures,” *Nature Nanotechnology*, vol. 9, pp. 682–686, aug 2014.

- [83] C. Gong, H. Zhang, W. Wang, L. Colombo, R. M. Wallace, and K. Cho, “Band alignment of two-dimensional transition metal dichalcogenides: Application in tunnel field effect transistors,” *Applied Physics Letters*, vol. 103, p. 053513, jul 2013.
- [84] S. Tongay, W. Fan, J. Kang, J. Park, U. Koldemir, J. Suh, D. S. Narang, K. Liu, J. Ji, J. Li, R. Sinclair, and J. Wu, “Tuning interlayer coupling in large-area heterostructures with CVD-grown MoS<sub>2</sub> and WS<sub>2</sub> monolayers,” *Nano Letters*, vol. 14, pp. 3185–3190, may 2014.
- [85] Y. Gong, J. Lin, X. Wang, G. Shi, S. Lei, Z. Lin, X. Zou, G. Ye, R. Vajtai, B. I. Yakobson, H. Terrones, M. Terrones, B. K. Tay, J. Lou, S. T. Pantelides, Z. Liu, W. Zhou, and P. M. Ajayan, “Vertical and in-plane heterostructures from WS<sub>2</sub>/MoS<sub>2</sub> monolayers,” *Nature Materials*, vol. 13, pp. 1135–1142, sep 2014.
- [86] A. M. van der Zande, J. Kunstmann, A. Chernikov, D. A. Chenet, Y. You, X. Zhang, P. Y. Huang, T. C. Berkelbach, L. Wang, F. Zhang, M. S. Hybertsen, D. A. Muller, D. R. Reichman, T. F. Heinz, and J. C. Hone, “Tailoring the electronic structure in bilayer molybdenum disulfide via interlayer twist,” *Nano Letters*, vol. 14, pp. 3869–3875, jun 2014.
- [87] P. K. Nayak, Y. Horbatenko, S. Ahn, G. Kim, J.-U. Lee, K. Y. Ma, A.-R. Jang, H. Lim, D. Kim, S. Ryu, H. Cheong, N. Park, and H. S. Shin, “Probing evolution of twist-angle-dependent interlayer excitons in MoSe<sub>2</sub>/WSe<sub>2</sub> van der waals heterostructures,” *ACS Nano*, vol. 11, pp. 4041–4050, apr 2017.
- [88] H. Heo, J. H. Sung, S. Cha, B.-G. Jang, J.-Y. Kim, G. Jin, D. Lee, J.-H. Ahn, M.-J. Lee, J. H. Shim, H. Choi, and M.-H. Jo, “Interlayer orientation-dependent light absorption and emission in monolayer semiconductor stacks,” *Nature Communications*, vol. 6, jun 2015.
- [89] K. Liu, L. Zhang, T. Cao, C. Jin, D. Qiu, Q. Zhou, A. Zettl, P. Yang, S. G. Louie, and F. Wang, “Evolution of interlayer coupling in twisted molybdenum disulfide bilayers,” *Nature Communications*, vol. 5, sep 2014.
- [90] J. Kunstmann, F. Mooshammer, P. Nagler, A. Chaves, F. Stein, N. Paradiso, G. Plechinger, C. Strunk, C. Schüller, G. Seifert, D. R. Reichman, and T. Korn, “Momentum-space indirect interlayer excitons in transition-metal dichalcogenide van der waals heterostructures,” *Nature Physics*, vol. 14, pp. 801–805, apr 2018.

- [91] E. M. Alexeev, D. A. Ruiz-Tijerina, M. Danovich, M. J. Hamer, D. J. Terry, P. K. Nayak, S. Ahn, S. Pak, J. Lee, J. I. Sohn, M. R. Molas, M. Koperski, K. Watanabe, T. Taniguchi, K. S. Novoselov, R. V. Gorbachev, H. S. Shin, V. I. Fal'ko, and A. I. Tartakovskii, “Resonantly hybridized excitons in moiré superlattices in van der waals heterostructures,” *Nature*, vol. 567, pp. 81–86, mar 2019.
- [92] Y. Saito, Y. Nakamura, M. S. Bahramy, Y. Kohama, J. Ye, Y. Kasahara, Y. Nakagawa, M. Onga, M. Tokunaga, T. Nojima, Y. Yanase, and Y. Iwasa, “Superconductivity protected by spin–valley locking in ion-gated MoS<sub>2</sub>,” *Nature Physics*, vol. 12, pp. 144–149, dec 2015.
- [93] J. M. Lu, O. Zheliuk, I. Leermakers, N. F. Q. Yuan, U. Zeitler, K. T. Law, and J. T. Ye, “Evidence for two-dimensional ising superconductivity in gated MoS<sub>2</sub>,” *Science*, vol. 350, pp. 1353–1357, nov 2015.
- [94] X. Qian, J. Liu, L. Fu, and J. Li, “Quantum spin hall effect in two-dimensional transition metal dichalcogenides,” *Science*, vol. 346, pp. 1344–1347, nov 2014.
- [95] D.-H. Choe, H.-J. Sung, and K. J. Chang, “Understanding topological phase transition in monolayer transition metal dichalcogenides,” *Physical Review B*, vol. 93, mar 2016.
- [96] J. Liu, H. Wang, C. Fang, L. Fu, and X. Qian, “van der waals stacking-induced topological phase transition in layered ternary transition metal chalcogenides,” *Nano Letters*, vol. 17, pp. 467–475, dec 2016.
- [97] Z. Fei, T. Palomaki, S. Wu, W. Zhao, X. Cai, B. Sun, P. Nguyen, J. Finney, X. Xu, and D. H. Cobden, “Edge conduction in monolayer WTe<sub>2</sub>,” *Nature Physics*, vol. 13, pp. 677–682, apr 2017.
- [98] Y. Sun, S.-C. Wu, M. N. Ali, C. Felser, and B. Yan, “Prediction of weyl semimetal in orthorhombicMoTe<sub>2</sub>,” *Physical Review B*, vol. 92, oct 2015.
- [99] R. Kappera, D. Voiry, S. E. Yalcin, B. Branch, G. Gupta, A. D. Mohite, and M. Chhowalla, “Phase-engineered low-resistance contacts for ultrathin MoS<sub>2</sub> transistors,” *Nature Materials*, vol. 13, pp. 1128–1134, aug 2014.

- [100] D. H. Keum, S. Cho, J. H. Kim, D.-H. Choe, H.-J. Sung, M. Kan, H. Kang, J.-Y. Hwang, S. W. Kim, H. Yang, K. J. Chang, and Y. H. Lee, “Bandgap opening in few-layered monoclinic MoTe<sub>2</sub>,” *Nature Physics*, vol. 11, pp. 482–486, may 2015.
- [101] S. Cho, S. Kim, J. H. Kim, J. Zhao, J. Seok, D. H. Keum, J. Baik, D.-H. Choe, K. J. Chang, K. Suenaga, S. W. Kim, Y. H. Lee, and H. Yang, “Phase patterning for ohmic homojunction contact in MoTe<sub>2</sub>,” *Science*, vol. 349, pp. 625–628, aug 2015.
- [102] K.-A. N. Duerloo, Y. Li, and E. J. Reed, “Structural phase transitions in two-dimensional mo- and w-dichalcogenide monolayers,” *Nature Communications*, vol. 5, jul 2014.
- [103] H. Yang, S. W. Kim, M. Chhowalla, and Y. H. Lee, “Structural and quantum-state phase transitions in van der waals layered materials,” *Nature Physics*, vol. 13, pp. 931–937, jul 2017.
- [104] W. Li and J. Li, “Ferroelasticity and domain physics in two-dimensional transition metal dichalcogenide monolayers,” *Nature Communications*, vol. 7, feb 2016.
- [105] M. Chhowalla, H. S. Shin, G. Eda, L.-J. Li, K. P. Loh, and H. Zhang, “The chemistry of two-dimensional layered transition metal dichalcogenide nanosheets,” *Nature Chemistry*, vol. 5, pp. 263–275, mar 2013.
- [106] Y. Qi, P. G. Naumov, M. N. Ali, C. R. Rajamathi, W. Schnelle, O. Barkalov, M. Hanfland, S.-C. Wu, C. Shekhar, Y. Sun, V. Süß, M. Schmidt, U. Schwarz, E. Pippel, P. Werner, R. Hillebrand, T. Förster, E. Kampert, S. Parkin, R. J. Cava, C. Felser, B. Yan, and S. A. Medvedev, “Superconductivity in weyl semimetal candidate MoTe<sub>2</sub>,” *Nature Communications*, vol. 7, mar 2016.
- [107] C. L. Kane and E. J. Mele, “Quantum spin hall effect in graphene,” *Physical Review Letters*, vol. 95, nov 2005.
- [108] M. Konig, S. Wiedmann, C. Brune, A. Roth, H. Buhmann, L. W. Molenkamp, X.-L. Qi, and S.-C. Zhang, “Quantum spin hall insulator state in HgTe quantum wells,” *Science*, vol. 318, pp. 766–770, nov 2007.
- [109] Y.-C. Lin, D. O. Dumcenco, Y.-S. Huang, and K. Suenaga, “Atomic mechanism of the semiconducting-to-metallic phase transition in single-layered MoS<sub>2</sub>,” *Nature Nanotechnology*, vol. 9, pp. 391–396, apr 2014.

- [110] Y. Guo, D. Sun, B. Ouyang, A. Raja, J. Song, T. F. Heinz, and L. E. Brus, “Probing the dynamics of the metallic-to-semiconducting structural phase transformation in MoS<sub>2</sub> crystals,” *Nano Letters*, vol. 15, pp. 5081–5088, jul 2015.
- [111] Y. Kang, S. Najmaei, Z. Liu, Y. Bao, Y. Wang, X. Zhu, N. J. Halas, P. Nordlander, P. M. Ajayan, J. Lou, and Z. Fang, “Plasmonic hot electron induced structural phase transition in a MoS<sub>2</sub>monolayer,” *Advanced Materials*, vol. 26, pp. 6467–6471, aug 2014.
- [112] S. Song, D. H. Keum, S. Cho, D. Perello, Y. Kim, and Y. H. Lee, “Room temperature semiconductor–metal transition of MoTe<sub>2</sub> thin films engineered by strain,” *Nano Letters*, vol. 16, pp. 188–193, dec 2015.
- [113] D. Barrera, Q. Wang, Y.-J. Lee, L. Cheng, M. J. Kim, J. Kim, and J. W. P. Hsu, “Solution synthesis of few-layer 2h MX<sub>2</sub> (m = mo, w; x = s, se),” *Journal of Materials Chemistry C*, vol. 5, no. 11, pp. 2859–2864, 2017.
- [114] W. Jung, S. Lee, D. Yoo, S. Jeong, P. Miró, A. Kuc, T. Heine, and J. Cheon, “Colloidal synthesis of single-layer MSe<sub>2</sub> (m = mo, w) nanosheets via anisotropic solution-phase growth approach,” *Journal of the American Chemical Society*, vol. 137, pp. 7266–7269, jun 2015.
- [115] W. Zhao, Z. Ghorannevis, L. Chu, M. Toh, C. Kloc, P.-H. Tan, and G. Eda, “Evolution of electronic structure in atomically thin sheets of WS<sub>2</sub> and WSe<sub>2</sub>,” *ACS Nano*, vol. 7, pp. 791–797, dec 2012. PMID: 23256505.
- [116] K. F. Mak, K. He, J. Shan, and T. F. Heinz, “Control of valley polarization in monolayer MoS<sub>2</sub> by optical helicity,” *Nature Nanotechnology*, vol. 7, pp. 494–498, jun 2012.
- [117] H. Zeng, J. Dai, W. Yao, D. Xiao, and X. Cui, “Valley polarization in MoS<sub>2</sub> monolayers by optical pumping,” *Nature Nanotechnology*, vol. 7, pp. 490–493, jun 2012.
- [118] D. Xiao, G.-B. Liu, W. Feng, X. Xu, and W. Yao, “Coupled spin and valley physics in monolayers ofMoS<sub>2</sub>and other group-VI dichalcogenides,” *Physical Review Letters*, vol. 108, p. 196802, may 2012.

- [119] Y. Li, Y. Rao, K. F. Mak, Y. You, S. Wang, C. R. Dean, and T. F. Heinz, “Probing symmetry properties of few-layer MoS<sub>2</sub> and h-BN by optical second-harmonic generation,” *Nano Letters*, vol. 13, pp. 3329–3333, jun 2013. PMID: 23718906.
- [120] J. Wilson and A. Yoffe, “The transition metal dichalcogenides discussion and interpretation of the observed optical, electrical and structural properties,” *Advances in Physics*, vol. 18, pp. 193–335, may 1969.
- [121] T. Li and G. Galli, “Electronic properties of MoS<sub>2</sub>nano particles,” *The Journal of Physical Chemistry C*, vol. 111, pp. 16192–16196, nov 2007.
- [122] L. Yuan and L. Huang, “Exciton dynamics and annihilation in WS<sub>2</sub> 2d semiconductors,” *Nanoscale*, vol. 7, no. 16, pp. 7402–7408, 2015.
- [123] L. Lin, Y. Xu, S. Zhang, I. M. Ross, A. C. M. Ong, and D. A. Allwood, “Fabrication of luminescent monolayered tungsten dichalcogenides quantum dots with giant spin-valley coupling,” *ACS Nano*, vol. 7, no. 9, pp. 8214–8223, 2013. PMID: 23968363.
- [124] M. Amani, D.-H. Lien, D. Kiriya, J. Xiao, A. Azcatl, J. Noh, S. R. Madhvapathy, R. Addou, S. KC, M. Dubey, K. Cho, R. M. Wallace, S.-C. Lee, J.-H. He, J. W. Ager, X. Zhang, E. Yablonovitch, and A. Javey, “Near-unity photoluminescence quantum yield in MoS<sub>2</sub>,” *Science*, vol. 350, pp. 1065–1068, nov 2015.
- [125] S. Jo, N. Ubrig, H. Berger, A. B. Kuzmenko, and A. F. Morpurgo, “Mono- and bilayer ws<sub>2</sub> light-emitting transistors,” *Nano Letters*, vol. 14, no. 4, pp. 2019–2025, 2014. PMID: 24669957.
- [126] L. Zeng, L. Tao, C. Tang, B. Zhou, H. Long, Y. Chai, S. P. Lau, and Y. H. Tsang, “High-responsivity UV-vis photodetector based on transferable WS<sub>2</sub> film deposited by magnetron sputtering,” *Scientific Reports*, vol. 6, jan 2016.
- [127] W. K. Hofmann, “Thin films of molybdenum and tungsten disulphides by metal organic chemical vapour deposition,” *Journal of Materials Science*, vol. 23, pp. 3981–3986, nov 1988.
- [128] Z.-Q. Xu, Y. Zhang, S. Lin, C. Zheng, Y. L. Zhong, X. Xia, Z. Li, P. J. Sophia, M. S. Fuhrer, Y.-B. Cheng, and Q. Bao, “Synthesis and transfer of large-area monolayer ws<sub>2</sub> crystals: Moving toward the recyclable use of sapphire substrates,” *ACS Nano*, vol. 9, no. 6, pp. 6178–6187, 2015. PMID: 25961515.

- [129] Q. Fu, W. Wang, L. Yang, J. Huang, J. Zhang, and B. Xiang, “Controllable synthesis of high quality monolayer WS<sub>2</sub> on a SiO<sub>2</sub>/si substrate by chemical vapor deposition,” *RSC Advances*, vol. 5, no. 21, pp. 15795–15799, 2015.
- [130] K. Kang, S. Xie, L. Huang, Y. Han, P. Y. Huang, K. F. Mak, C.-J. Kim, D. Muller, and J. Park, “High-mobility three-atom-thick semiconducting films with wafer-scale homogeneity,” *Nature*, vol. 520, pp. 656–660, apr 2015.
- [131] Y. Gao, Z. Liu, D.-M. Sun, L. Huang, L.-P. Ma, L.-C. Yin, T. Ma, Z. Zhang, X.-L. Ma, L.-M. Peng, H.-M. Cheng, and W. Ren, “Large-area synthesis of high-quality and uniform monolayer WS<sub>2</sub> on reusable au foils,” *Nature Communications*, vol. 6, oct 2015.
- [132] S. J. Yun, S. H. Chae, H. Kim, J. C. Park, J.-H. Park, G. H. Han, J. S. Lee, S. M. Kim, H. M. Oh, J. Seok, M. S. Jeong, K. K. Kim, and Y. H. Lee, “Synthesis of centimeter-scale monolayer tungsten disulfide film on gold foils,” *ACS Nano*, vol. 9, pp. 5510–5519, apr 2015.
- [133] Y. Gong, Z. Lin, G. Ye, G. Shi, S. Feng, Y. Lei, A. L. Elías, N. Perea-Lopez, R. Vajtai, H. Terrones, Z. Liu, M. Terrones, and P. M. Ajayan, “Tellurium-assisted low-temperature synthesis of MoS<sub>2</sub> and WS<sub>2</sub> monolayers,” *ACS Nano*, vol. 9, pp. 11658–11666, nov 2015.
- [134] C. J. Carmalt, I. P. Parkin, and E. S. Peters, “Atmospheric pressure chemical vapour deposition of WS<sub>2</sub> thin films on glass,” *Polyhedron*, vol. 22, pp. 1499–1505, jun 2003.
- [135] S. M. Eichfeld, L. Hossain, Y.-C. Lin, A. F. Piasecki, B. Kupp, A. G. Birdwell, R. A. Burke, N. Lu, X. Peng, J. Li, A. Azcatl, S. McDonnell, R. M. Wallace, M. J. Kim, T. S. Mayer, J. M. Redwing, and J. A. Robinson, “Highly scalable, atomically thin WSe<sub>2</sub> grown via metal–organic chemical vapor deposition,” *ACS Nano*, vol. 9, pp. 2080–2087, feb 2015.
- [136] F. Reale, P. Palczynski, I. Amit, G. F. Jones, J. D. Mehew, A. Bacon, N. Ni, P. C. Sherrell, S. Agnoli, M. F. Craciun, S. Russo, and C. Mattevi, “High-mobility and high-optical quality atomically thin WS<sub>2</sub>,” *Scientific Reports*, vol. 7, nov 2017.
- [137] H. Kim, C. Mattevi, M. R. Calvo, J. C. Oberg, L. Artiglia, S. Agnoli, C. F. Hirjibehedin, M. Chhowalla, and E. Saiz, “Activation energy paths for graphene nucleation and growth on cu,” *ACS Nano*, vol. 6, pp. 3614–3623, mar 2012.

- [138] J. R. McKone, A. P. Pieterick, H. B. Gray, and N. S. Lewis, “Hydrogen evolution from pt/ru-coated p-type WSe<sub>2</sub> photocathodes,” *Journal of the American Chemical Society*, vol. 135, pp. 223–231, dec 2012.
- [139] J. Baglio, E. Kamieniecki, N. DeCola, C. Struck, J. Marzik, K. Dwight, and A. Wold, “Growth and characterization of n-WS<sub>2</sub> and niobium-doped p-WS<sub>2</sub> single crystals,” *Journal of Solid State Chemistry*, vol. 49, pp. 166–179, sep 1983.
- [140] A. Turler, “Gas phase chemistry of superheavy elements,” *Journal of Nuclear and Radiochemical Sciences*, vol. 5, no. 2, pp. R19–R25, 2004.
- [141] R. J. Wu, M. L. Odlyzko, and K. A. Mkhoyan, “Determining the thickness of atomically thin MoS<sub>2</sub> and WS<sub>2</sub> in the TEM,” *Ultramicroscopy*, vol. 147, pp. 8–20, dec 2014.
- [142] F. A. Rasmussen and K. S. Thygesen, “Computational 2d materials database: Electronic structure of transition-metal dichalcogenides and oxides,” *The Journal of Physical Chemistry C*, vol. 119, pp. 13169–13183, jun 2015.
- [143] F. Withers, T. H. Bointon, D. C. Hudson, M. F. Craciun, and S. Russo, “Electron transport of WS<sub>2</sub> transistors in a hexagonal boron nitride dielectric environment,” *Scientific Reports*, vol. 4, may 2014.
- [144] P. Hu, J. Ye, X. He, K. Du, K. K. Zhang, X. Wang, Q. Xiong, Z. Liu, H. Jiang, and C. Kloc, “Control of radiative exciton recombination by charge transfer induced surface dipoles in MoS<sub>2</sub> and WS<sub>2</sub> monolayers,” *Scientific Reports*, vol. 6, apr 2016.
- [145] K. N. Kang, K. Godin, and E.-H. Yang, “The growth scale and kinetics of WS<sub>2</sub> monolayers under varying h<sub>2</sub> concentration,” *Scientific Reports*, vol. 5, aug 2015.
- [146] Y. Y. Hui, X. Liu, W. Jie, N. Y. Chan, J. Hao, Y.-T. Hsu, L.-J. Li, W. Guo, and S. P. Lau, “Exceptional tunability of band energy in a compressively strained trilayer MoS<sub>2</sub> sheet,” *ACS Nano*, vol. 7, pp. 7126–7131, jul 2013.
- [147] N. Peimyoo, W. Yang, J. Shang, X. Shen, Y. Wang, and T. Yu, “Chemically driven tunable light emission of charged and neutral excitons in monolayer WS<sub>2</sub>,” *ACS Nano*, vol. 8, pp. 11320–11329, oct 2014.

- [148] S. Tongay, J. Suh, C. Ataca, W. Fan, A. Luce, J. S. Kang, J. Liu, C. Ko, R. Raghunathanan, J. Zhou, F. Ogletree, J. Li, J. C. Grossman, and J. Wu, “Defects activated photoluminescence in two-dimensional semiconductors: interplay between bound, charged and free excitons,” *Scientific Reports*, vol. 3, sep 2013.
- [149] Z. Liu, M. Amani, S. Najmaei, Q. Xu, X. Zou, W. Zhou, T. Yu, C. Qiu, A. G. Birdwell, F. J. Crowne, R. Vajtai, B. I. Yakobson, Z. Xia, M. Dubey, P. M. Ajayan, and J. Lou, “Strain and structure heterogeneity in MoS<sub>2</sub> atomic layers grown by chemical vapour deposition,” *Nature Communications*, vol. 5, nov 2014.
- [150] H. Liu, J. Lu, K. Ho, Z. Hu, Z. Dang, A. Carvalho, H. R. Tan, E. S. Tok, and C. H. Sow, “Fluorescence concentric triangles: A case of chemical heterogeneity in WS<sub>2</sub> atomic monolayer,” *Nano Letters*, vol. 16, pp. 5559–5567, aug 2016.
- [151] M. Cattelan, B. Markman, G. Lucchini, P. K. Das, I. Vobornik, J. A. Robinson, S. Agnoli, and G. Granozzi, “New strategy for the growth of complex heterostructures based on different 2d materials,” *Chemistry of Materials*, vol. 27, pp. 4105–4113, may 2015.
- [152] H. Martinez, A. Benayad, D. Gonbeau, P. Vinatier, B. Pecquenard, and A. Levasseur, “Influence of the cation nature of high sulfur content oxysulfide thin films MO<sub>y</sub>S<sub>z</sub> (m=w, ti) studied by XPS,” *Applied Surface Science*, vol. 236, pp. 377–386, sep 2004.
- [153] A. Alharbi and D. Shahrjerdi, “Electronic properties of monolayer tungsten disulfide grown by chemical vapor deposition,” *Applied Physics Letters*, vol. 109, p. 193502, nov 2016.
- [154] C. Lan, C. Li, Y. Yin, and Y. Liu, “Large-area synthesis of monolayer WS<sub>2</sub> and its ambient-sensitive photo-detecting performance,” *Nanoscale*, vol. 7, no. 14, pp. 5974–5980, 2015.
- [155] A. M. Hussain, G. A. T. Sevilla, K. R. Rader, and M. M. Hussain, “Chemical vapor deposition based tungsten disulfide (WS<sub>2</sub>) thin film transistor,” in *2013 Saudi International Electronics, Communications and Photonics Conference*, IEEE, apr 2013.

- [156] Y. Cui, R. Xin, Z. Yu, Y. Pan, Z.-Y. Ong, X. Wei, J. Wang, H. Nan, Z. Ni, Y. Wu, T. Chen, Y. Shi, B. Wang, G. Zhang, Y.-W. Zhang, and X. Wang, “High-performance monolayer WS<sub>2</sub> field-effect transistors on high- $\kappa$  dielectrics,” *Advanced Materials*, vol. 27, pp. 5230–5234, aug 2015.
- [157] M. W. Iqbal, M. Z. Iqbal, M. F. Khan, M. A. Kamran, A. Majid, T. Alharbi, and J. Eom, “Tailoring the electrical and photo-electrical properties of a WS<sub>2</sub> field effect transistor by selective n-type chemical doping,” *RSC Advances*, vol. 6, no. 29, pp. 24675–24682, 2016.
- [158] T. Georgiou, H. Yang, R. Jalil, J. Chapman, K. S. Novoselov, and A. Mishchenko, “Electrical and optical characterization of atomically thin WS<sub>2</sub>,” *Dalton Transactions*, vol. 43, no. 27, p. 10388, 2014.
- [159] M. W. Iqbal, M. Z. Iqbal, M. F. Khan, M. A. Shehzad, Y. Seo, and J. Eom, “Deep-ultraviolet-light-driven reversible doping of WS<sub>2</sub> field-effect transistors,” *Nanoscale*, vol. 7, no. 2, pp. 747–757, 2015.
- [160] D. Ovchinnikov, A. Allain, Y.-S. Huang, D. Dumcenco, and A. Kis, “Electrical transport properties of single-layer WS<sub>2</sub>,” *ACS Nano*, vol. 8, pp. 8174–8181, jul 2014.
- [161] X. Hu, P. Yasaie, J. Jokisaari, S. Öğüt, A. Salehi-Khojin, and R. F. Klie, “Mapping thermal expansion coefficients in freestanding 2d materials at the nanometer scale,” *Physical Review Letters*, vol. 120, feb 2018.
- [162] H. Tada, A. E. Kumpel, R. E. Lathrop, J. B. Slanina, P. Nieva, P. Zavracky, I. N. Miaoulis, and P. Y. Wong, “Thermal expansion coefficient of polycrystalline silicon and silicon dioxide thin films at high temperatures,” *Journal of Applied Physics*, vol. 87, pp. 4189–4193, may 2000.
- [163] O. B. Aslan, M. Deng, and T. F. Heinz, “Strain tuning of excitons in monolayer WSe<sub>2</sub>,” *Physical Review B*, vol. 98, sep 2018.
- [164] A. M. Dadgar, D. Scullion, K. Kang, D. Esposito, E. H. Yang, I. P. Herman, M. A. Pimenta, E.-J. G. Santos, and A. N. Pasupathy, “Strain engineering and raman spectroscopy of monolayer transition metal dichalcogenides,” *Chemistry of Materials*, vol. 30, pp. 5148–5155, jul 2018.

- [165] B. G. Yacobi, F. W. Boswell, and J. M. Corbett, “Intercalation-induced shift of the absorption edge in ZrS<sub>2</sub>and HfS<sub>2</sub>,” *Journal of Physics C: Solid State Physics*, vol. 12, pp. 2189–2196, jun 1979.
- [166] B. Yacobi, F. Boswell, and J. Corbett, “The fundamental absorption edge in Ni<sub>x</sub>ZrS<sub>2</sub>,” *Materials Research Bulletin*, vol. 14, pp. 1033–1038, aug 1979.
- [167] M. Deshpande, S. Gupta, A. Agarwal, and M. Agarwal, “Transport and optical property measurements in indium intercalated molybdenum diselenide single crystals grown by DVT technique,” *Synthetic Metals*, vol. 123, pp. 73–81, aug 2001.
- [168] G. S. Rao and C. Sunandana, “LAYERED DICHALCOGENIDES AND INTERCALATED MATERIALS,” in *Preparation and Characterization of Materials*, pp. 269–282, Elsevier, 1981.
- [169] C. D. Wagner, “The nist x-ray photoelectron spectroscopy (xps) database.” Online, 1991.
- [170] R. B. Somoano and J. A. Woollam, “Intercalation compounds of molybdenum disulfide,” in *Intercalated Layered Materials*, pp. 307–319, Springer Netherlands, 1979.
- [171] H. Hahn and W. Klingler, “Über die kristallstrukturen des in<sub>2</sub>s<sub>3</sub>und in<sub>2</sub>te<sub>3</sub>,” *Zeitschrift für anorganische Chemie*, vol. 260, pp. 97–109, oct 1949.
- [172] D. Voiry, H. Yamaguchi, J. Li, R. Silva, D. C. B. Alves, T. Fujita, M. Chen, T. Asefa, V. B. Shenoy, G. Eda, and M. Chhowalla, “Enhanced catalytic activity in strained chemically exfoliated WS<sub>2</sub> nanosheets for hydrogen evolution,” *Nature Materials*, vol. 12, pp. 850–855, jul 2013.
- [173] F. Wypych and R. Schöllhorn, “1t-MoS<sub>2</sub>, a new metallic modification of molybdenum disulfide,” *J. Chem. Soc., Chem. Commun.*, no. 19, pp. 1386–1388, 1992.
- [174] P. Chen, W. W. Pai, Y.-H. Chan, W.-L. Sun, C.-Z. Xu, D.-S. Lin, M. Y. Chou, A.-V. Fedorov, and T.-C. Chiang, “Large quantum-spin-hall gap in single-layer 1t/WSe<sub>2</sub>,” *Nature Communications*, vol. 9, may 2018.
- [175] Y. Xu, B. Yan, H.-J. Zhang, J. Wang, G. Xu, P. Tang, W. Duan, and S.-C. Zhang, “Large-gap quantum spin hall insulators in tin films,” *Physical Review Letters*, vol. 111, sep 2013.

- [176] D. V. Gruznev, S. V. Eremeev, L. V. Bondarenko, A. Y. Tupchaya, A. A. Yakovlev, A. N. Mihalyuk, J.-P. Chou, A. V. Zотов, and A. A. Saranin, “Two-dimensional in-sb compound on silicon as a quantum spin hall insulator,” *Nano Letters*, vol. 18, pp. 4338–4345, jun 2018.
- [177] Y. Yu, G.-H. Nam, Q. He, X.-J. Wu, K. Zhang, Z. Yang, J. Chen, Q. Ma, M. Zhao, Z. Liu, F.-R. Ran, X. Wang, H. Li, X. Huang, B. Li, Q. Xiong, Q. Zhang, Z. Liu, L. Gu, Y. Du, W. Huang, and H. Zhang, “High phase-purity 1t'-MoS<sub>2</sub>- and 1t'-MoSe<sub>2</sub>-layered crystals,” *Nature Chemistry*, vol. 10, pp. 638–643, apr 2018.
- [178] B. Lei, Y. Pan, Z. Hu, J. Zhang, D. Xiang, Y. Zheng, R. Guo, C. Han, L. Wang, J. Lu, L. Yang, and W. Chen, “Direct observation of semiconductor–metal phase transition in bilayer tungsten diselenide induced by potassium surface functionalization,” *ACS Nano*, vol. 12, pp. 2070–2077, jan 2018.
- [179] M. S. Sokolikova, P. C. Sherrell, P. Palczynski, V. L. Bemmer, and C. Mattevi, “Direct solution-phase synthesis of 1t' WSe<sub>2</sub> nanosheets,” *Nature Communications*, vol. 10, feb 2019.
- [180] H. Chen, X. Wen, J. Zhang, T. Wu, Y. Gong, X. Zhang, J. Yuan, C. Yi, J. Lou, P. M. Ajayan, W. Zhuang, G. Zhang, and J. Zheng, “Ultrafast formation of interlayer hot excitons in atomically thin MoS<sub>2</sub>/WS<sub>2</sub> heterostructures,” *Nature Communications*, vol. 7, aug 2016.
- [181] Q. Wang, P. Wu, G. Cao, and M. Huang, “First-principles study of the structural and electronic properties of MoS<sub>2</sub>–WS<sub>2</sub>and MoS<sub>2</sub>–MoTe<sub>2</sub>monolayer heterostructures,” *Journal of Physics D: Applied Physics*, vol. 46, p. 505308, nov 2013.
- [182] X. Yu and K. Sivula, “Photogenerated charge harvesting and recombination in photocathodes of solvent-exfoliated WSe<sub>2</sub>,” *Chemistry of Materials*, vol. 29, pp. 6863–6875, aug 2017.
- [183] X. Yu and K. Sivula, “Toward large-area solar energy conversion with semiconducting 2d transition metal dichalcogenides,” *ACS Energy Letters*, vol. 1, pp. 315–322, jun 2016.
- [184] K. Sivula and R. van de Krol, “Semiconducting materials for photoelectrochemical energy conversion,” *Nature Reviews Materials*, vol. 1, jan 2016.

- [185] C. Tan, J. Chen, X.-J. Wu, and H. Zhang, “Epitaxial growth of hybrid nanostructures,” *Nature Reviews Materials*, vol. 3, jan 2018.
- [186] X. Li, Y. Dai, M. Li, W. Wei, and B. Huang, “Stable si-based pentagonal monolayers: high carrier mobilities and applications in photocatalytic water splitting,” *Journal of Materials Chemistry A*, vol. 3, no. 47, pp. 24055–24063, 2015.
- [187] J. Shi, D. Ma, G.-F. Han, Y. Zhang, Q. Ji, T. Gao, J. Sun, X. Song, C. Li, Y. Zhang, X.-Y. Lang, Y. Zhang, and Z. Liu, “Controllable growth and transfer of monolayer MoS<sub>2</sub> on au foils and its potential application in hydrogen evolution reaction,” *ACS Nano*, vol. 8, pp. 10196–10204, sep 2014.
- [188] P. C. Sherrell, P. Palczynski, M. Sokolikova, F. R. and Federico M. Pesci, M. Och, and C. Mattevi, “Large-area cvd mos2/ws2 heterojunctions as a photoelectrocatalyst for salt water oxidation,” *ACS Appl. Energy Mater.*, 2019.
- [189] S. M. Sze and K. K. Ng, *Physics of Semiconductor Devices*. Wiley-Blackwell, 2006.
- [190] T. Ogura, “Analyzing indirect secondary electron contrast of unstained bacteriophage t4 based on SEM images and monte carlo simulations,” *Biochemical and Biophysical Research Communications*, vol. 380, pp. 254–259, mar 2009.
- [191] V. Kochat, A. N. Pal, E. S. Sneha, A. Sampathkumar, A. Gairola, S. A. Shivashankar, S. Raghavan, and A. Ghosh, “High contrast imaging and thickness determination of graphene with in-column secondary electron microscopy,” *Journal of Applied Physics*, vol. 110, p. 014315, jul 2011.
- [192] G. Binnig, C. F. Quate, and C. Gerber, “Atomic force microscope,” in *Scanning Tunneling Microscopy*, pp. 55–58, Springer Netherlands, 1993.
- [193] I. Schmitz, M. Schreiner, G. Friedbacher, and M. Grasserbauer, “Tapping-mode AFM in comparison to contact-mode AFM as a tool for in situ investigations of surface reactions with reference to glass corrosion,” *Analytical Chemistry*, vol. 69, pp. 1012–1018, mar 1997.